

University of Nottingham
UK | CHINA | MALAYSIA

Hyperpolarized Krypton ^{83}Kr as a Novel Contrast Agent for pulmonary Magnetic Resonance Imaging (MRI)

Thesis submitted in partial fulfillment of the requirements of University of Nottingham for the degree of Doctor of Philosophy

SALEH ALRUMYAN, MSc

Supervisors:

Prof Meersmann, Thomas

Prof Morris, Peter

March 2019

School of Medicine
Nottingham University
United Kingdom

DEDICATION

I dedicate this work to my parents; my mother Thuriya Suliman Alshammary (I ask God to keep her in good health), and my father Abdulkareem Alrumyan (May God have mercy on him). The Dedication is linked to my wife Mashael Alhayes. Their never ending support of my endeavor for this Ph.D. has been a much needed and well used constant in my life. Since the moment I applied to programs, they have supported every decision I have made. While some of these decisions have involved moving away from home, they have never questioned my choices, instead offering me even more support and opportunities.

Mom, Dad, Masael this is for you.

DECLARATION

I hereby confirm that the present thesis

Hyperpolarized Krypton ^{83}Kr as a Novel Contrast Agent for pulmonary Magnetic Resonance Imaging (MRI)

is the result of my own independent scholarly work, and that in all cases material from the work of others (in books, articles, essays, dissertations, and on the internet) is acknowledged, and quotations and paraphrases are clearly indicated. No material other than that listed has been used. I have read and understood the Institute's regulations and procedures concerning plagiarism.

ACKNOWLEDGEMENTS

I would like to acknowledge a number of people for both their professional and personal support in the writing of this thesis and collection of the contained data. I think that it is only proper to start by thanking to Professor Thomas Meersmann, my principle PhD supervisor. I am grateful for the opportunity to work with him. He has given me from his time, support and mentorship over the years. I am also appreciative to my other supervisors Professor Peter Morris and my inernal assesor Professor Richard Bowtell for their advice and input over the duration of my PhD.

I would like to thank Dr Clementine Lesbats, and Dr Wasif Dia, fellow PhD PostDoc and reasearch group people & students whom I have spent many late nights with collecting data. They have been instrumental in conducting the experimental work in this thesis and have both become dear friends.

Similarly I would like to express my gratitude to Dr Galina Pavlovskaya for her insight and assistance. I am of course very thankful also to others that have helped make this research possible including Clive Dixon, Alan Dorkes, for constructing the wealth of specialized glassware and equipment used throughout this work.

I have also received a lot of support from the many friends I have made in the Sir Peter Mansfield Magnetic Resonance Centre. While I would like to, I can not list everyone here, but all the same you have my gratitude.

Finally I would like to acknowledge and thank the Ministry of Health in collaboration with Ministry of Education for funding me through my PhD.

INTRODUCTION

This PhD thesis is devoted to the problem of visualization of respiratory organs by magnetic resonance imaging and is aimed at developing a method of magnetic hyperpolarization of noble gases and developing a method for visualizing lungs using inert noble gases. According to the World Health Organization, respiratory diseases are considered to be the most common (Organization et al., 2011).

Many lung diseases are either completely incurable or treatable only at early stages of their development (lung cancer, chronic obstructive pulmonary disease, etc.). Early diagnosis of such diseases, even if it does not guarantee full recovery, then allows to stop the deterioration of the patient's condition. That is why the development of new methods for diagnosing lung pathologies in the early stages of their development is an extremely urgent task. In some existing methods of diagnosing the lungs such as spirometry, radiography, fluorography, and computed tomography, etc.) either ionizing radiation harmful to humans or only global pathological abnormalities are detected. In turn, magnetic resonance imaging (MRI) is safe and one of the most effective methods of medical diagnosis. However, traditional MRI techniques based on hydrogen nuclei (protons) can not provide diagnostable lung images (Gould and Isaacson, 1993).

Lungs are difficult to image, study, and study when conventional magnetic resonance imaging is used because of the presence of air in the lungs. air is inactive when used for magnetic resonance, for chemical and physical reasons, which will be addressed later.

Numerous studies have been carried out aimed at finding gases that would make it

possible to obtain informative MRI images of the lungs. Such gases include oxygen, fluorine-containing gases and noble hyperpolarized gases (Edelman et al., 1996; Kuethe et al., 1998; Fain et al., 2010). The choice of hyperpolarization method is due to a combination of low cost ^{83}Kr and a number of interesting physical properties relative to other noble gases used in MRI (Albert and Hane, 2016).

It should be noted that the MRI technique for visualization of lungs with hyperpolarized gases is practically not developed in Saudi Arabia, therefore, the experiments on this Method for this PhD thesis were conducted within the framework of a three years with full time work with the group of Professor T. Meersmann and G. Pavlovskaya at the **Sir Peter Mansfield Imaging Center (SPMIC)**(Nottingham University, Nottingham, United Kingdom).

In this thesis the author will lay the foundation stone and discuss the basic principles for developing the technical methods of the magnetic resonance imaging system to detect chest diseases. The use of the technique of hyperpolarisation will open the doors for the possibility of imaging this physical member by magnetic resonance. On the other hand, this technique is one of the medical laser applications used to produce hyperpolarisation.

At the moment, the SPMIC laboratory for magnetic hyperpolarization of ^{83}Kr uses a 24W laser. In this case, optical pumping of 75 ml cells is performed. Increase a cell volume and productivity can be achieved by using a laser of higher power. Nevertheless, the cost of some type of noble gases used in MRI remains high, and the procedure of gas hyperpolarization is complicated and expensive (Liu et al., 2014).

This thesis will briefly describe two different projects related to clinical MRI. The ultimate aim of the overall thesis is to develop a protocol for MRI scanner to enable future clinical application. This thesis sets off with a few words about the classical theory of MRI to explain how hyperpolarisation, which is a relatively new technique, is different from the conventional MRI methodology. Although it is a fairly new technique that is not yet available outside specialized research centres, substantial work and research in pulmonary MRI, including human subject studies, has taken place over the past decade.

A summary literature review will be used explain the use of hyperpolarised noble gases. Also, this thesis will address how human lung physiology works and a description of ventilation, perfusion, diffusion, and gas transport will be provided. Secondly, an introductory

will be given concerning of MR system and ^{83}Kr probe basic hardware using saddle coils and the concept of ^{129}Xe and ^{83}Kr hyper polarization, polarisation level determination, and applications will be provided. Thirdly, an overview of the pulse sequences used for imaging with hyperpolarised noble gases and the effects and advantages of these new modified pulse sequences will be discussed. Finally, the main hyperpolarised ^{83}Kr experiment in preclinical ex vivo research field to show the sensitivity of ^{83}Kr and how ^{83}Kr is stored will be described. Also, a discussion of what are the future considerations required to make this technique applicable in human subject will be addressed.

CONTENTS

Dedication I

Acknowledgements V

Introduction VII

List of Figures XIII

List of Tables XV

List of Symbols XVII

1 Introduction to Lung: A General consideration 1

1.1 Lung Anatomy 2

1.1.1 Blood Supply 3

1.1.2 Lungs Pleura 4

1.2 Lung Physiology 4

1.2.1 Breathing Mechanism 5

1.2.2 Airway Architecture 6

1.2.3 Ventilation & Perfusion 7

2 NMR System's Hardware 9

2.1 Magnet 9

2.1.1 Superconductivity . . . 10
2.1.2 Superconducting Magnets . . . 12
2.1.3 Magnet Coils . . . 14
2.1.4 Magnet Shielding . . . 15
2.1.5 Shim Coil & Shimming . . . 16
2.1.6 Gradient Coils . . . 20
2.2 Probe . . . 23
2.2.1 Law of Biot and Savart . . . 24
2.2.2 Magnetic Flux . . . 24
2.2.3 Faraday's Law . . . 24
2.2.4 Inductor . . . 25
2.2.5 Capacitor . . . 25
2.2.6 RCL circuit . . . 26
2.2.7 Quality Factor . . . 28
2.2.8 Shielding . . . 30
2.2.9 Coil Geometry . . . 31
2.3 Operator Console . . . 31
2.4 Technical Equipment . . . 32

3 MR Signal Relaxation **35**
3.1 Spin Bundle . . . 35
3.2 Spin-lattice Thermal Relaxation . . . 36
3.3 Saturation Recovery Technique (Thermal Sample) . . . 37
3.3.1 Signal Intensity using Saturation Recovery from Thermal Sample . . . 38
3.3.2 Saturation and Image Contrast . . . 40
3.4 Inversion Recovery Technique (Thermal Sample) . . . 41
3.4.1 Inversion Recovery and Image Contrast . . . 41
3.5 T_1 relaxation using (HP Sample) . . . 42
3.6 Spin-Spin Thermal Relaxation . . . 44
3.7 Spin Echo(SE) Method . . . 45
3.7.1 Graphical Description of Spin Echo Method . . . 46

3.7.2 Signal Phase Cycling . . . 47
3.7.3 Pulse Criteria . . . 48
3.8 Limitation of Spin Echo (SE)Method . . . 49
3.9 Fast Spin Echo or Multiple Spin Echo . . . 50
3.10 Diffusion . . . 50
3.10.1 The Carr-Purcell Mechanism . . . 51
3.10.2 The Meiboom-Gill Improvement . . . 51

4 Pump Cell Preparation **53**
4.1 Construction . . . 53
4.2 Pump Cell Cleaning . . . 53
4.3 Rubidium Filling . . . 54
4.4 Pump Cell Priming . . . 56
4.5 Pump Cell Loading . . . 57

5 Hyperpolarisation **59**
5.1 Classical Theory of MRI Physics . . . 59
5.1.1 Composition of Nuclei . . . 59
5.1.2 Isotopes . . . 60
5.1.3 Nuclear Spin . . . 61
5.1.4 Hydrogen Nuclei in MRI World . . . 62
5.1.5 Hydrogen Nuclei is not used in MRI Pulmonary Application . . . 64
5.2 Historical Background in Hyperpolarised Noble Gases uses in Pulmonary Imaging 66
5.3 ^{3}He at Market and in Research Field . . . 67
5.4 Noble Gases and Alkali Metal Properties . . . 67
5.4.1 Rubidium [Rb] . . . 67
5.4.2 Xenon ^{129}Xe . . . 68
5.4.3 Krypton ^{83}Kr . . . 69
5.5 Optical pumping Concept . . . 70
5.5.1 Temperature Effect . . . 71
5.6 Optical pumping & Spin Exchange . . . 73
5.6.1 Optical pumping (OP) . . . 73

5.6.2 Spin Exchange (SE) . . . 74
5.7 Polarisation in SEOP . . . 75
5.8 Gas Mixture . . . 77
5.9 Polarization & SEOP Pressure . . . 78
5.9.1 Apparent polarization . . . 78
5.9.2 Xenon Polarization . . . 78
5.9.3 Krypton Polarization . . . 79
5.10 Application of Hyperpolarised Noble Gas . . . 80
5.10.1 ^{129}Xe Ventilation imaging . . . 80
5.10.2 ^{129}Xe Perfusion Imaging . . . 84
5.10.3 ^{83}Kr Media (Surface) Interaction . . . 86
5.10.4 ^{83}Kr Surface Hydration Effect on T_1 Relaxation . . . 86
5.10.5 ^{83}Kr Concentration Vs T_1 Relaxation . . . 87

6 Hyperpolarised Laser Characteristics 89
6.1 Introduction . . . 89
6.2 Material and Method . . . 91
6.2.1 Laser Power Output Experiment . . . 91
6.2.2 Spectral Line Shape Experiment . . . 92
6.3 Results & Data Analysis . . . 93
6.3.1 Analysing Laser Power Output Data . . . 93
6.3.2 Analysing Spectral Line Shape Data . . . 94
6.4 Discussion . . . 95
6.5 Conclusion . . . 96

7 HP ^{83}Kr T_1 Relaxation as Surface Analyser 97
7.1 Introduction . . . 97
7.2 Materials and Methods . . . 99
7.2.1 ^{83}Kr Optical Pumping . . . 99
7.2.2 NMR Measurements . . . 100
7.2.3 Samples Design & Preparation . . . 100
7.3 Result . . . 102

7.3.1 Hydrated Treatment . . . 102
7.3.2 Dehydrated Treatment . . . 104
7.3.3 Oven Treatment . . . 105
7.4 Discussion . . . 106
7.4.1 Data Analysis . . . 106
7.4.2 Data Reliability . . . 109
7.5 Conclusion . . . 109

8 Remote Detection of HP ^{83}Kr Gas 111
8.1 Introduction . . . 111
8.2 Material and Method . . . 112
8.2.1 ^{83}Kr Optical Pumping . . . 112
8.2.2 NMR Measurements . . . 113
8.2.3 Re-compression System Design & Preparation . . . 113
8.2.4 Experimental Set-Up and Transfer of HP ^{83}Kr . . . 114
8.3 T_1 Calculation . . . 117
8.3.1 Data Analysis . . . 117
8.3.2 Justification and Data Reliability . . . 118
8.4 Results . . . 120
8.5 Discussion . . . 121
8.6 Conclusion . . . 122

9 Future Work 123

10 Conclusion 125

Bibliography 129

LIST OF FIGURES

1.1 Lung Breathing Mechanism, (Won et al., 2014) 2

1.2 Gas Exchange at the Alveolicapillary Membrane , (Won et al., 2014; Shier et al., 2001) 4

1.3 Lung Breathing Mechanism, (Won et al., 2014) 6

1.4 Respiratory Tree, Z is the lung genertion numbers (Shier et al., 2001) 8

2.1 Cross-section of a superconducting wire of overall diameter 0.7 mm, containing about 6,000 filaments of 5 μm superconductor, Pantsyrny et al. (2009). . 11

2.2 The operating parameters of a NbTi supercondutor,(Pisanty, 2017; Sharma, 2015). 12

2.3 Cross-section of a typical superconducting magnet cryostat,(Lvovsky et al., 2013). 13

2.4 Cross-section of research spectrometer, (Lvovsky et al., 2013). 13

2.5 A generalised coil system, (De Graaf, 2013). 14

2.6 Schematic Diagram of Magnet Shielding 16

2.7 Tesseral harmonic $(x^2 - y^2)$,(De Graaf, 2013). 17

2.8 Shim coil designed to null spherical harmonic component of B_z,(De Graaf, 2013). 18

2.9 Images of zonal harmonics component of B_z, (De Graaf, 2013). 19

2.10 Z-Gradient coils, (Hidalgo-Tobon, 2010; Keeler, 2011). 21

2.11 X and Y-Gradient coils, (Hidalgo-Tobon, 2010; Keeler, 2011). 22
2.12 (a) X-gradient field path, (b) Y-Gradient field path, and (c) Z-gradient field path from X,Y,andZ coils respectively,(Lemdiasov and Ludwig, 2005; Keeler, 2011). 22
2.13 Shielding Coils,(Lemdiasov and Ludwig, 2005) 23
2.14 (a)a single-loop RF coil and (b) RLC circuit,(Mispelter et al., 2006). 27
2.15 The resonance curve – the centre of the curve is the desired condition. 28
2.16 The tunning and matching stages– the centre of the curve is the desired condition. 29
2.17 Saddle Coil Design, (Hidalgo-Tobon, 2010; Keeler, 2011). 31
2.18 schematic diagram of operator console and its connection 31
2.19 schematic diagram of technical equipment and its connection 34

3.1 The effect of magnetic field B_0 on spin 36
3.2 Net Magnetisation Vector 36
3.3 Equilibrium Magnetisation $M_Z = M_0$ 37
3.4 Saturation process 38
3.5 T_1 process 38
3.6 Signal Intensity from Steady State Process 39
3.7 Relation between Signal Intensity and Magnetization 39
3.8 T_1 axial images of the brain. Contrast of brain images reduces with increasing TR values – (right) TR = 140 ms; (left) TR = 460 ms, (Westbrook and Talbot, 2018). 40
3.9 Magnetization Pattern of Inversion Recovery 41
3.10 Inversion Recovery Sequence 41
3.11 Inversion recovery axial images of the brain. Contrast of brain images reduces with increasing TI values – (left) TI = 165 ms; (right) TI = 600 ms (Westbrook and Talbot, 2018). 42
3.12 T_1 relaxation using saturation method with HP sample 43
3.13 FID of HP sample 43
3.14 Integration of the Spectrum 44

3.15 T2 Relaxation Following RF Application 45
3.16 Spin Echo $\pi/2$ on x axis While π on y axis 46
3.17 Spin Echo $\pi/2$ on X-axis While π on Y-axis 47
3.18 Sketch of Two Alternative of Pulse 48
3.19 Signal strength decay, (Westbrook and Talbot, 2018). 49
3.20 Sketch of Double Spin Echo Pulse Sequence 50
3.21 Sketch Diagram of CPMG sequence 52

4.1 The Shape of fabricated and clean Pump Cell. 54
4.2 Used pump Cell Coated with Oxidised Rubidium 55
4.3 Glove box inner chamber & oven vacuum outer chamber. 55
4.4 pump Cell after Priming Process 56
4.5 pump Cell within Helmholtz Coil 58
4.6 Achieving Circularly Polarized Light by $\lambda/4$ plate, (Meersmann and Brunner, 2015). 58

5.1 Nuclei Composition, (Cherry et al., 2012) 60
5.2 Zeeman Splitting, (Weibel, 2009) 61
5.3 MRI Lung Images: (a) Conventional T_1 Weighted Image multi-slice spin (b) Axial l T_1 Weighted Image with multi-slice projection reconstruction(motion artefact has disappeared),(Wielpütz and Kauczor, 2012) 65
5.4 MRI Lung Images: (a) Hyperpolarised ^3He of human lung (b) Proton Density (PD) image of the same lung, (Gould and Isaacson, 1993) 65
5.5 MRI of rat Lung Images using Hyperpolarised ^{129}Xe, (Albert et al., 1994) . . 66
5.6 MRI Pig Lung Imagesusing GRASS Sequence, (Middleton et al., 1995) 66
5.7 The D_1 transition of Optical pumping (OP) Associated with Collision Between Rb Electron and Laser light 73
5.8 The Effect of Magnetic field on Zeeman Sub-level polarisation (a) In The Absence of Magnetic Field (b) In The Presence of Magnetic Field, (Meersmann and Brunner, 2015). 74
5.9 Flip-Flop Action of Rb and ^{129}Xe Spin Exchange (SE), (Birchall et al., 2017). 75

5.10 Comparison between NMR Signal from $Thermally$ Polarised Spin System and Hyperpolarised Spin System, (Meersmann and Brunner, 2015). 75

5.11 The polarization obtained for different gas mixtures of ^{129}Xe with buffer gas N_2 as a function of SEOP pressure using 30 W of circular polarised laser light, (Meersmann and Brunner, 2015). 79

5.12 The polarization obtained for different gas mixtures of ^{83}Kr with buffer gas N_2 as a function of SEOP pressure using 30 W of circular polarised laser light, (Meersmann and Brunner, 2015). 80

5.13 Improved MRI image from ^{129}Xe compared to ^{3}He Image, (Mugler and A, 2013). 80

5.14 MRI ^{129}Xe Images of Various Lung Disease, (Shukla et al., 2012). 81

5.15 Fast Low Angle Shot (FLASH) Sequence, (Hatabu et al., 1999). 82

5.16 Signal Intensity comparison between (a) fixed flip angle and (b) variable flip angle, (Lilburn et al., 2013; Zhao et al., 1996). 83

5.17 MRI images from Dynamic EPI sequence, (Gierada et al., 2000). 84

5.18 Proton spectrum of ethyl acetate showing unique peaks for each of the three types of protons. 84

5.19 ^{129}Xe in the Lung Tissue Dissolved Phases, (Driehuys et al., 2006). 85

5.20 Schematic Diagram of MXTC Technique of Image Acquisition, (Driehuys et al., 2006; Meersmann and Brunner, 2015). 85

5.21 Coronal images of Rat lung (A)^{129}Xe in (airspace) gas phase, (B)^{129}Xe in the lung tissue dissolved phase, (C)^{129}Xe in RBC dissolved phase, (Driehuys et al., 2006). 86

5.22 The ^{83}Kr MR images with Flash sequence to hydrophilic beads (i) untreated (ii) treated beads, (Pavlovskaya et al., 2005). 86

5.23 The T_1 relaxation time comparison between hydrated and dehydrated surface, (Cleveland et al., 2007) 87

6.1 (A): Laser Power Supply (B): Laser Cooling System. 90

6.2 Laser Power Meter, Thermal Sensor, and Solid State Temperature Control used for Experiment Set Up. 91

6.3 (A): Thermal Sensor without Direct Laser Beam,(B): Laser Circular light Facing Thermal Sensor Inside Hyperpolariser. 92
6.4 Fibre Optic cable connected to Computer Software via Spectrometer 92
6.5 Laser Power Output Versus Operating Current 93
6.6 laser intensity of spectral line shape in 794.7 nm wavelength 94
6.7 analysed data (A) extracted data De-convoluted, (B) multi-peak data fitting, and (C) residual data from both peak 95
6.8 The Report shows Type and Fitting Parameters of Both Peaks 96

7.1 Micro-structure of Three Variable Size Relaxing Agent Foam 101
7.2 The Internal Diameter of Relaxing Agent B, C, and D 101
7.3 Relaxing Agent Foams filled within medical universal vials 102
7.4 The signal Intensity as a function of time for Hydrated sample A (empty) . . 103
7.5 The signal Intensity as a function of time for Hydrated sample B (Medium surface-to-volume Foam) 103
7.6 The signal Intensity as a function of time for Hydrated sample C (Small surface-to-volume Foam) 104
7.7 The signal Intensity as a function of time for Hydrated sample D (Large surface-to-volume Foam) 104
7.8 The signal Intensity as a function of time for Dehydrated sample A 105
7.9 The signal Intensity as a function of time for Dehydrated sample B) 105
7.10 The signal Intensity as a function of time for Dehydrated sample C 106
7.11 The signal Intensity as a function of time for Dehydrated sample D 106
7.12 The signal Intensity as a function of time for **Oven sample E** 107
7.13 The signal Intensity as a function of time for **Hydrated sample F** 107
7.14 SEOP Measurements Stability Overtime 109
7.15 Analysis of Average T_1 Data Collected for HP ^{83}Kr of sample Materials 110
7.16 Schematic Diagram of Phantom Design for In vivo Clinical Scanner 110

8.1 a Schematic Diagram of Re-compression System Design 114
8.2 a Schematic Diagram show Inside Hyperpolarizing Unit. 115
8.3 Gauss Meter. 116

8.4 Schematic diagram of experimental set up. Recompression system was placed on a table with vaccuum pump underneath to aid with evacuating the system. 117
8.5 1D Plot for Peak hieght Method FID 118
8.6 The T_1 Value from 1D spectrum 50 G after Normalised Signal fitted 119
8.7 1D spectrum Shows Integration Method 119
8.8 The T_1 Value from 1D spectrum 50 G after Normalised Signal fitted 120
8.9 Pump cell Stability 121
8.10 T_1 value versus fringe field of 9.4 T magnet 122

LIST OF TABLES

1.1 Lobes and segments of lung 3

2.1 Common Shim 'Names' and their Cartesian Function,(De Graaf, 2013). 19

3.1 Signal Phased Cycle Generated by Combination of $\pi/2$ and π Pulses 47

5.1 NMR Active noble Gases, (Mark Brown, 2010) 62

5.2 3 Dimensional Fast Gradient Sequence with breath hold 81

5.3 3 Dynamic EPI sequence 83

6.1 Extracted Data From Laser Power Output vs current and voltage Experiment 93

7.1 T_1 Value of Four Treated sample Using HP ^{83}Kr 108

7.2 The Average and Standard Deviation(SD) For Each Treated sample 108

8.1 The Normalised Signal of 1D decay from 50 Gauss Re-compression Experiment of Peak Height Method 118

8.2 The Normalised Signal of 1D spectrum from 50 Gauss Recompression Experiment of Integration Method 120

8.3 T_1 Value generated from Peak Height and Spectrum Integration of 1D plot from ^{83}Kr Recompression Experiment 120

LIST OF SYMBOLS

Abbreviations

$2D$	Two Dimensional
$3D$	Three Dimensional
B_1	Radiofrequency Field
FFT	Fast Fourier Transform
MRI	Magnetic Resonance Imaging
C	Capacitor
CSF	Cerebrospinal fluid
CT	Computed Tomography
EFG	Electric Field Gradient
FSE	Fast Spin Echo
$GRASS$	Gradient Recalled Acquisition in Steady State
GRE	Gradient Recalled Echo
HP	hyperpolarised
L	Inductor

NM	Nuclear Medicine
NMR	Nuclear Magnetic Resonance
PD	Proton Density
PET	Positron Emission Tomography
Q	Quality Factor
R	Resistor
RBC	Red Blood Cell
RF	Radiofrequency
rf	radiofrequency
$SEOP$	Spin Exchange Optical pumping
SNR	Signal to Noise Ratio
$SPECT$	Single Photon Emission Copmuted Tomography
$STIR$	Short-TI Inversion Recovery
STP	Standard temperature and Pressure
T_2^*	T_2 Star relaxation times
T_1	Longitudinal relaxation times
$T_1W.I$	T_1 Weighted Image
T_2	Transverse relaxation times
$T_2W.I$	T_2 Weighted Image
dB	decibel
FFA	fixed flip angle
FID	Free Induction Decay

Greek Letters

γ	Gyromagnetic ratio of specific nuclei
κ	Boltzmann Constant= $1.3805 \times 10^{-23} JK^{-1}$
$\mu_0 = 4\pi 10^{-7}\ \mathrm{H\,m^{-1}}$	permeability of magnet in air core space
τ	time

Symbols

w	Larmor frequency
w_0	Angular frequency or Angular speed
θ	flip angle
A	Mass Number
E	Energy of each orientation
f	Frequency.
H	Hydrogen
h	Planck's Constant
I	Nuclear spin value
I_c	Current
M_z	Magnetization along the z-axis
N	Neutron Number
n	total number of excitations
N_0	Population energy of ground level
N_I	Population energy of initial level
S	Angular momentum

S_n	signal intensity
V	sample volume
Z	Atomic Number
Z	Impedance
ℓ	Length of Coil
$\hbar$	Planck's constant/ 2π
∞	Infinity
AW	Average Weight
B_0	External magnetic field
$d\ell$	Electric charge
dB	Magnetic Field Amplitude
N	Number Of Turns in coil
Q	Electric Charge
r	radius of coil
T	temperature
V	Voltage
Z_0	Resisitive Impedance
Z_C	Capacitance Impedance
Z_L	Inductive Impedance

CHAPTER 1

INTRODUCTION TO LUNG: A GENERAL CONSIDERATION

Human lung is considered as one of the largest organs in the body although it contains only approximately of 0.5 litres of tissue. Each lung contains structures of both conducting and respiratory zones. The main function of the organ is to perform the primary gas exchange mechanism in the alveoli between oxygen and carbon dioxide with air from the atmosphere. The lungs exchange respiratory gases across a very large epithelial surface area, about 70 square meters, that is highly permeable to gases. The airways ventilating the lung split further as they go downward ending in the respiratory zone that has varying volume, depending on inhalation level, but a steady amount of blood volume. In the following, some of the fundamental components of respiratory and pulmonary organs will be elaborated (Weibel, 2009; Won et al., 2014).

The lung anatomy and physiology is a very branched and huge topic. In this thesis, the author will briefly discuss some major anatomical and physiological aspect of human lung.

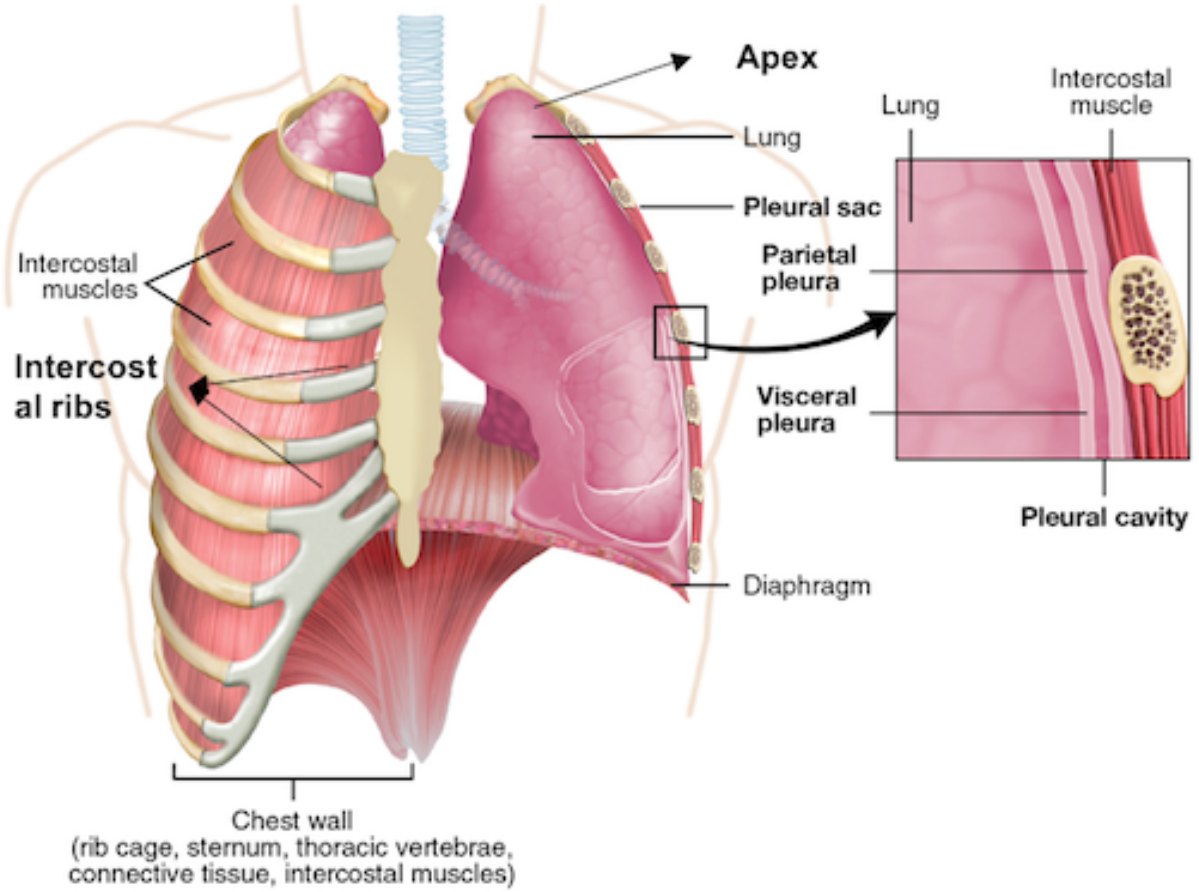


Figure 1.1: Lung Breathing Mechanism, (Won et al., 2014)

1.1 Lung Anatomy

The lungs are semi-pyramid shaped, paired organs that are attached to the trachea by right and left bronchi. Inferiorly, the lungs are bordered by the diaphragm and surrounded by intercostal ribs. The diaphragm is a flat, dome-shaped muscle located at the base of the lungs and thoracic cavity. The lungs are enclosed by the pleurae, which are normally connected to the mediastinum. The right lung is shorter and wider than the left lung. Due to this cause, the left lung occupies a smaller volume than the right. The apex of the lung is the superior region, whereas the base is the opposite region near the diaphragm. The costal surface of the lung borders the ribs. The mediastinal surface faces the midline (Hess et al., 2015; Shier et al., 2001). The lung anatomy is shown in Figure 1.1

Each lung is made of smaller structure called lobes. Fissures divide & separate these lobes from each other. The right lung consists of three lobes: the superior, middle and inferior lobes. The left lung consists of two lobes: the superior and inferior lobes. A segment is a division of a lobe, and each lobe houses multiple segments, as shown in Table 1.1. Each

segment receives air from its own tertiary bronchus and is supplied with blood by its own artery (Hess et al., 2015; Shier et al., 2001).

Table 1.1: Lobes and segments of lung

Lung	Lobe	Segment
Right	Upper	Apical
		Anterior
		Posterior
	Middle	Lateral
		Medial
		Superior
	Lower	Anterior basal
		Posterioe basal
		Lateral basal
		Medial Basal
Left	Upper	Apical posterior
		Anterior
		Superior lingualr
		Inferior lingualr
	Lower	Superior
		Anterior medial basal
		Lateral basal
		Posterior basal

1.1.1 Blood Supply

The blood permits lungs to carry out their primary function of gas-exchange. The pulmonary artery arises from the pulmonary trunk of the cardiac atrium and carries deoxygenated blood to the alveoli. The pulmonary artery branches multiple times as it follows the bronchi, and each branch becomes more and more smaller in diameter to end with the capillary tree. The capillaries branch and follow the bronchioles and structure of the alveoli, as shown in Figure 1.2. It is at this point that the capillary wall meets the alveolar wall, creating the respiratory membrane (Hess et al., 2015; Shier et al., 2001).

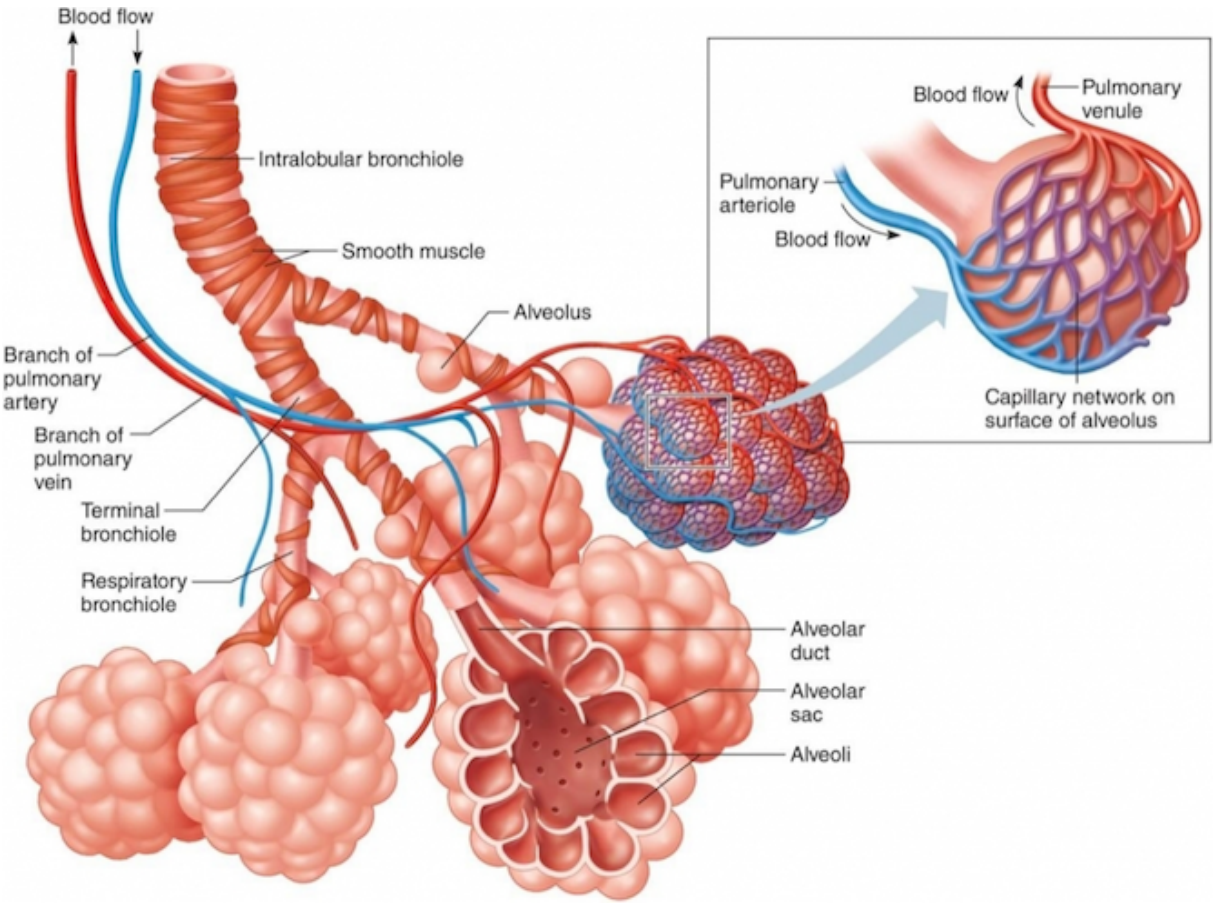


Figure 1.2: Gas Exchange at the Alveolicapillary Membrane , (Won et al., 2014; Shier et al., 2001)

1.1.2 Lungs Pleura

Each lung is enclosed and surrounded by the pleura cavity. The pleura is a smooth membrane that surrounds the lung. Both pleurae, which enclose the right and left lungs, respectively, are separated by the mediastinum. There are two layers of pleurae :the **visceral pleura** is superficial layer and extends into lines of the lung fissures, as shown in Figure 1.1. On the other hand, the**parietal pleura** is the outer layer that connects to the thoracic wall, the mediastinum and the diaphragm. The **pleural cavity** is the space between the visceral and parietal layers. Both pleurae, produce pleural fluid which is secreted by mesothelial cells and acts to lubricate their surfaces (Hess et al., 2015).

1.2 Lung Physiology

The functional part of the lungs exists in the parenchyma. Within this part of an adult lung, there are ≈ 300 million alveoli. Each alveolus is ≈ 300 micron in diameter. The ability to

breathe, i.e. to have air enter the lungs during inspiration and air leave the lungs during expiration, is dependent on the air pressure of the atmosphere and the air pressure within the lungs(Hess et al., 2015).

1.2.1 Breathing Mechanism

The breathing mechanism can be described as inspiration and expiration of the lung, which is described in detail in the following paragraphs:

1.2.1.1 The Inspiration

Inspiration is usually controlled mainly by the brain stem. When the medulla oblongata is activated, the diaphragm and the inter-costal muscle start stretch away from their exact locations. This allows the thoracic cavity to expand and accordingly plural cavity pressure is decreased. The diaphragm plays a major role in this process. Due to its contraction, the lower ribs that it is attached to rotates horizontally and thus the thoracic cavity expands. While normal human subject breathing in the resting state makes the diaphragm stretch about 1 cm downward, the athletes' and runners usually put an excessive force during both air inhalation and exhalation thus, the movement may reach up to 10 cm. At the time the intercostal muscles contract, the ribs connected to these muscles usually moves superiorly and interiorly leading to volume increase in the chest wall (Shier et al., 2001).

According to the previous scenario, the air passes through trachea and airway branches into the alveoli until pressure in the alveoli equalizes with the pressure at the air way opening. This process can be seen in figure1.3 (Weibel, 2009; Won et al., 2014).

1.2.1.2 The Expiration

Expiration is considered as a passive incident because of the recoiling lung elasticity and the surface tension of fluid covering the alveolar surface. The consequence of removing the air rapidly from the lung (i.e. expiration), will increase the pleural cavity pressure as shown in figure1.3 (Weibel, 2009; Won et al., 2014).

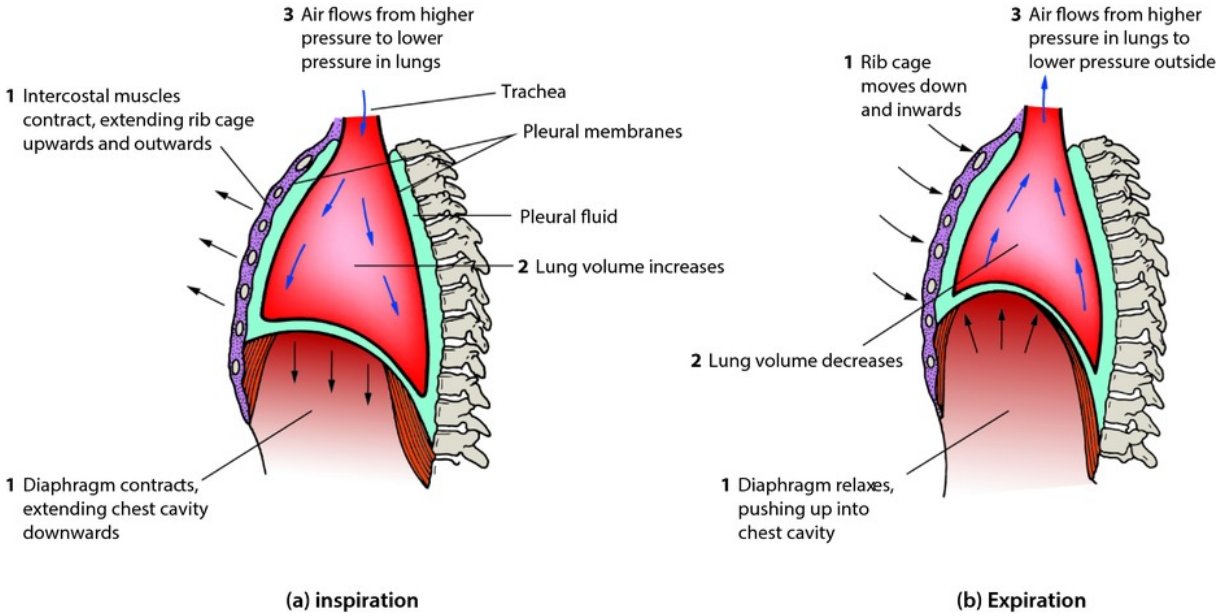


Figure 1.3: Lung Breathing Mechanism, (Won et al., 2014)

1.2.2 Airway Architecture

The inhaled air passes into the airways and carries on until it reaches the lung respiratory epithelium part. The branches of the airways are usually like tubes that become smaller and narrower as they permeate in the lung. The trachea is divided into smaller main left and right bronchi. These two main bronchi will be subdivided into narrower lobar and segmental bronchi. According to Weibel (2009), the branches of the human airway system are classified into 23 generations. The epithelial airway walls from 0-14 generations of human airway beginning with the trachea and ending with the terminal bronchioles. These are known as the Conducting District. The Acinar District is where the alveoli are becoming a part of the construction of the airway as well as the gas exchange occurs. This district represents the generations from 15 to 23 (Weibel, 2009). The epithelium of this district begins with the transitional bronchioles at generation 15. From generation 16 to 18 the respiratory bronchioles are developed with more alveoli. As the branching continues, the alveoli start to develop to form an alveolar duct at the area of generation 19 to 22. Further splitting occurs and ultimately ends with the alveolar sac or what is called pulmonary Acinar at generation 23. Most of the lung air space is contained in the acinar region, which represent approximately 3 litres. Figure 1.4 shows the repiratory tree and airway architecture (Weibel, 2009; Won et al., 2014).

1.2.3 Ventilation & Perfusion

The major pulmonary artery is followed by a series of branching arteries until the end of pulmonary capillaries. These tiny tubes are attached to the barrier that is connecting to the alveolar duct and sac known as blood-gas barrier. This barrier allows the blood to reach the respiratory tissue and blood where gas exchanges occur (Weibel, 2009).

Weibel (2009) described that ventilation in human subjects occurs in series whereas the vascular capillaries are connected in parallel. During the inhalation process, the oxygen, O_2 reaches the acinar area sequentially. As the alveoli are arranged in sequential order, the air with time moves from central alveoli to more peripheral alveoli. This could in principle lead to 'screening' i.e. a situation where little oxygen is left for the final alveoli. This would be a problem as about half of the total lung volume is made up by the respiratory end zone.

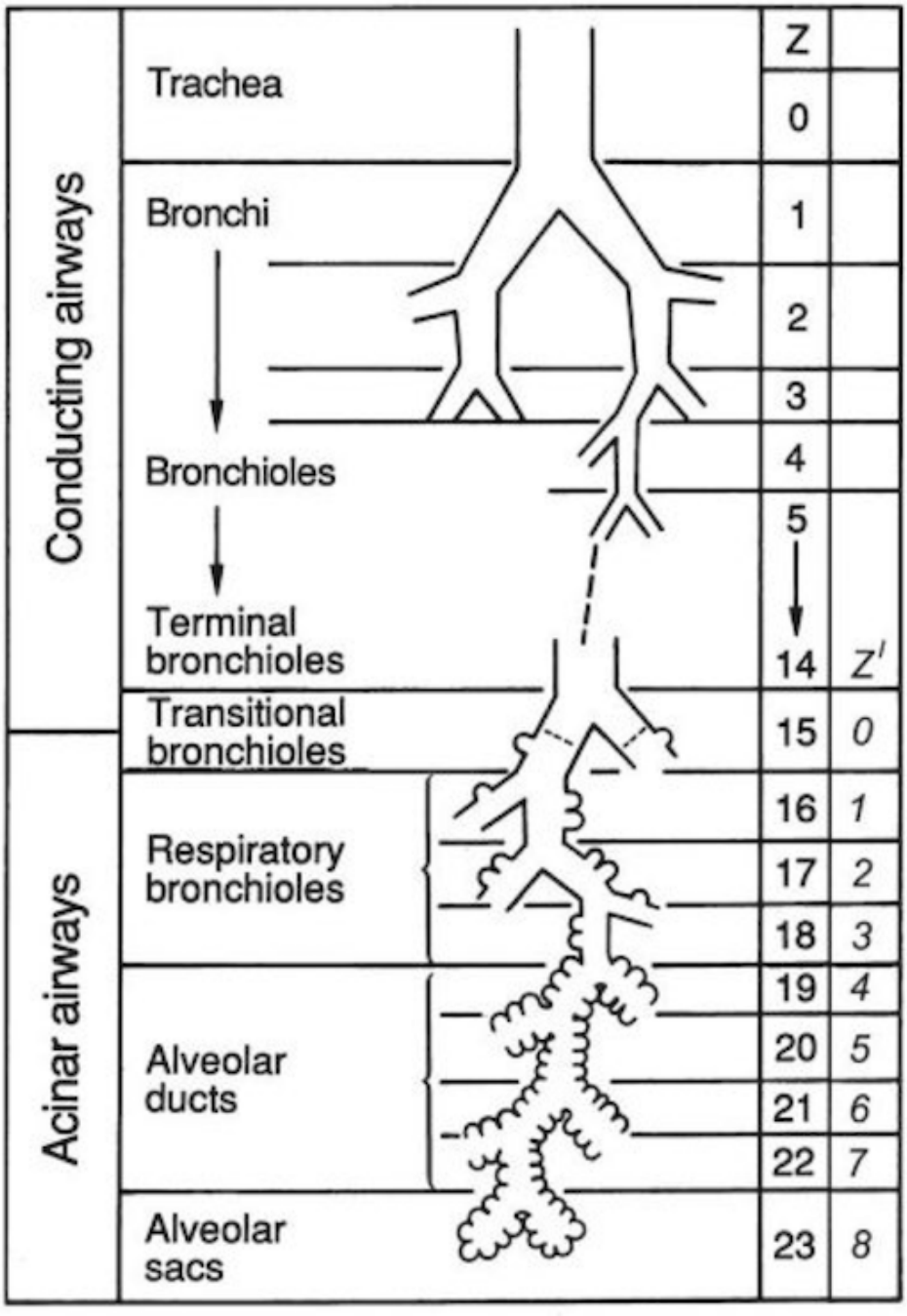


Figure 1.4: Respiratory Tree, Z is the lung genertion numbers (Shier et al., 2001)

CHAPTER 2

NMR SYSTEM'S HARDWARE

The Magnetic Resonance Spectrosopy (MRS) system is made up of several main groupings of equipment. Our focus in this chapter is on NMR architectures in preclinical (laboratory systems):

1. The Magnet
   (a) Magnet Coils
   (b) Gradient Coils
   (c) Shim Coils
   (d) Shielding
2. Radio-frequency Coils (Probe)
3. Operator Console
4. Technical Equipment

2.1 Magnet

The magnet in NMR system is one of the most critical components to the performance of the instrument. The field generated by the magnet must be:

- very pure & intense – with homogeneous regions which refers to the uniformity of a magnetic field in the center of a scanner when no (subject or sample) is present. Magnetic field homogeneity is measured in parts per million (ppm) over a certain diameter of spherical volume (DSV) which is often called diameter sensitive volume of 10-25cm in preclinical magnet.

- very stable – the temporal stability of the field in the dsv is usually less than 0.1 ppm/hour (Finnemore et al., 1966).

In general there are different classes of NMR magnets. In this thesis we will focus only on the most commercial one, also known as **Superconducting magnet systems**. Above 0.3 T or higher, superconducting systems are used almost exclusively, and form the basis of the vast majority of preclinical MRI systems and Exvivo NMR research which could be seen in figure 2.6 (Finnemore et al., 1966).

2.1.1 Superconductivity

Superconductivity is a very strange phenomenon whereby certain metals and alloys when cooled to low temperatures behave as though they are 'perfect' conductors. The temperatures at which this phenomenon becomes apparent are very low – usually few degrees below the boiling point of helium liquid i.e. 4.2 Kelvin (0 Kelvin = -273°C). A typical superconductor used for MR is a Niobium-Titanium (NbTi) alloy in a copper matrix and anywhere from 50 to 400 km of the wire may be required for a modern clinical MR magnet. NbTi in figure 2.1 is a type II superconductor, as is Niobium-3-Tin (Nb_3Sn), a conductor used at very high field strengths (Kwok et al., 1993; Pantsyrny et al., 2009).

2.1.1.1 Limitations of superconductivity

Superconductivity is not without its limitations. The current density (A/m^2) that a conductor can safely carry is dependent on the temperature of the conductor and field strength, which it resides in. In general, the lower the temperature and the lower the immersed field, the greater the ability to carry current (Vonsovsky et al., 1982).

NbTi coils are often kept at approximately 4.2 K in clinical scanners. 4.2 Kelvin is the boiling point of liquid helium, in which the coils are immersed. At this temperature, the

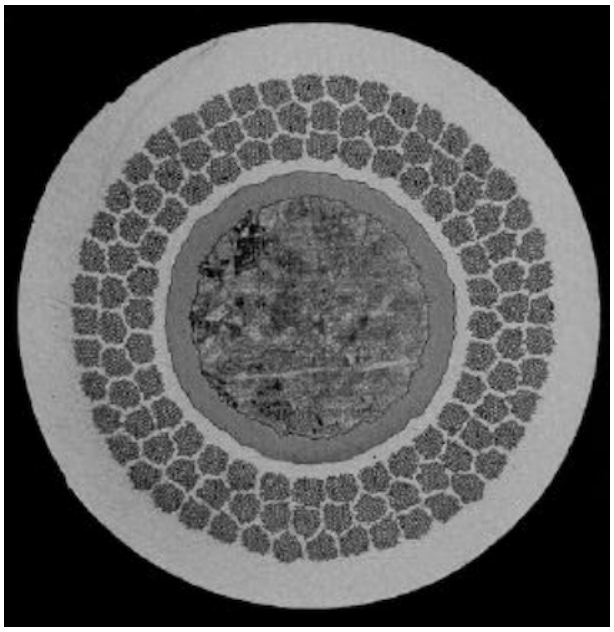


Figure 2.1: Cross-section of a superconducting wire of overall diameter 0.7 mm, containing about 6,000 filaments of 5 μm superconductor, Pantsyrny et al. (2009).

.

conductor's critical field strength (above which superconductivity ceases) is approximately 10 Tesla. The field strength in the centre of the magnet would be somewhat less than this. In a conventional 1.5 T clinical magnet, for example, the coils would reside in a maximum field of about 6.5 T (Pisanty, 2017).

The current carrying capability of the wire is also dependent on the thickness and number of filaments in the composite structure of alloy used. Figure 2.2 shows the effect of current and temperature of field strength. Niobium titanium NbTi is the standard 'work horse' of the superconducting magnet business. The figure shows the critical surface, which is the boundary between superconductivity and normal resistivity in 3 dimensional space. Superconductivity prevails everywhere below the surface, while resistance everywhere above it. The upper critical field (at zero temperature and current) and critical temperature (at zero field and current) which are characteristic of the alloy composition while critical current density depends on processing. Thus, because magnets usually work in boiling liquid helium, the critical surface is often represented by a curve of current versus field at 4.2K. (Thuries et al., 1991; Sharma, 2015).

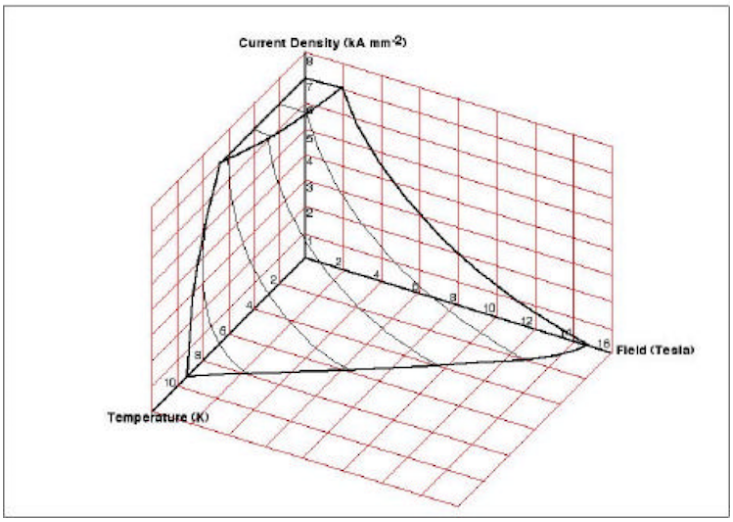


Figure 2.2: The operating parameters of a NbTi supercondutor,(Pisanty, 2017; Sharma, 2015).

2.1.2 Superconducting Magnets

The implications of using superconducting coils are that once they are energised to the desired current, the loop may be closed, the power supply removed and the current still circulates – providing the complete coil structure is maintained at a low enough temperature (Mark Brown, 2010). Surrounding the coils and radially outwards is a range of chambers designed to provide a thermal gradient to the outside world and prevent the helium liquid from evaporating. This is important as liquid helium is expensive and the longer time between refills the better. Convective losses are almost completely eliminated by evacuating the magnet's inner chambers, also known as the cryostat (Lvovsky et al., 2013). Radiation from the helium vessel to the outer cryostat is reduced by placing two radiation shields in the cryostat. The shields operate at approximately 20 K and 80 K respectively and may be cooled in one of two ways:

1. The outer shell in figure 2.4 can be bathed in a liquid nitrogen (77 K) and the inner one cooled by helium gas boil off.

2. a two-stage cryocooler in figure 2.3 may be used in which the Gifford-McMahon principle is invoked by using a closed helium gas loop.

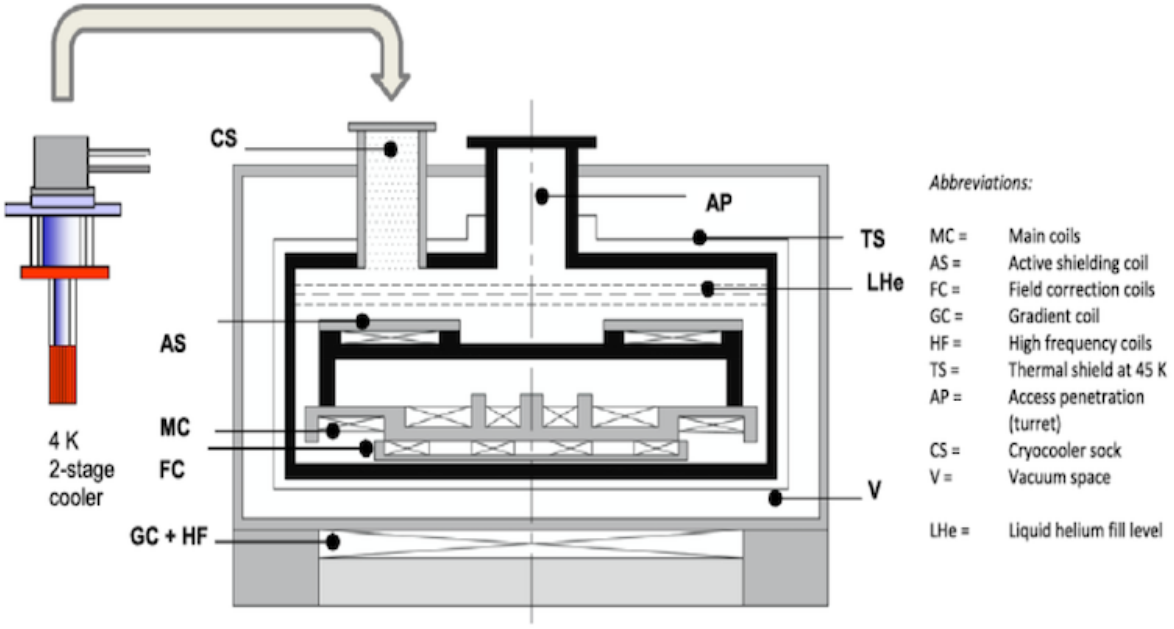
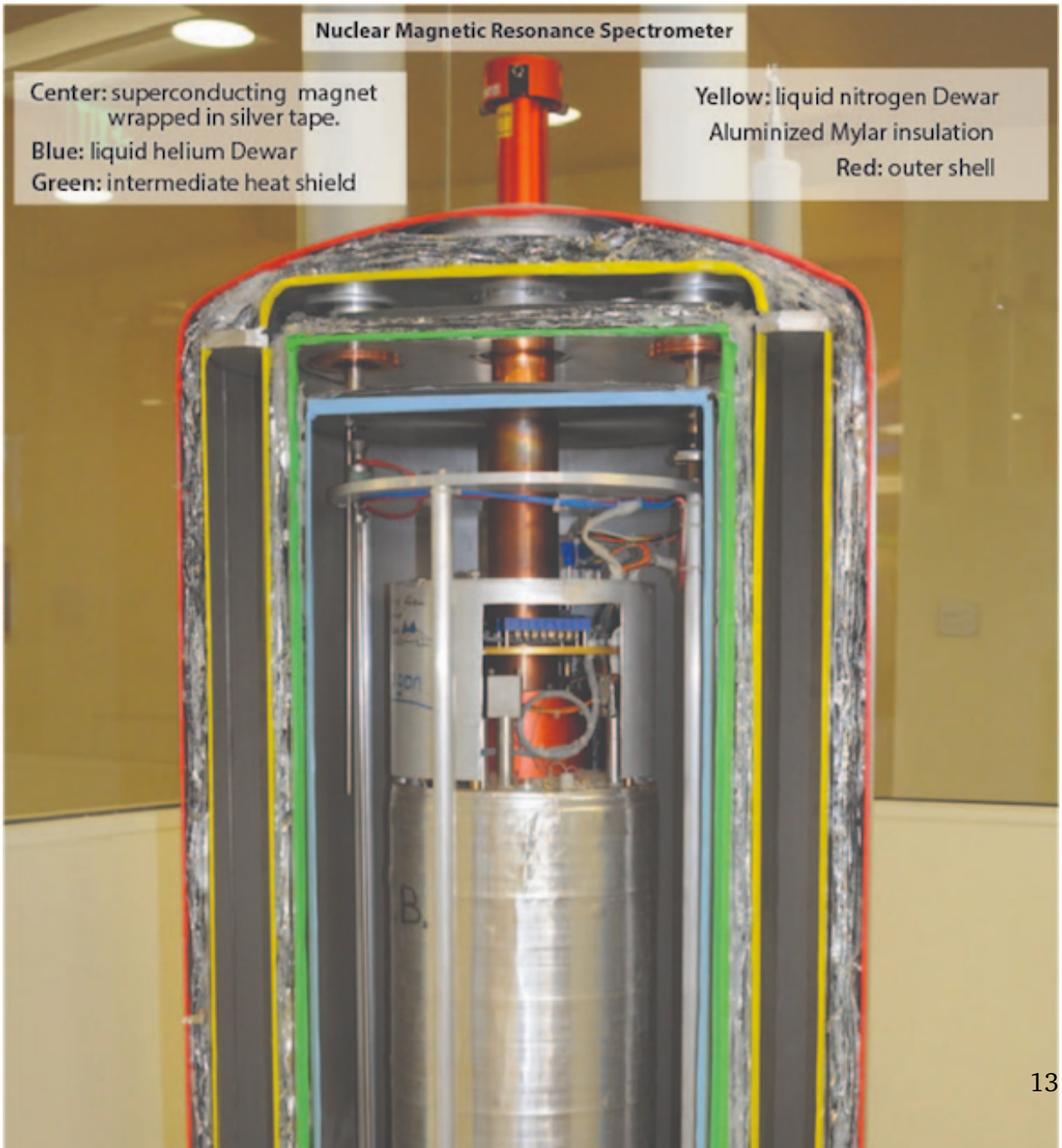


Figure 2.3: Cross-section of a typical superconducting magnet cryostat,(Lvovsky et al., 2013).



2.1.2.1 Two-Stage Cryocooler

In a two-stage 'cryocooler' system, the evaporating helium gas is collected and compressed by Closed Cycle refrigerator. The vaporized helium passes through the cold side of the train of heat exchangers and returns back to the compressor. The process of compression removes heat from the system and thereby cools the outer section of the cryostat, including the shields. Thermal radiative losses are further reduced by the use of many thin layers of super-insulation (aluminum covered Mylar – not dissimilar to space-suit material) over the gas shields (Lvovsky et al., 2013).
This can be viewed in figure 2.3.

2.1.3 Magnet Coils

Most Magnets use coaxial superconducting coils – the exact structure (position, dimensions, number of turns per coil, type of wire in each coil, etc.) of which requires very careful design. Most designs are such that a very pure magnetic field is generated at the centre of the magnet. Structure and all coils are connected in series and therefore carry the same transport current (several hundred Amps). The complete magnet has a huge inductance and therefore takes a considerable time to ramp to final field strength – this ramping or charging is achieved by attaching a power supply across the coil structure. This can be observed in figure 2.5 (McDougall and Bird, 1987).

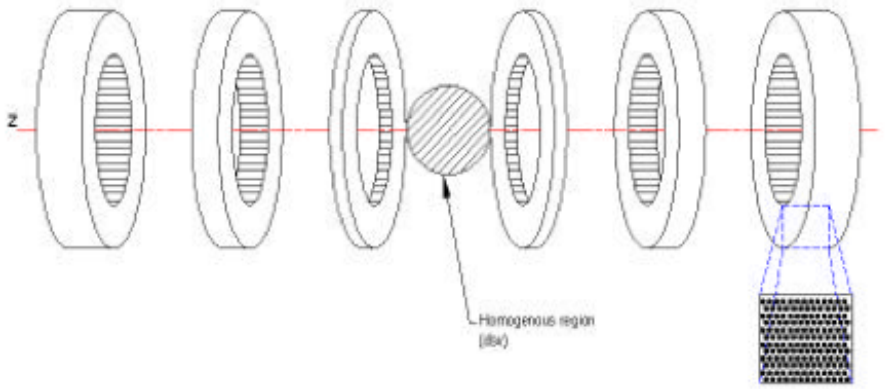


Figure 2.5: A generalised coil system, (De Graaf, 2013).

2.1.4 Magnet Shielding

Magnet designs are further complicated by the need to restrict stray or fringe fields that emanate from the system. The need for shielding is for:

- people working in the nearby environment must be within statutory exposure limits to static magnetic fields.
- any large metallic objects linking with significant field from the magnet will influence the central field homogeneity of the systems as well as the temporal effects of elevators.

In order to prevent flux leakage from magnet systems, two general methods of magnetic shielding have been developed: passive and active shielding. In passive shielding iron beams or steel plates are incorporated into the walls, ceiling, and floor of the magnet room. These materials concentrate magnetic flux lines close to the scanner. In some cases passive shielding material is applied to the outer surfaces of the cryostat or magnet shell. Passive shielding adds considerable weight and expense to MR siting and creates difficulties in achieving high homogeneity within the magnet bore itself. To overcome these limitations, actively shielded magnets were developed to become standard on all superconducting clinical scanners. Occasionally passive shielding is still required, but the amount of steel is significantly less than it would be otherwise. Although a number of 7.0 T magnets also have active shielding, additional passive shielding is usually required due to the very high fields involved. In active shielding, the fringe fields are suppressed within the cryostat itself rather than contained by ferromagnetic materials outside the scanner. An actively shielded magnet design incorporates at least one additional set of superconductive windings (shield coils) that oppose a portion of the external field generated by the main windings. These secondary shield coil windings are co-axial with the main windings and external to them, as shown in the image left and diagram below. The two coil sets are electrically connected oppositely in series and thus have fields pointing in opposite directions. For example, the main windings might generate a magnetic field of 2.0 T while the shielding coils generate a field of 0.5 T in the opposite direction. The net effect is a magnetic field of 1.5 T in the centre of the magnet. The usable field strength in the operating volume is reduced by the active shielding, the reduction effect on the fringe field is great. (Kanal et al., 1990).

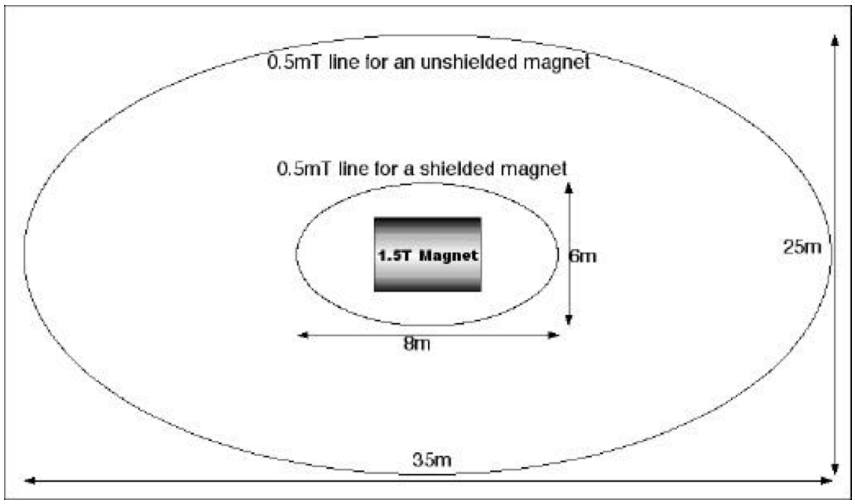


Figure 2.6: Schematic Diagram of Magnet Shielding

An ≈ eight Tesla (8 T) system is characteristically unshielded and uses approximately 420 km of superconducting wire. Figure 2.6 shows; The stray field in the axial direction is about 30 metres at the 0.5 mT (5 Gauss) level. This is normally the level of field quoted for shielding, as this is the currently permitted level for occupational exposure to static magnetic fields (Kanal et al., 1990).

2.1.5 Shim Coil & Shimming

Because any sample has its own magnetic field, materials in the probe, and ferromagnetic materials around the magnet , local magnetic field B_0 will be altered by loading sample to the bore of magnet. The field disturbance (inhomogeneity) within the dsv reveals necessity of shimming & the basis for classic shim-coil designs. The field homogeneities can be defined mathematically using spherical harmonics. Spherical harmonics have the distinct mathematical advantage of being orthogonal over the sphere of interest, and so if a coil structure is designed to just generate a single harmonic it theoretically does not interact with any of the other shims. This means by adjusting one shim coil current no harmonics (in B_0) other than that designated should be generated. In practice, this is not quite the case due to design and manufacturing imperfections and some shims do interact – typically a Z_2 shim generates a bit of Z and Z_0 (frequency shift) and perhaps also some X and Y (Romeo and Hoult, 1984).

2.1.5.1 Spherical Harmonics

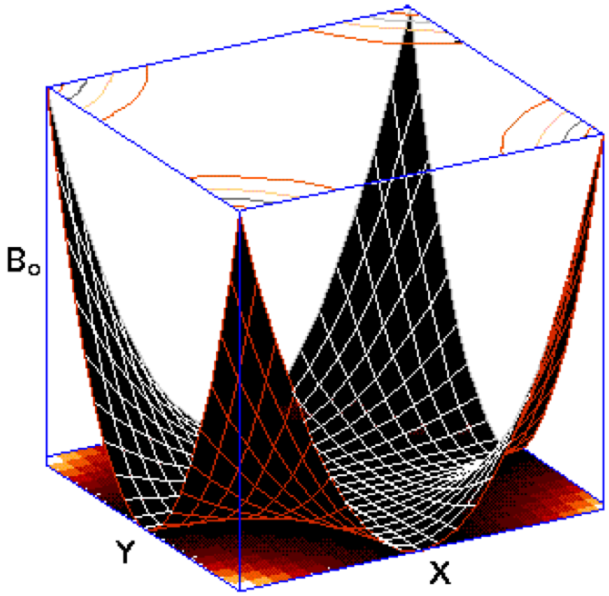


Figure 2.7: Tesseral harmonic $(x^2 - y^2)$,(De Graaf, 2013).

The field changes in value over the dsv, as a function of position. In an analogous fashion to time vs frequency (which has an inverse relationship), it maybe considered how regularly the field varies, which in turn corresponds to space vs spatial frequency. Another term for spatial frequencies is spatial harmonics, which if measured over a sphere are called **spherical harmonics** (Romeo and Hoult, 1984).

Along the z-axis these variations are easy to visualise and are called **zonal terms**. **Tesseral harmonics** in figure 2.7 are those without complete azimuthal symmetry, that is, they vary with x and y position (Romeo and Hoult, 1984).

2.1.5.2 Coils Design

In general, there may be as many as three classes of shims in MRI system. Typically, superconductive and/or passive shims will be used by the manufacturer to correct for manufacturing tolerances in the production process. Room-temperature shims is a term used for an array of electromagnets placed inside the magnet pore. These shims are controlled (the amount of current flowing through the coils in each coil is individually changed) by the console. Many commercial superconducting machines only make x, y and z shims available as room temperature shims. This is rapidly changing, however, as preclinical and clinical commercial systems move to higher field strengths and the installation of second order shims

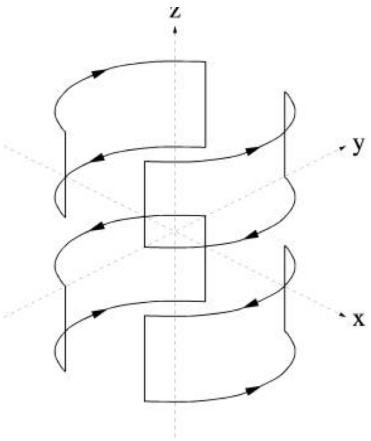


Figure 2.8: Shim coil designed to null spherical harmonic component of B_z,(De Graaf, 2013).

is becoming more common (and is highly recommended, particularly if spectroscopy is to be used). A shim coil in figure 2.8 is designed to create a small magnetic field B_0 which will oppose and cancel out an inhomogeneity in the main magnetic field B_0. Second order shims correct additional harmonics. Some typical second order shim names are $Z^2, XY, X^2 - Y^2$ (Bernstein et al., 2004).

The table 2.1 shows common names for shims and their Cartesian representation

2.1.5.3 Influence of Individual Harmonics

Although in imaging experiments, the spectrum of the NMR signal is rarely seen, it has a profound influence on the quality of the final image. In localised spectroscopy, of course, spectral information is paramount. This allows to observe the influence of the shims order (mentioned in table 2.1) on the impurity harmonics of water (initially) NMR spectrum in figure 2.9.

The spectral resolution, or the ability to discern between nearby peaks reduces if appropriate shimming is not performed to remove residual field impurities. After shimming the lineshape should be symmetric, have a narrow half-height and no lumps on the baseline. On most spectrometers, the shim coils are controllable by the computer (Romeo and Hoult, 1984).

Table 2.1: Common Shim 'Names' and their Cartesian Function,(De Graaf, 2013).

Names			
Degree (m^2)	**Order (n)**	**Function**	**Name**
0	1	Z	Z
0	2	$Z^2-(X^2+Y^2)$	Z^2
0	3	$Z[2Z^2-3(X^2+Y^2)]$	Z^3
0	4	$8Z^2[Z^2-3(X^2+Y^2)]+3(X^2+Y^2)^2$	Z^4
0	5	$48Z^3[Z^2-5(X^2+Y^2)]+90Z(X^2+Y^2)^2$	Z^5
1_c	1	X	X
1_s	1	Y	Y
1_c	2	ZX	ZX
1_s	2	ZY	ZY
1_c	3	$X[4Z^2-(X^2+Y^2)]$	Z^2X
1_s	3	$Y[4Z^2-(X^2+Y^2)]$	Z^2Y
2_c	2	X^2-Y^2	X^2-Y^2
2_s	2	XY	XY
2_c	3	$Z(X^2-Y^2)$	$Z(X^2-Y^2)$
2_s	3	ZXY	ZXY
3_c	3	$X(X^2-3Y^2)$	X^3
3_s	3	$Y(3X^2-Y^2)$	Y^3

The subscript c or s indicates either cosine or sine azimuthal dependence respectively

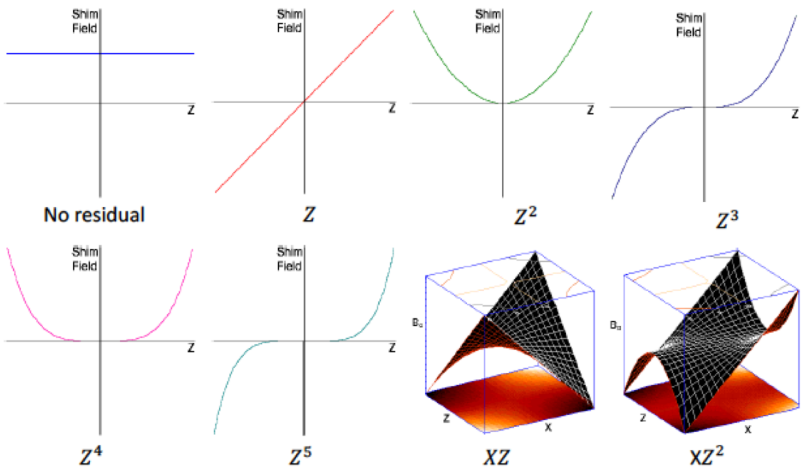


Figure 2.9: Images of zonal harmonics component of B_z, (De Graaf, 2013).

2.1.5.4 Passive and Superconducting Shims

Passive shimming refers to the use of thin pieces of steel placed in calculated positions in trays in the bore-tube of the magnet. These pieces of ferromagnetic material are used to shim the field. Passive shimming is normally performed by the installation engineers and remains in place thereafter. Superconducting shims are designed in the same manner as room temperature shims, but are placed in the cryostat and are generally energised during magnet installation to shim the dsv to specifications (Dorri et al., 1993).

2.1.6 Gradient Coils

Magnetic field gradients are used to encode the spatial position of the spins in a sample (subject) by varying the local magnetic field in a controlled manner. In addition to the static field, the gradient is imposed. This causes the Larmor frequency (ω_0) of the nuclear spins to vary as a function of their position (Lemdiasov and Ludwig, 2005).

Normally, the position ' spatial encoding' is achieved by varying the field in a linear manner with position. Not all magnets have gradient coils, also most NMR spectrometers do not have the hardware necessary to drive these coils. However, clinical MR scanners must have these coils. The gradient coils are usually working at room temperature (Keeler, 2011; Lemdiasov and Ludwig, 2005; Dorri et al., 1993).
There are desirable properties of gradient coil sets include:

- very linear (<5% impurities) gradients over the dsv.
- able to be pulsed very rapidly (gradient 'pulse' should have a rise-time in the order of 100-200 μs. Slew rate is an important property of pulsed gradients and is defined as the maximum gradient strength divided by the rise-time).
- the gradient coil set should have a low resistance to minimise power dissipation.
- gradients need to be shielded so that eddy currents are not induced in the magnet structure when the gradient is pulsed.
- torques and forces should be minimal, as should acoustic output and vibration.

2.1.6.1 The Maxwell Pair

First consider the design of a Gz gradient coil. The simplest system(in Figure 2.10) is two circular coils separated along the z-axis by a distance $2Z_1$. Current (I_c) in the two coils flows in opposite directions creating a magnetic field gradient (B_z) between the two coils. A coil pair is at optimal separation when

$$2Z_1 = \sqrt{3a} \tag{2.1}$$

where a is the coil radius. This coil pair is termed a Maxwell Pair (Hidalgo-Tobon, 2010). The gradient B_z(+) field at the center of one coil adds to the static magnetic field B_0, while the B_z(-) field at the center of the other coil subtracts from the static magnetic field B_0 (Hidalgo-Tobon, 2010; Keeler, 2011).

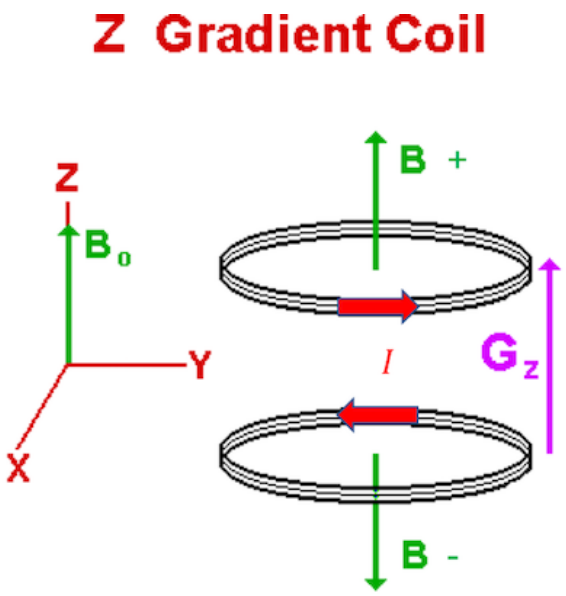


Figure 2.10: Z-Gradient coils, (Hidalgo-Tobon, 2010; Keeler, 2011).

2.1.6.2 The Golay coils

A similar process is shown at figure 2.11 to the design of G_z gradient coils may be followed to design transverse gradient coils G_x and G_y. The resultant designs tend to use a '4-loop' configuration around the circumference of the cylinder and are called Golay coils.
The function of these coils is to generate **field** in the Z-direction but that the additional field varies linearly with X or Y-position(shown in figure 2.12) (Lemdiasov and Ludwig, 2005).

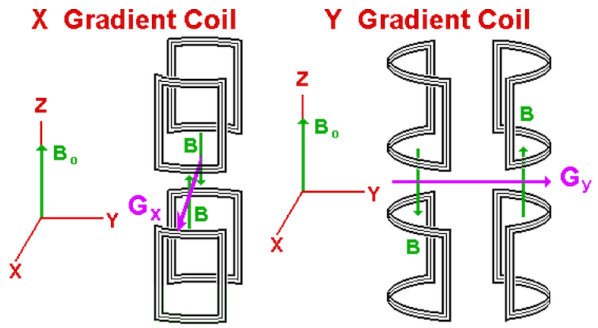


Figure 2.11: X and Y-Gradient coils, (Hidalgo-Tobon, 2010; Keeler, 2011).

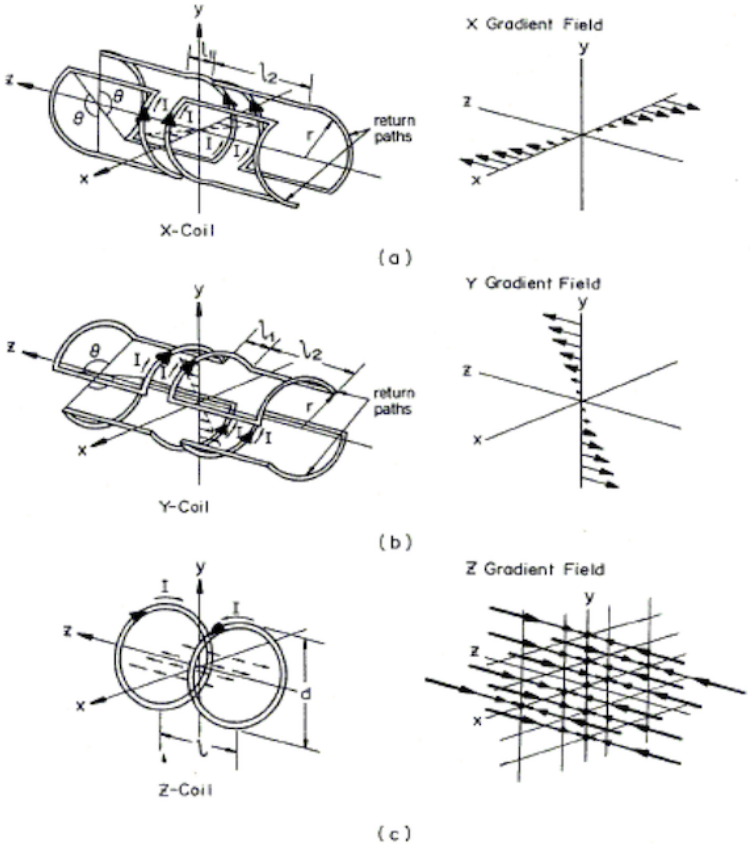


Figure 2.12: (a) X-gradient field path, (b) Y-Gradient field path, and (c) Z-gradient field path from X,Y,andZ coils respectively,(Lemdiasov and Ludwig, 2005; Keeler, 2011).

2.1.6.3 Shielding

Just as magnets need to be shielded to reduce stray fields, so do gradient coils. As gradient fields are pulsed, the fields that they generate outside the coil, link with other conductors and induce current in them called **Eddy currents**. These 'eddy currents' generate their own fields that act to generally oppose the initial fields generated by the gradient coil. The upshot

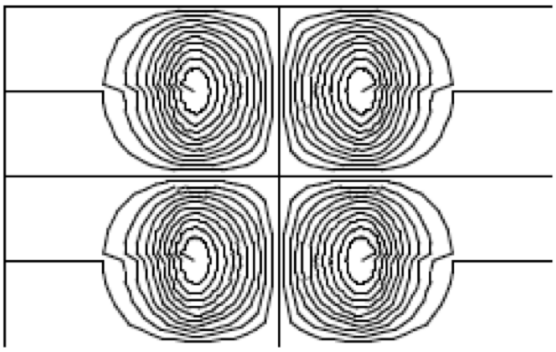


Figure 2.13: Shielding Coils,(Lemdiasov and Ludwig, 2005)

of this action is that the gradient rise-time (eddy currents are only induced by time-varying fields) is increased and therefore the slew rate is decreased. The generated gradient fields in the dsv are not only slower in response than desired, but the fields become also distorted (Dodd and Deeds, 1968).

There are two approaches to combat the unwanted eddy currents generated by pulsed field gradients:

1. Shielding the gradient coils by placing an additional layer of coils radially outwards from the 'primary' coils and which, while connected in series, are wound in the opposite direction to the primary (which is shown at 2.13). These 'shielding' coils are designed to reduce the leakage fields to the magnet and other cold structures which are particularly problematic due to their reduced resistivity (meaning longer acting eddy currents), but are also designed so that the total set delivers very linear gradients.

2. Shape the gradient waveform to reduce the effect of the eddy-current induced magnetic fields.

2.2 Probe

The devices that generate RF magnetic fields (B_1) at the Larmor or proper frequency of the nucleus being examined with the NMR spectrometer are termed RF coils, probes or resonators. The same coil that generates the RF field may also be used to receive the considerably weaker NMR signal at the same frequency. Alternatively, a separate coil, placed close to the sample may be used as a receiver coil. This section is concerned with the function and operation of

the rf probes in the NMR system and begins with an examination of the transmission field and transmission devices.

To begin with we describe some physics such as the Law of Biot and Savart, Electric Magnetic flux, and Faraday law. This will be followed by several parameters need to be considered such Resistance (R), Capacitance, (C), inductance (L) or called RCL circuit. The previous will be the basic physics of designing RF probe (Mispelter et al., 2006).

2.2.1 Law of Biot and Savart

Any movement by electric charge will generate a magnetic field that is given by:

$$dB = \frac{\mu_0}{4\pi}(Id\ell \times \frac{r}{r^2}) \tag{2.2}$$

where $Id\ell$ is the current element, $\mu_0 = 4\pi 10^{-7}\ \mathrm{H\,m^{-1}}$ is referred to the permeability of magnet in air core space. The magnetic field decreases when distance increases. It is measured in Tesla (T) (Mispelter et al., 2006).

2.2.2 Magnetic Flux

Represented by (ϕm) which describe the magnetic field per area unit by:

$$\phi m = BA\cos\theta \tag{2.3}$$

where B is the magnetic field, A is cross-area, and θ is an angle between the cross or surface area A and magnetic field vector B. Electric Magnetic flux (emf) is measured in Weber (Wb) (Mispelter et al., 2006).

2.2.3 Faraday's Law

This law states the change in magnetic flux in conductor (coil) or looped wire will produce a voltage at the two ends of constructed loop

$$V = [\frac{d}{dt}]\phi m \tag{2.4}$$

where V is voltage measured in Volts (V) (Mispelter et al., 2006).

2.2.4 Inductor

The inductance (L) is measured in Henry (H). For a simple solenoid coil the inductance is calculated by:

$$L = \frac{\mu_0 N^2 A}{\ell} \tag{2.5}$$

where N is the number of turns, A is referred to the cross section of coil area, and ℓ is referred the length of the coil. When a current increases, the opposing inductance will also increase. Thus, **Inductive Impedance** (Z_L) will increase as the frequency (ω) increases by:

$$Z_L = jL\omega \tag{2.6}$$

where Z_L is measured in ohms (Ω), $j = \sqrt{-1}$ Which represent the imaginary number, and ω is measured in radian per second (s^{-1}) (Mispelter et al., 2006).

2.2.5 Capacitor

It is the ability to store electric charge as energy. The capacitance is measured in Farad (F). An ideal capacitor is characterized by a constant capacitance C which is defined as the ratio of the positive or negative charge Q on each conductor to the voltage V between them. Capacitance is given by:

$$C = \frac{Q}{V} \tag{2.7}$$

where Q is the charge in coulomb.

Similar to the inductor, it has **capacitive Impedance** (Z_C). The impedance of the capacitor is given by :

$$Z_C = \frac{j}{C\omega} \tag{2.8}$$

The relation between the impedance Z_C and the capacitance is inversely proportional.

Thus, as capacitance decrease, the impedance increases. However, the relation between the capacitance C and the resonance Frequency ω_0 is similar to inductor. For example, if the capacitance increases, the resonance frequency will decrease however the impedance Z_C decreases (Mispelter et al., 2006).

2.2.6 RCL circuit

Matching resonated coil impedance Z to pure resistive impedance Z_0 indicate that coil reactance is compensated while the residual resistance R is converted to Z_0. Using capacitor C or adding another conductor achieves this. As capacitor C matching is more concerned in this work, capacitors may be connected parallel or serially with a coil inductor. Thus, we can describe the resonated circuit as parallel or series resonant circuit (Mispelter et al., 2006). When Equation(2.5) is combined with equation(2.6), then capacitor impedance Z_C compensates exactly Conductor Impedance Z_L by:

$$L\omega_0 = \frac{1}{C\omega_0} \tag{2.9}$$

When one well defined frequency ω_0 is known, the eqaution is simplified to

$$LC(\omega_0)^2 = 1 \tag{2.10}$$

The relation between the inductance L and frequency f_0 is clearly noticed by:

$$\frac{1}{\sqrt{LC}} = 2\pi f_0 \tag{2.11}$$

Inductance L of coil has an inversely proportional relation to the resonance frequency f_0 . For instance, if the inductance in the coil of wire increases, the resonance frequency on this coil will be decreased.

2.2.6.1 Concepts of Resonance

To understand the concept of resonance, a simple RF coil and equivalent circuit is explained by using the Kirchhoff's law, the current flowing in the RLC circuit is given by:

$$I_c = V(R + \frac{j}{C\omega} - jL\omega)^{-1} \tag{2.12}$$

where I_c is the current, and R is the resistor. If R = 0, then the equation is rearranged to become:

$$I_c = V(\frac{L}{j\omega}(\omega^2 - \frac{1}{LC}))^{-1} \tag{2.13}$$

The current (I_c) flowing in the circuit will become infinite (∞) and impedance (voltage/current) will be zero,when

$$\frac{1}{\sqrt{LC}} = \omega_0 = \omega \tag{2.14}$$

The figure 2.14 below shows the simple RCL circuit where L is the inductance, C is the capacitor, V is the voltage, R is the resistor, and I_c is the flowing current in the circuit (Mispelter et al., 2006).

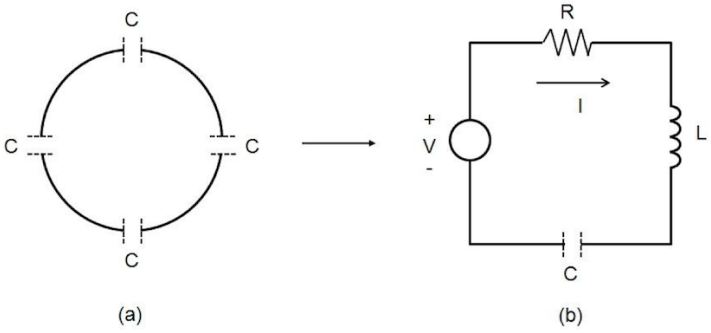


Figure 2.14: (a)a single-loop RF coil and (b) RLC circuit,(Mispelter et al., 2006).

2.2.6.2 Tuned circuits

The elements in an antenna can be broadly grouped into inductive, capacitive and resistive elements – each of which has a different frequency response. If the input impedance of a circuit is measured at a variety of frequencies, there is usually a frequency at which the impedance of the inductive components are equal but of opposite sign to the capacitive impedance and leads to a low impedance circuit. This is the resonance frequency of the (tuned) circuit. It is normal to provide adjustable components to fine tune the resonance

frequency of the circuit to the desired frequency (Mispelter et al., 2006). Figure 2.15 shows the recommended curve condition.

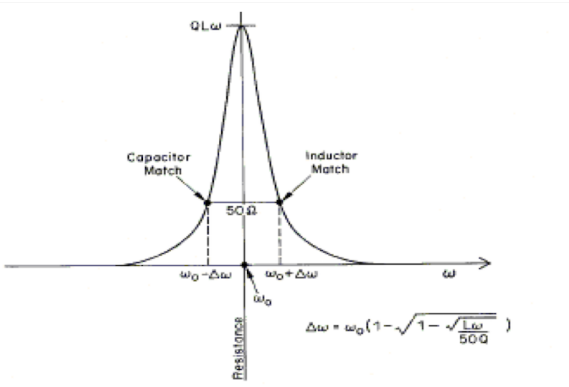


Figure 2.15: The resonance curve – the centre of the curve is the desired condition.

2.2.6.3 Matching

Not only is it important to ensure that the probe is tuned to the appropriate frequency, but also that the impedance at that frequency is the same as the rest of the RF circuitry so that there is no wave or power reflections. Consider the waves in a swimming pool: they reflect from the edge of the pool if the water level is less than the edge level. If the water laps over the edge, however, there is little reflection and the surface of the pool is calm and offers reduced resistance to swimmers. The same general principle applies here – additional circuitry is applied to ensure that the RF pulse 'sees' a lap over rather than a reflection, and that maximum power is transferred to the RF probe from the RF amplifier (Mispelter et al., 2006).

In most modern scanners tuning and matching circuitry is adjusted to the patient (load) during the pre-scan sequence and a transmission circuit impedance of 50 Ω ohms is common in MR RF systems as shown in figure 2.15 (Mispelter et al., 2006). Tuning and matching are manually adjusted in preclinical (laboratory) NMR spectroscopy system which could be seen in figure 2.16.

2.2.7 Quality Factor

One parameter that is often quoted for probes is the quality factor (Q). The quality factor of a coil is symbolized as Q. It explains how the coil losses or keeps the energy with time t.

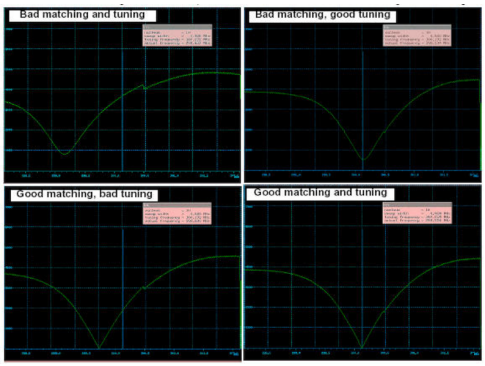


Figure 2.16: The tunning and matching stages– the centre of the curve is the desired condition.

This is the ratio of the 3 dB frequency-width of the impedance curve to the central frequency $\frac{f_0}{\triangle f}$ (Mispelter et al., 2006).

$$Q = \frac{L\omega}{R} \tag{2.15}$$

The introduction of a conductive sample should reduce Q as this indicates that the probe is producing strong RF fields (B_1) in the sample. Desirable properties in terms of Q factors are then a high Q for an unloaded condition, as this indicates minimal resistance R.

The unloaded Q factor is denoted Q_0,

$$Q_0 = \frac{2\pi f_0 C}{G_0}$$

G_0 represents the dissipation inside the resonator. Typically, this dissipation is caused by conductor losses and by dielectric losses. loaded resonator that has slightly different resonant frequency. When conductance G_{ex} comes in parallel to G_0, thus lowering the overall Q to a new value Q_L , which is expressed by writing as

$$\frac{1}{Q_L} = \frac{1}{Q_0} + \frac{1}{Q_{ex}}$$

The external Q factor is defined in analogy as

$$Q_{ex} = \frac{2\pi f_0 C}{G_{ex}}$$

G_{ex} represent power dissipated in the external circuit. The ratio of power dissipated in the

external circuit to the power dissipated in the resonator is called coupling coefficient κ. As both G_0 and G_{ex} have common voltage V, the ratio of powers is proportional to the ratio of conductances

$$\kappa = \frac{V^2 G_{ex}}{V^2 G_0} = \frac{G_{ex}}{G_0} = \frac{Q_0}{Q_{ex}}$$

When an equal amount of power is dissipated in the external circuit as in the resonator itself, the coupling is said to be critical, and the coupling coefficient in this case is κ=1. An under-critical coupling means that more power is dissipated in the resonator than in the external circuit, while an overcritical coupling means that more power is lost in the external circuit than in the resonator. By eliminating Q_{ex}, the relationship between the unloaded and the loaded Q become as

$$Q_0 = Q_L(1+\kappa)$$

As soon as the measurement starts, the resonator is loaded by the external circuit (here the network analyser). This measurement will produce the loaded Q.

Upon introduction of a lossy (conductive) sample the Q should drop considerably; The greater the unloaded Q and the larger the Q drop for a fixed sample, the greater the signal-to-noise ratio that could be expected from that probe (Mispelter et al., 2006).
On other words, A high Quality Factor Q suggests a high inductance L but low resistance (losses) R while a Low Quality Factor Q suggests a low inductance L but high resistance (losses) R (Mispelter et al., 2006).

2.2.8 Shielding

When pulsing a transmitter coil it will radiate externally as well as internally. External radiation can interfere with the operation of the gradient coils and allow noise to enter the RF coil. Most transmission coils are therefore shielded. The shield consists of one or more layers of conductors external to the coil. In some systems the shield is mounted on the inside face of the gradient coils. Care must be taken to ensure that the shield does not introduce additional eddy currents when the gradient coils are pulsed and hence shields are usually slotted or constructed in a spiral pattern to avoid large continuous regions. The shield also acts as a ground-plane and can improve the sensitivity and homogeneity of the

coil. Receive-only coils do not require shields (Mispelter et al., 2006).

2.2.9 Coil Geometry

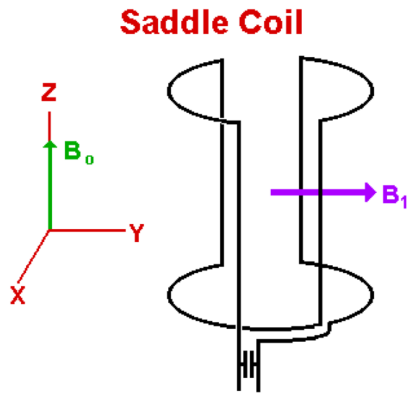


Figure 2.17: Saddle Coil Design, (Hidalgo-Tobon, 2010; Keeler, 2011).

There many classifications of RF coil geometry however, most RF coils on NMR spectrometers are of the saddle shape and work as the transmitter of RF field B_1 and receiver of RF signal from the sample (Mispelter et al., 2006).

Most of the research in this thesis are performed with home built low-field resonance probe consists of three windings with saddle-coil geometry with 30 mm probe diameter. It is optimized to resonate at a frequency of 15.385 MHz for hyperpolarised Krypton ^{83}Kr gas.

2.3 Operator Console

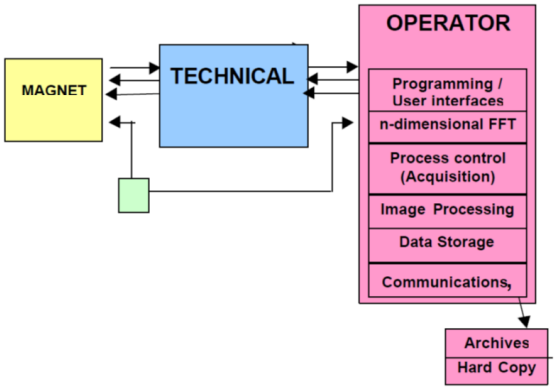


Figure 2.18: schematic diagram of operator console and its connection

The operator room contains a central computer workstation which controls the overall system and provides a graphic display of images. Associated with the main computer

are a number of dedicated co-processors. This distribution allows faster control and data throughput, which in turn allows faster image acquisition and processing, and therefore greater subject and operator throughput.

- Programming / User interfaces – allows easily selectable imaging sequences, parameters and image locations of the subject (sample).
- n-dimensional FFT – for the rapid reconstruction of 2D and 3D images.
- Process control (Acquisition) – takes the high-level sequence selections and controls the timing of pulses to the rf, gradient, and acquisition systems.
- Image processing - image processing workstations, data archiving and hardcopy equipment such as cameras, printers, etc.
- Data storage – each sample may have a large number of images for each examination or experiment.
- Communications – transfers data and connects to other systems

2.4 Technical Equipment

The Technical equipment contains a transmitter unit, which formulates and shapes the required RF pulses, and sends them to the coil. Gradient coils pulses are also shaped, amplified and sent to gradient.

The returning MRI signal is accepted by a receiver unit which demodulates, filters and then converts the analogue signal to a digital form.

A variety of amplifiers are used to boost the outbound pulses and the returning signal:

- Transmitter unit – generate a transmitter pulse, either selective or non-selective at the desired frequency and of the correct shape. Note that the frequency synthesiser is also linked to the receiver unit.
- Gradient boxes – three channels (X,Y,Z) of gradient pulses are shaped and amplified here to drive the gradient coils.

- RF high power amplifier – the rf transmission pulses are amplified to high power levels.For body coil in clinical scanner the pulse level usualy 15 kW.

- Circulator, Duplexer (is a passive device that implements frequency-domain multiplexing and allow only the required frequency to pass). Also, further protection is provided by a duplexer that isolates the receiver coil and sensitive MR pre-amplifier from the transmission (high power) circuit. Consider the simple circuit. When the transmitter is on and the input is of sufficient level, diode sets A and B conduct and act as short circuits. The rf pulse passes through set A, and set B effectively shorts the quarter wavelength transmission line to ground. The quarter wavelength line effectively transforms the short circuit B to an open circuit at A. This protects the pre-amplifier and ensures that the power flow is to the transmitter coil as desired. After transmission, the diodes cease conduction and return to being high impedance – there is now a direct connection between the probe and the receiver as the NMR signal level is too low to activate the diodes., Isolators, Pre-Amplifiers, and Tuning devices – all of which are associated with the efficient transmission of rf pulses and/or reception of the NMR signal.

- Safety monitoring – Federal regulations limit the amount of rf power that may be delivered to the patient and also the size and rise-time of the gradient pulses. This unit monitors the levels of rf and gradient pulses and shuts down the amplifiers if the levels become unsafe.

- 2nd stage amplifier – further amplifies and filters the NMR signal.

- Receiver unit – With input from the frequency synthesis unit, this unit demodulates the NMR signal to baseband frequencies (remembering that NMR signals are usually at frequencies of many MHz), filters the signal to a bandwidth set by the type of sequence being used, and then converts the signal from analog to digital for computer input, storage and processing.

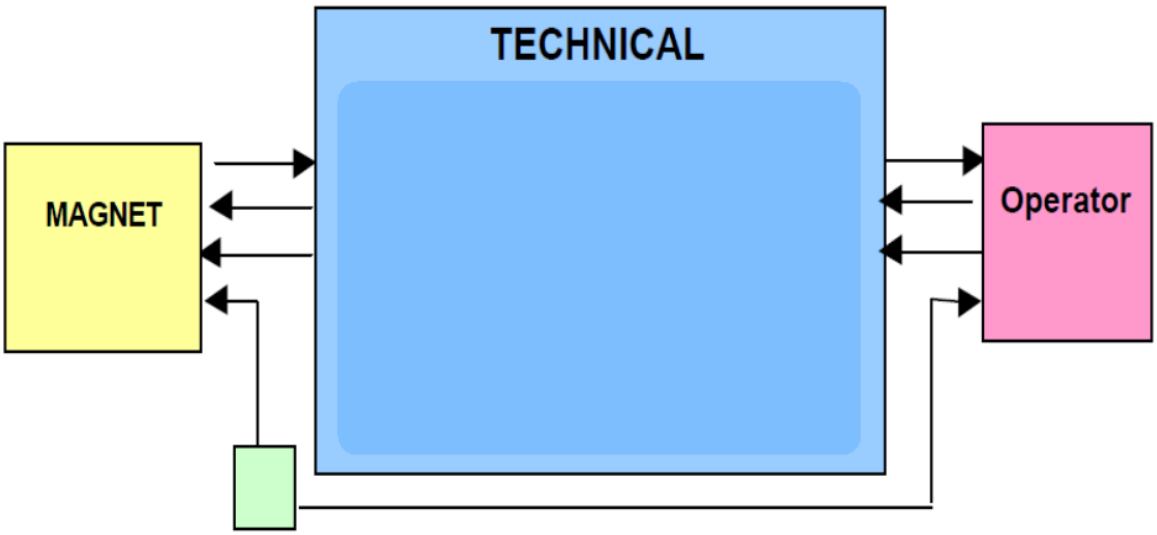


Figure 2.19: schematic diagram of technical equipment and its connection

CHAPTER 3

MR SIGNAL RELAXATION

Relaxation describes how signals change with time. In general MR signals decay with time, to generate broader and weaker signals. The deterioration enhances the fact that MR signal is a result an excited state of thermally equilibrium magnetisation. Relaxation is the conversion of this non-equilibrium magnetisation to a normal state. In other words, relaxation describes how fast nuclear spins "recover" the direction in which they are oriented.

The rates of this spin relaxation can be measured in both spectroscopy and imaging applications. MR signal relaxation is understood in terms of two independent processes, each with their own time constants:

- Spin lattice relaxation (T_1)
- Spin spin relaxation (T_2)

3.1 Spin Bundle

To begin with, let us first define the spin bundle before describing the relaxation. It is more convenient to describe this on a microscopic picture. Spin bundle is a group of spins experiencing the same magnetic field strength inside a sample. In figure 3.1A, the spins in the bundle are in random motion and distributed. Once the magnetic field B_0 is applied, the spins bundle gets aligned with magnetic field B_0. Figure 3.1B shows the effect of magnetic

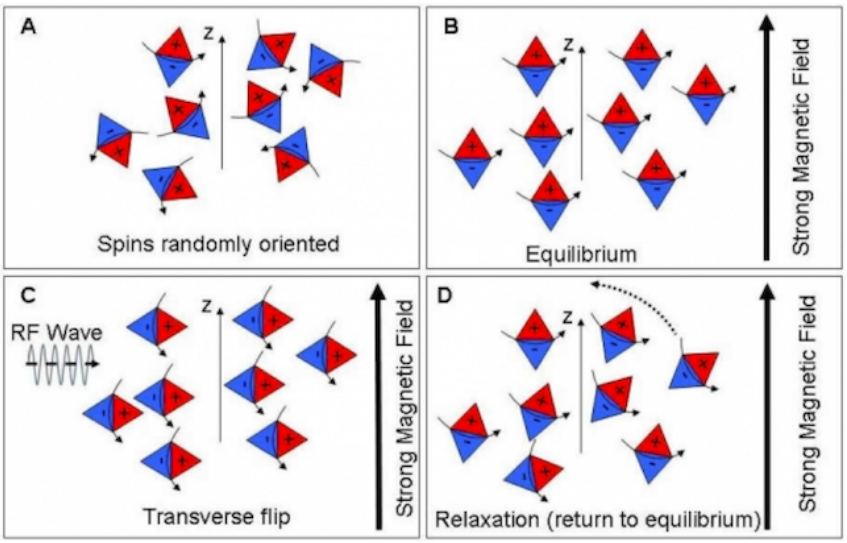


Figure 3.1: The effect of magnetic field B_0 on spin

field B_0 on the spin bundle. The sum of the spin vector from all spins are presented as net magnetisation vector which is observed in figure 3.2 (Dale et al., 2015).

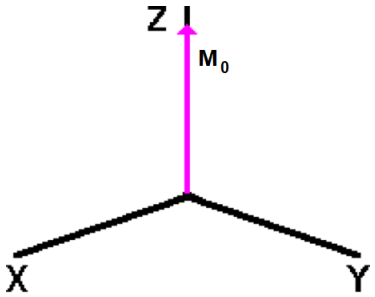


Figure 3.2: Net Magnetisation Vector

3.2 Spin-lattice Thermal Relaxation

At equilibrium the net magnetisation vector seen in figure 3.1B lies along the direction of the applied magnetic field Bo and is called the equilibrium magnetization M_0 which equals the Z component of magnetization M_Z. In this configuration $M_Z = M_0$ observed in figure 3.3, while M_{X-Y} in transverse plane does not exist (Callaghan, 1993; Bloembergen et al., 1990).

The time constant which controls how M_Z returns to its equilibrium state after RF wave is applied in the presence of B_0 field is called the longitudinal relaxation time (T_1) as seen in figure 3.1D. The T_1 signal as a function of the repetition time (TR) after its displacement is governed by the equation:

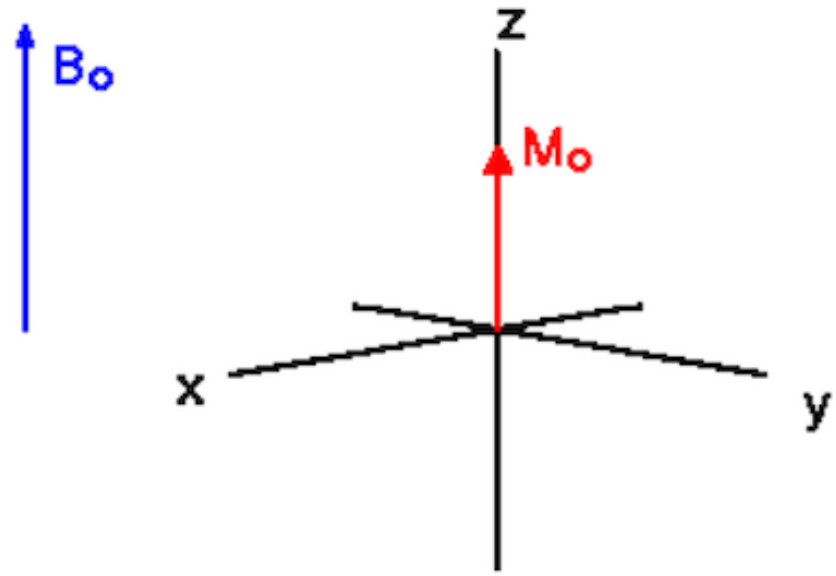


Figure 3.3: Equilibrium Magnetisation $M_Z = M_0$

$$M_Z = M_0(1 - e^{-\tau/T_1}) \tag{3.1}$$

There are two main method to measure T_1 relaxation;

- Saturation recovery technique.
- Inversion recovery technique.
- Spin echo (this will be discussed in detail later in this chapter)

3.3 Saturation Recovery Technique (Thermal Sample)

Saturation recovery technique is a repeated applications of 90° RF pulse, separated by a repetition time (TR), for a sample with a relaxation time, T_1. The first pulse generates transverse magnetization with amplitude M_0. At this point M_Z=0. During the subsequent time M_Z starts to increase or recover. This technique fulfil the condition of Equation 3.1(Rutherford and Bydder, 2002; Currie et al., 2013).

If TR is half of T_1, then the new M_Z is 60% of initial M_Z. Thus, the next 90° RF pulse will produce a smaller amount of coherent transverse magnetization. This is called **saturation** (Weishaupt et al., 2008).

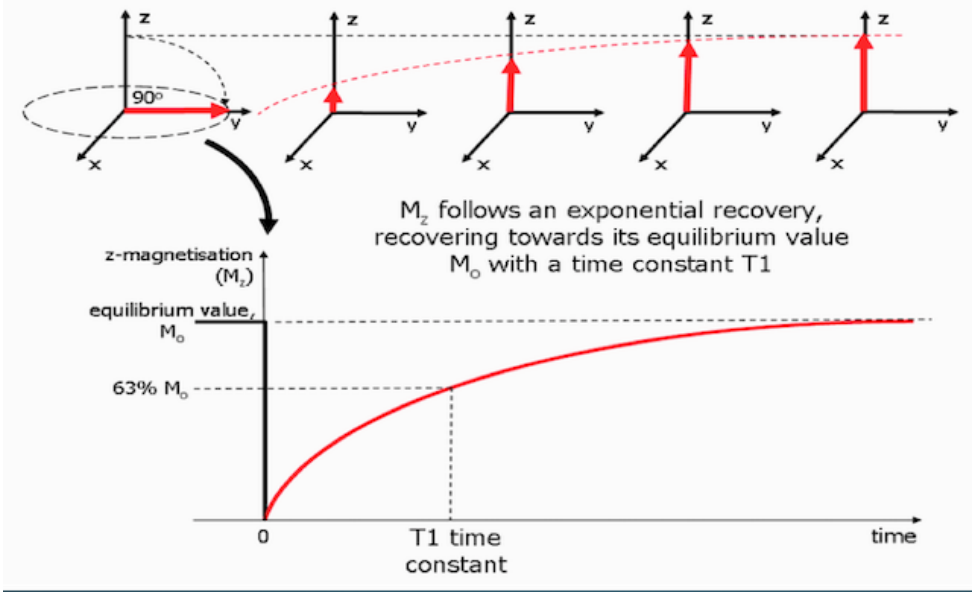


Figure 3.4: Saturation process

3.3.1 Signal Intensity using Saturation Recovery from Thermal Sample

To begin a pulse sequence, the spins must be rotated into the transverse plane by an RF pulse (normally a 90° pulse). In figure 3.5, the observed signal is dependent on the spin dephasing in the transverse plane. However, the spins are also relaxing back to be aligned with a magnetic field, B_0. This longitudinal relaxation time is T_1. while in (figure 3.6) the maximum signal for the next pulse sequence is only available if all the spins have relaxed back and aligned with B_0. This effectively occurs at five times the T_1 relaxation time (Westbrook and Talbot, 2018; Fleckenstein et al., 1991).

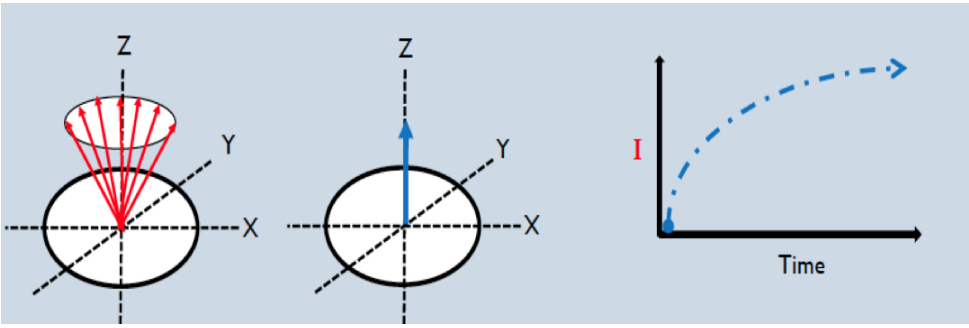


Figure 3.5: T_1 process

If TR is less than $7\times T_1$, the signal from consecutive echoes decreases. In the extreme case, a zero-net signal is detected in the transverse plane. However, in most situations a **steady state magnetization** is reached, where the signal becomes a fixed percentage of the maximum signal (Westbrook and Talbot, 2018).

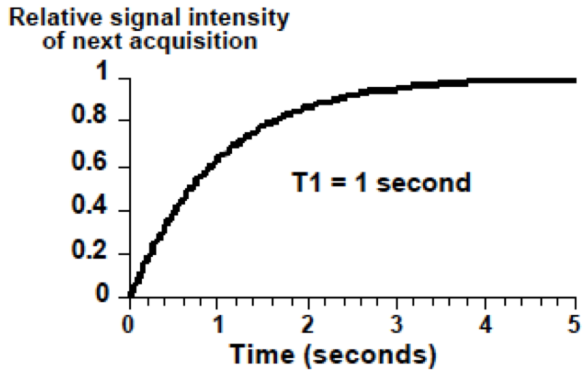


Figure 3.6: Signal Intensity from Steady State Process

The magnetization is relatively governed by the pulse angle and recovery time while the signal intensity (I_s) is relatively governed by the amount of magnetization in the x-y plane or called Transverse magnetization (Westbrook and Talbot, 2018).

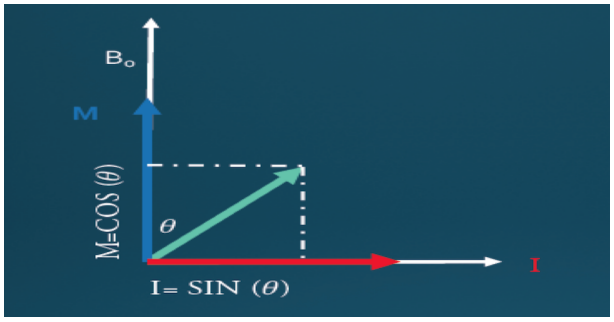


Figure 3.7: Relation between Signal Intensity and Magnetization

The spin magnetization is relatively calculated by the equation:

$$M_0 = \cos\theta \tag{3.2}$$

While the signal intensity is calculated by equation:

$$I_s = \sin\theta \tag{3.3}$$

As an example, if the pulse angle is 90°, then the longitudinal magnetization is cosine 90° that equal zero. This means the signal intensity is sine 90° equal to one. Thus, all magnetisation is now in the x-y plane with full signal intensity. To acquire a signal for T_1, a time (τ) need to be waited for the magnetization to recover back to the Z plane. Figure 3.7 shows the spin magnetisation orientation according to the flip or pulse angle.

3.3.2 Saturation and Image Contrast

For images to have contrast, there must be intensity variation (normally displayed as varying shades of grey) between different tissues. Contrast in MRI images occurs because of the different signal strengths acquired by the receiver coil for given acquisition parameters, as a result of the range of tissue types within the sample volume.

In a T_1-weighted image, the contrast is obtained by exploiting the differences in the T_1 relaxation times of the tissues being examined. It has been noted previously that after the application of 90° pulse, M_Z begins to recover during the time TR. The rate of recovery is dependent upon the type of tissue.

Typically, fat has a very short T_1 while water has a long T_1-value. In order to achieve T_1-weighting, the TR must be short enough such that full longitudinal recovery is not reached for any tissue within the sample. If the TR is too long, all tissues will have fully recovered and differences in T_1 will not be apparent.

When TR is short and tissue has not fully recovered in M_Z direction, the signal from subsequent 90° pulses will be affected by partial saturation. Because there were different amounts of longitudinal magnetisation in the tissues before the subsequent 90° pulses, there will be different amounts of transverse magnetisation after the pulses, and image contrast is produced. Figure 3.8 shows the effect of changing TR on image contrast (Westbrook and Talbot, 2018; Fleckenstein et al., 1991).

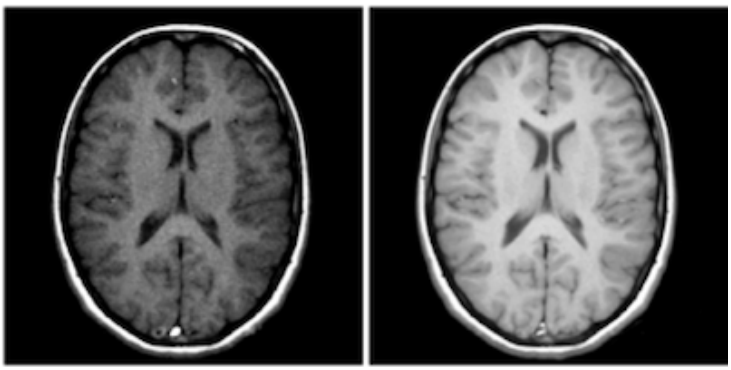


Figure 3.8: T_1 axial images of the brain. Contrast of brain images reduces with increasing TR values – (right) TR = 140 ms; (left) TR = 460 ms, (Westbrook and Talbot, 2018).

3.4 Inversion Recovery Technique (Thermal Sample)

If a 180° pulse is applied to M_z, the magnetizations will rotate to Z direction. This is called an inversion pulse (which can be seen in figure 3.9). When the inversion pulse is followed by a $\pi/2$ (90°) pulse after a time TI, which will rotate the magnetization from M_z to M_{xy}. TI is known as the inversion time. The TR is the time from the first 180° pulse to the second 180° pulse of the next acquisition. Figure 3.10 shows an inversion recovery sequence.

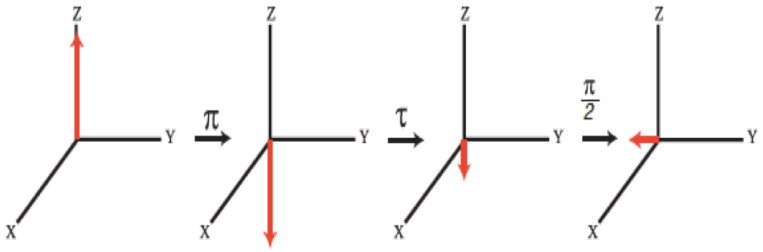


Figure 3.9: Magnetization Pattern of Inversion Recovery

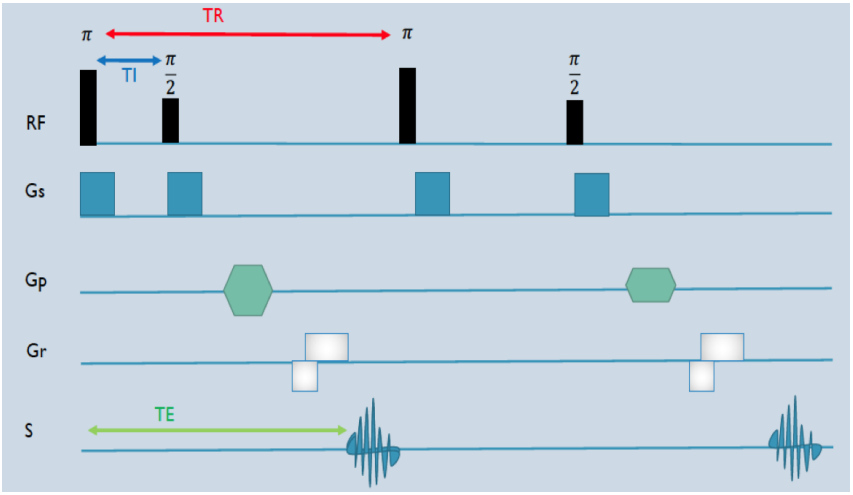


Figure 3.10: Inversion Recovery Sequence

3.4.1 Inversion Recovery and Image Contrast

In an inversion recovery sequence, a π-pulse is initially applied which is then followed some time later by a $\pi/2$ -pulse. The time between the application of these two pulses is known as the inversion time, TI.

In order to achieve contrast in an inversion recovery images, the relaxation of the various tissue components during TI is exploited. In these images, contrast is primary controlled

by the length of TI. Medium length TI will demonstrate large contrast differences between tissue types, while a long TI will result in less contrast in these images. This is due to greater relaxation of the tissues, and the effect of the π pulse is negated . The inversion recovery sequence has the ability to produce a heavy T_1 weighted images contrast, if proper TI parameter is used.

The signal intensity from this sequence is also governed by the TR time. The TR plays a major role in the signal intensity of the sequence. Thus, reducing the TR, causes a reduction in echo intensity related to tissues or fluids contain the long T_1 value such as cerebrospinal fluid (CSF). Figure 3.11 shows the effect of TI on image contrast (Westbrook and Talbot, 2018; Keeler, 2011; Fleckenstein et al., 1991).

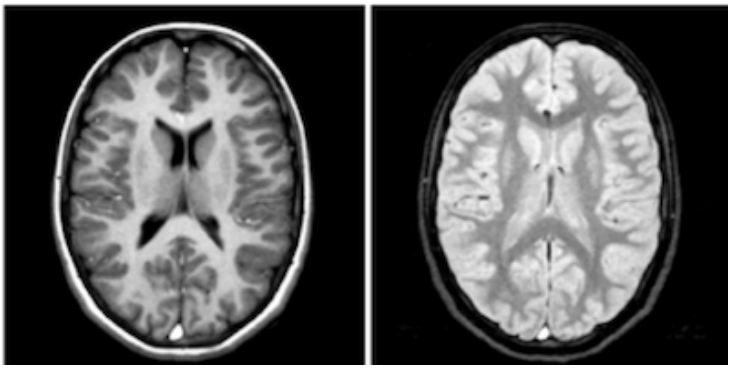


Figure 3.11: Inversion recovery axial images of the brain. Contrast of brain images reduces with increasing TI values – (left) TI = 165 ms; (right) TI = 600 ms (Westbrook and Talbot, 2018).

The inversion recovery technique is another way to fit T1 time. However, this technique is not useful when hyperpolarised gas is used. The magnetization from hyperpolarised gas do not recover back and all magnetization will be lost following the first 180 pulse.

3.5 T_1 relaxation using (HP Sample)

Combining the previous saturation technique with HP gas is not practical. Because once the HP gas magnetizations is used, they does not recover back. Therefore, to make this technique work with HP gas a slight modification would be induced to the technique by using a consecutive HP gas delivery to a subject. Every time a signal is need to be acquired using a pulse and collect experiment, a HP gas is delivered before the beginning of the experiment. Figure 3.12 shows the modification applied to the technique during sequence application.

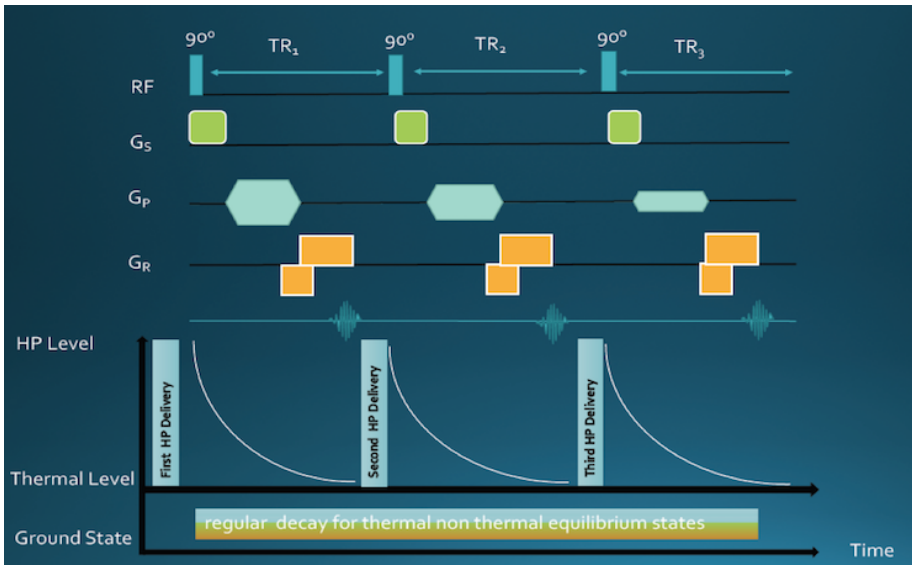


Figure 3.12: T_1 relaxation using saturation method with HP sample

The combination of this technique with HP system will create a signal intensity. The T_1 relaxation time is then measured from the maximum data points of signal intensity from the free induction decay (FID) at different time delay (τ) that is proportional to spin density which is called **peak height** calculation method as shown in 3.13.

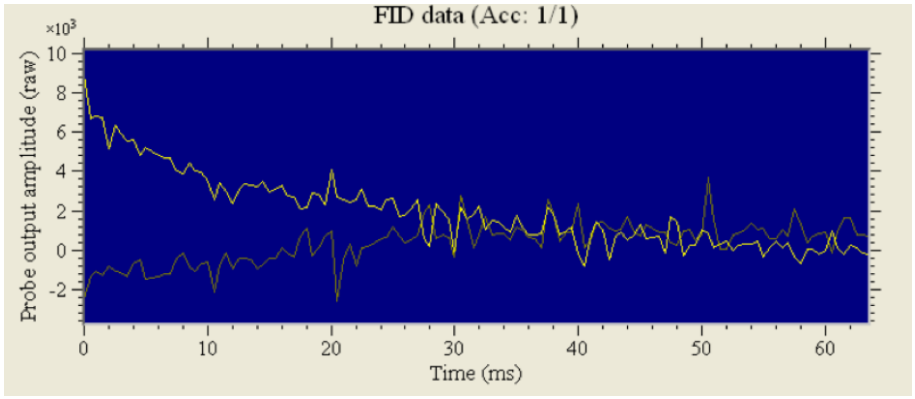


Figure 3.13: FID of HP sample

The other method is to integrate the area under the complex spectrum (Fourier transformed signal), which is displayed in figure 3.14. This is known as **integration**.

For smaller pulse angles, the decrease in M_z is much less than the increase in M_{xy} per degree of rotation. For large pulse angles, the decrease in Mz is much greater than the corresponding increase in M_{xy}.

The change in the longitudinal (M_z) and transverse magnetization (M_{xy}) by applying pulse that turns the spins by less than (90°), would be an ideal alternative way to combine with HP system. This would help the user to use some of the magnetization from the HP

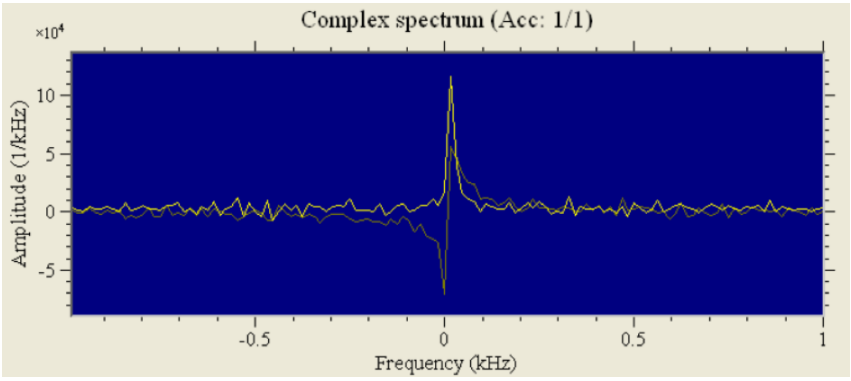


Figure 3.14: Integration of the Spectrum

gas during the sequence and then use the remaining HP magnetization by applying another pulse angle to finish the whole scan in one HP delivery. This is principally accomplished by using a series of fixed small flip angle radio-frequency (RF) pulses that are evenly spaced.

Theoretically, applying fixed flip angle (FFA) allows signal intensity (S_n) of hyper polarized gas to decay with each RF perturbation by:

$$S_n = M_1[\cos\theta \times \exp^{\frac{-TR}{T_1}}]^{n-1}, n = 1, 2, 3, 4, ...n \tag{3.4}$$

While S_n is signal intensity, n is the total number of excitations, M_1 is the leftover magnetization, θ is the flip angle, TR is the repetition time, and T_1 is the longitudinal magnetization. If we used a fixed angle of 5° thus 1% of the HP magnetization is used leaving 99% as leftover to be used for the next excitation. The next 5° pulse will use another 1% of leftover magnetization leaving 98% to be leftover. This will continue until the whole 90° is completely finish using 18 excitation pulse.

3.6 Spin-Spin Thermal Relaxation

The spin-spin relaxation, also called (transverse relaxation or T_2 decay) time is a measure of the rate at which phase coherence is lost. The 'transverse decay time, T_2, is a process due to the interactions of the tumbling magnetic dipoles and is a function of the chemical and physical environment. In addition, there is the dephasing due to inhomogeneities in the B_0 magnetic field as well. The combination of the transverse relaxation is often called $T_2^\star$ according to the equation:

$$\frac{1}{T_2^\star} = \frac{1}{T_2} + \frac{\gamma \Delta B_0}{2} \tag{3.5}$$

where ΔB_0 is decay caused by field inhomogeneity.

After RF application, the magnetization is flipped into the x-y plane in figure 3.15. The magnetization in the transverse plane (M_{XY}) immediately after RF excitation will start to disperse around z-direction, which can be defined using the equation:

$$M_{XY} = [\cos\theta] \exp^{-TR/T_2^\star} \tag{3.6}$$

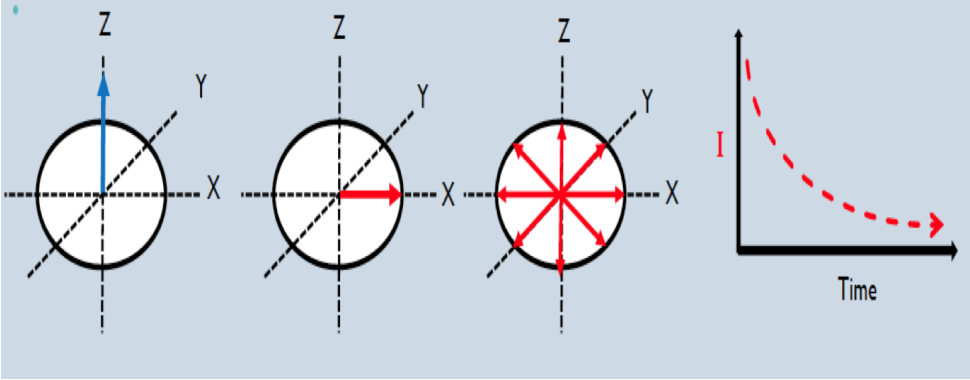


Figure 3.15: T2 Relaxation Following RF Application

Although T_2 decay can be achieved with **gradient echo** method, **spin echo** remains an ideal choice for T_2 decay especially in imaging (Elster and Burdette, 2001).

3.7 Spin Echo(SE) Method

The most basic method for recovering signal is the spin echo method. The simplest experiment is the application of a 180° or π-pulse. Following a period, τ, of dephasing, the π-pulse rotates the orientations of the dephasing magnetisation vectors within the transverse plane. Because they then continue to disperse and precess in the same direction, they will begin to rephase, and after a further period, τ, the vectors will gain phase. This is called a spin echo (Elster and Burdette, 2001).

3.7.1 Graphical Description of Spin Echo Method

As explained in 3.16. When $\pi/2$ or 90° pulse is applied along the **positive** x axis direction , the spins are flipped from z plane into the x-y plane. Then they begin to disperse, and accumulating extra phase. This accumulation occurs when π or 180° pulse is applied along y axis. This occurs at a time $=\tau$. The spins will flip around **positive** y axis direction and continue to collect extra phase at the same rate until time $= 2\tau$. At which time all spins rephase and return to the **positive** y axis together forming an echo. The SE sequence can be written as

$$\frac{\pi}{2}[+X]-\tau-\pi[Y]-\tau-Acquistion. \tag{3.7}$$

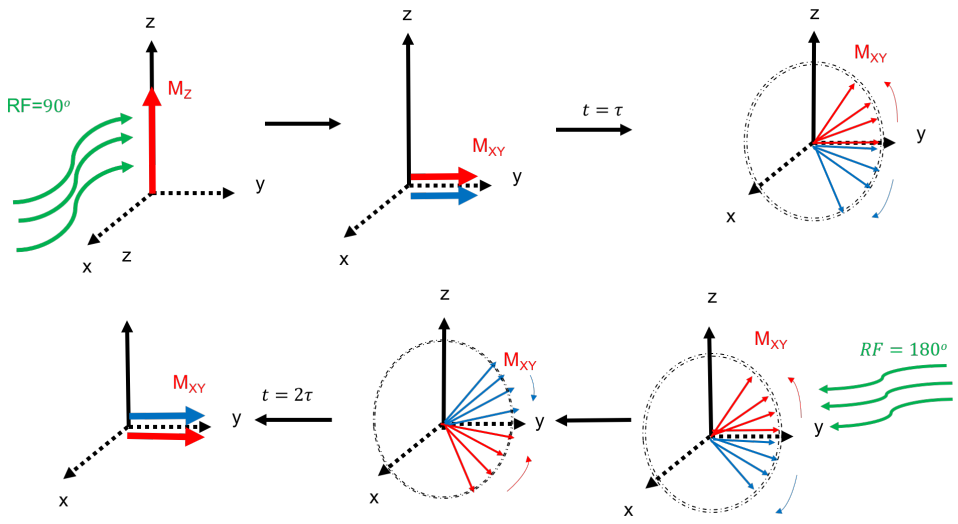


Figure 3.16: Spin Echo $\pi/2$ on x axis While π on y axis

If the π pulse is applied with the same **positive** x axis direction of the $\pi/2$ pulse, the spins will disperse and flipped to **negative** y axis. This is shown clearly in figure 3.17.

The SE pulse sequence notation can be written as

$$\frac{\pi}{2}[X]-\tau-\pi[X]-\tau-Acquistion. \tag{3.8}$$

These two method give a description of what is also known as a phase cycling (Elster and Burdette, 2001).

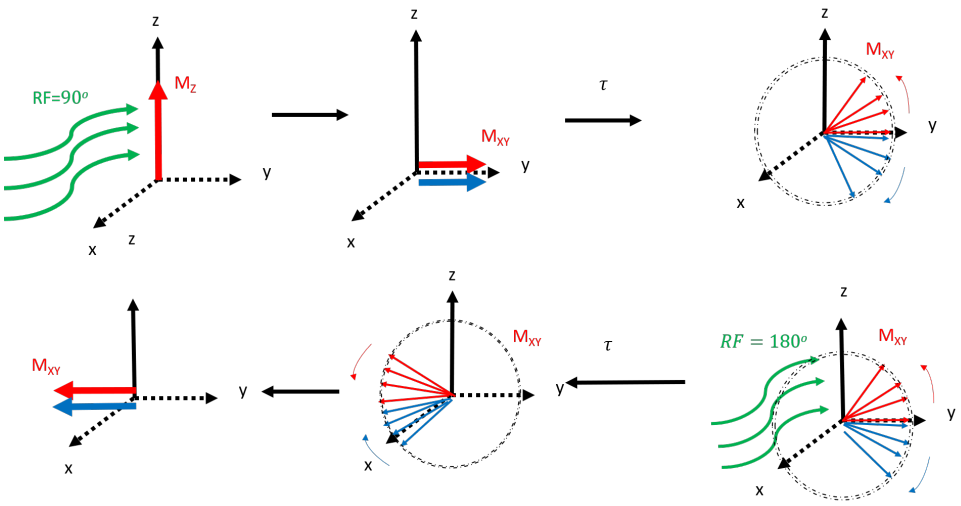


Figure 3.17: Spin Echo $\pi/2$ on X-axis While π on Y-axis

3.7.2 Signal Phase Cycling

Signal Phase Cycling is the phase or the direction of signal when 180° or π-pulse is also used. The sign of signal can be changed by applying the π-pulse along the orthogonal axis. So,the phase of π -pulse can be changed from ± x to ± y axis. Reversing the sign of the π-pulse will not change the sign of the signal. A $\pi[+X]and\pi[-X]$ will produce the same signal direction (Keeler, 2011).

Table 3.11shows all possible signal phase cycling using $\pi/2$ or π pulse over the orthognal-axis

Table 3.1: Signal Phased Cycle Generated by Combination of $\pi/2$ and π Pulses

$\pi/2$ Pulse Phase	π Pulse Phase	Signal Phase
+X	+X or -X	-Y
	+Y or -Y	+Y
-X	+X or -X	+Y
	+Y or -Y	-Y
+Y	+X or -X	-X
	+Y or -Y	+X
-Y	+X or -X	+X
	+Y or -Y	-X

3.7.3 Pulse Criteria

All pulses require a time called **pulse width** and a power called **amplitude**. For example if a $\pi/2$ or π pulse is applied for time (τ) and with power (P). The required pulse could be achieved either by changing the amplitude in decibel (dB) or by (τ) in microseconds (μs). However, the two method are not equivalent. (Keeler, 2011).

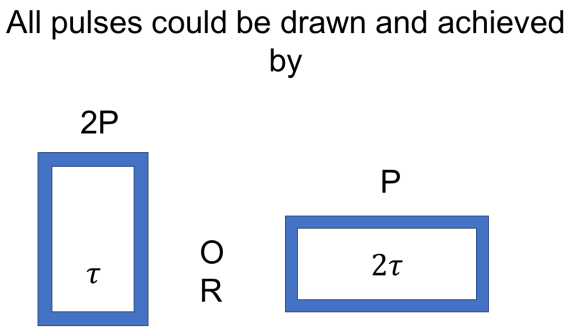


Figure 3.18: Sketch of Two Alternative of Pulse

The spectrometer usually provides us with a way of altering the RF power level and hence the strength of the B1 field. To set B1 field to a specific level, adding an attenuator between the RF source and the amplifier is required. The attenuation is normally expressed in decibels. If the input power is P_{in} and the output power is P_{out} the attenuation in dB is

$$10 \times \log_{10} \frac{P_{\text{out}}}{P_{\text{in}}}$$

Usually the attenuator is under computer control and its value can be set in dB. This is very helpful to us as we can determine the attenuation needed for different B1 field strengths. Suppose that with a certain setting of the attenuator we have determined the B1 field strength to be $\omega^1_{init}\ /2\pi$. However, if we want the field strength to be $\omega^1_{new}/2\pi$. The ratio of the powers needed to achieve these two field strengths

$$\text{power ratio } = \left(\frac{\omega_1^{\text{new}}/2\pi}{\omega_1^{\text{init}}/2\pi} \right)^2$$

$$\begin{aligned} \text{power ratio in dB} &= 10 \log_{10} \left(\frac{\omega_1^{\text{new}}/2\pi}{\omega_1^{\text{init}}/2\pi} \right)^2 \\ &= 20 \log_{10} \left(\frac{\omega_1^{\text{new}}/2\pi}{\omega_1^{\text{init}}/2\pi} \right) \end{aligned}$$

As the duration of a pulse of a given flip angle is inversely proportional to $\omega_1/2\pi$ the relationship can be expressed in terms of the initial and new pulse widths, τ_{init} and τ_{new}:

$$\text{power ratio in dB} = 20\log_{10}\left(\frac{\tau_{\text{init}}}{\tau_{\text{new}}}\right)$$

As an example, if we have calibrated the pulse width for a 90° pulse to be 15 µs but the actual wanted pulse was a 90° pulse of 25 µs. The required attenuation would be:

$$\text{power ratio in dB} = 20\log_{10}\left(\frac{15}{25}\right) = -4.4\text{dB}$$

(Keeler, 2011).

3.8 Limitation of Spin Echo (SE)Method

It is important to point out that the signal strength does not recover to its primary level. In reality, it recovers only to the level dictated by the T2 envelope.

Although SE does not reduce the effect of T_2 decay on the signal, The recovery is complete when all the accumulated phases back again to zero. This only observed and occured when t $= 2\tau$. For t $> 2\tau$, the signal decays away again from the T_2 envelope maximum. This decay noticeably drops off after t $= 2\tau$ especially when the magnetic field B_0 is inhomogeneous.

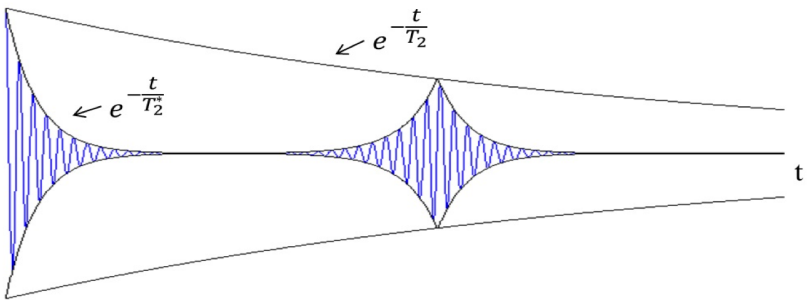


Figure 3.19: Signal strength decay, (Westbrook and Talbot, 2018).

Why does the SE method not reduce the effect of T_2?

The reason that SE method does not reduce the effect of T_2 decay lies in the rapid time fluctuations in the local magnetic field. Inhomogeneities in the local magnetic field are rapidly fluctuating and do not stay fixed in time after the π-pulse. No refocusing is possible

to eliminate this effect, but the time interval over which data are collected is generally quite short compared with T_2 (Keeler, 2011; Westbrook and Talbot, 2018; Currie et al., 2013).

3.9 Fast Spin Echo or Multiple Spin Echo

Applying $\pi/2$ pulse for a time $=\tau$ will dephase the magnetisation. After applying the first π pulse at time$=2\tau$, the magnetisation will rephase. However, the magnetisation will dephase again as it did in the beginning when t$=\tau$. At this time, a second π pulse is applied that will rephase and refocus the magnetisation again, but they will dephase again because of the field inhomogeneities and the T_2^*. A π pulse can be repeated over and over again as an echo train length (ETL), but the echo generated in each application will be smaller to the previous one due to non-recoverable dephasing of T_2 decay. Figure 3.20 shows this multi-spin echo method (Keeler, 2011; Westbrook and Talbot, 2018; Currie et al., 2013).

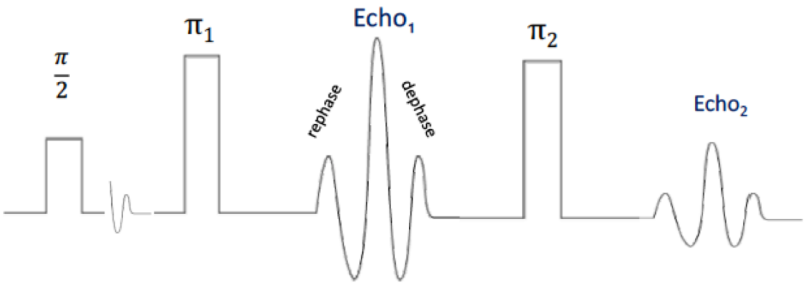


Figure 3.20: Sketch of Double Spin Echo Pulse Sequence

3.10 Diffusion

The diffusion generates irreversible T_2 spin-spin decay. This becomes particularly important if long τ is used to produce a strong T_2 contrast. The diffusion for a given molecule is actually a change of molecule position.

Although the SE sequence can reverse the dephasing caused by magnetic field variation experienced from molecular shifting, dephasing due to the change in position of a given molecule caused by diffusion needs another type of sequence modification

There are two methods to modify the sequence to eliminate or suppress the diffusion effect:

- The Carr-Purcell Mechanism.
- The Meiboom-Gill Improvement.

The general concept is to use a series of (π) pulses which cause spin flips to prevent the phase accumulation from growth for a given spin random walk. The time (τ) is separated into (n) shorter time periods (τ_D).(Keeler, 2011; Meiboom and Gill, 1958; Carr and Purcell, 1954)

3.10.1 The Carr-Purcell Mechanism

In this method a train of (π) pulses are applied along x-axis. The sequence begins with a ($\pi/2$)-pulse, at t = 0, followed by the first π-pulse after a time (τ_D), which is (τ/n). Then a train of π pulses are applied at intervals of ($2\tau_D$), until ($n\pi$) pulses have been applied. The loss of signal due to diffusion depends on (τ_D), while the loss due to (T_2) depends on the total time (2τ) = 2 $n\tau_D$.

$$\frac{\pi}{2}[X]-\tau_D-\pi[X]-2\tau_D-\pi[X]-2\tau_D-\pi[X]-2\tau_D.....etc, Acquistion. \tag{3.9}$$

Basically each π-pulse reverses in turn the sign of the previous phase accumulation.(Carr and Purcell, 1954)

3.10.2 The Meiboom-Gill Improvement

Although Carr-Purcell mechanism could be used to eliminate the effect of self molecular diffusion, it causes another problem due to large number of π pulses. Because each π pulse will depart from the precise 180° spin flip, this will generate a reduced transverse magnetisation for the next upcoming π pulse.

The solution proposed by Meiboom and Gill is to change the phase of the π pulse by 90°. So, instead applying the π pulses along the x-axis, a train of π pulses are applied along the y-axis. The previous method used the x-axis pulses which caused the transverse magnetisation to flip around the same axis by sequential pulses. Therefore, any error in the rotation due to an incorrectly set π pulse, will build up with each following echo. This in turn causes errors in the measurement and a loss of echo signal intensity.

Applying a π pulse along the y-axis refocusses the magnetisation back along the +y-axis, rather than flipping around the x-axis to -y-axis. Any error in the π pulse rotation in the first refocussing pulse is compensated for in the next, and so all the even numbered echoes successfully achieve full intensity (Meiboom and Gill, 1958).

$$\frac{\pi}{2}[X]-\tau D-\pi[Y]-2\tau D-\pi[Y]-2\tau D-\pi[Y]-2\tau D.....etc, Acquistion. \quad (3.10)$$

Figure 3.21 shows The Carr Purcel Meiboom Gill (CPMG) sequence.

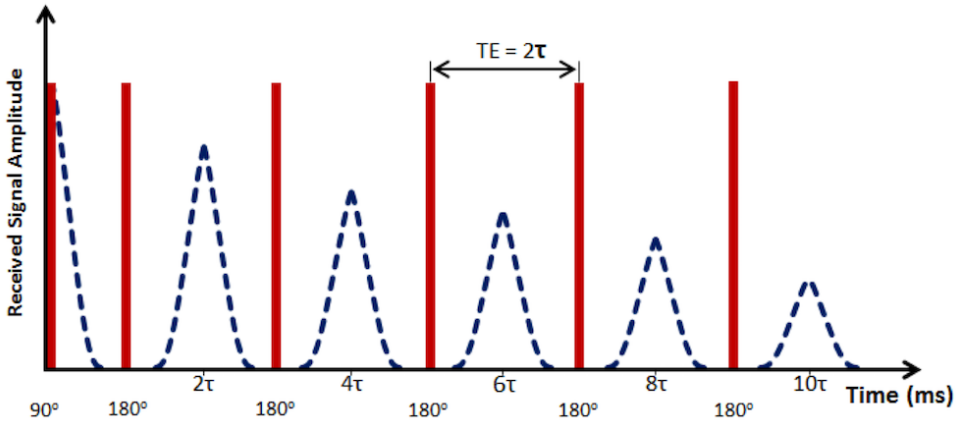


Figure 3.21: Sketch Diagram of CPMG sequence

CHAPTER 4

PUMP CELL PREPARATION

4.1 Construction

Pump cells used were made from borosilicate glass (Dimensions: length = 120 mm, inner diameter = 28 mm, volume ≈ 65 cm^3), and were built and assembled by (Clive Dixon) Nottingham University glass blower. Two valves had glass connection pieces attached and where added to the top of tube. Optically transparent windows were then attached to the end of each tube. The capacity of each is ≈75 ml. Figure 4.1 shows fabricated and constructed pump cell.

4.2 Pump Cell Cleaning

Any used cell, which may contain a residual amount of rubidium droplet or rubidium hydroxide, may require a good cleaning before it's used again for repeated experiment. Figure 4.2 shows the coated pump cell. This cleaning process includes the inlet and outlet entry points of the pump cell. By keeping the cell pressurized with an inert gas, the cell can be transported to a fume hood without igniting the remaining rubidium. By using proper protective equipment, pipette, cotton pads, 10 ml of pure Isopropanol, and a mixture of 10 ml Isopropanol plus 10 ml of water, the pump cell can be cleaned under continuous nitrogen



Figure 4.1: The Shape of fabricated and clean Pump Cell.

flow in a custom made container box. A nitrogen tube is connected to one of the entry points. The tube is flushed with nitrogen 5 times and emptied each time. One of the emptied pump cell taps is opened slightly to allow the nitrogen to flow inside the pump cell for a few seconds. The other tap of the emptied pump cell is completely removed; and a sound of flushing will be heard. Then, pure Isopropanol is poured into the cell. The rubidium oxide layer attached to the pump cell glass is dissolved and isolated from the cell surface. The nitrogen box where the pump cell exists is shaken properly. The mixture is pipetted into the pump cell and the box is shaken vigorously. The first tap is opened completely and the process is repeated until all remaining Rb is completely removed. Once all Rb is removed, the pump cell is rinsed with distilled water. Finally, the pump cell is rinsed with acetone and left to dry (Witte et al., 2012).

4.3 Rubidium Filling

Before Rb is filled into the pump cell, first a clean pump cell is placed in a vacuum oven within glove box chamber overnight (M200 ECO, M.BRAUN Inertgas-System GmbH, Germany) at temperature $\geq$ 100 C°. The vacuum oven chamber is first evacuated (-100 kPa or -1 Bar) and then refilled thoroughly with an atmosphere of N_2. This process was repeated four times to ensure that any H_2O and O_2 contamination was purged from the chamber and pump cell



Figure 4.2: Used pump Cell Coated with Oxidised Rubidium

before transferring the pump cell into the inner chamber of the glove box. The pump cell was then rapidly transferred into the second chamber of the glove box with 100% N_2 inert gas atmospheric environment. Figure 4.3 shows the glove box used.



Figure 4.3: Glove box inner chamber & oven vacuum outer chamber.

Within the inner chamber, a single ampoule of solid Rb is placed on a holder. After heating the ampoule from one side with a heat gun (Tesco, Cheshunt, UK)), the rubidium will become liquefied. While The Rb is falling down to the bottom of the ampoule, it is advisable to leave it for a quite time to return to its solid form again. The filling port of the pumping cell is opened; a heat gun again heats up the Rb ampoule until it became in liquefied form. A pipette is used to suck $\approx$ 1 gram of liquid Rb. The height that the Rb reached on the pipette was measured ($\approx$83 *mm* from the tip of the pipette) and this later on was considered the target height for all subsequent fillings. The pipette is used again to

release Rb into the pumping cell through the filling port. The filling port of the pumping cell is sealed meanwhile the pressure in the glove box is increased by adding a higher pressure of N_2. By doing this, the pressure in the two chambers is maintained equalized. The cell is taken out of the inner chamber to the oven vacuum chamber. Finally, the door between two chambers is sealed and the exit door is opened to carry the pump cell to the next stage for pump cell priming (Witte et al., 2012).

4.4 Pump Cell Priming



Figure 4.4: pump Cell after Priming Process

In the next stage of the preparation process, the spin-exchange optical pumping (SEOP) cell was transferred out of the glove box and evacuated. The pump cell is attached into a lab clamp holder that allows the angulations of the holder, which in turn allow the angulations of pump cell during the set up or "priming" process. The pump cell is connected to a vacuum pump which evacuates the N_2 gas from the pump cell. Therefore, this evacuation allows a high diffusion of Rb around the pump cell. The same tube is used to flush N_2 through the Teflon pipes as this will make sure the pipe is free from any other impurities especially O_2. Moreover, for safety considerations, the standard safety protocol of Sir Peter Magnetic Imaging Centre (SPMIC), states that a shield is placed between the pump cell and the user.

Thus, from behind the shield a heat gun (Steinel, Herzebrock-Clarholz, Germany) of 200° to 310° is placed below the pump cell to heat up lower surface of the pump cell. Meanwhile, the Rb inside the pump cell will start to liquefy creating a line. During this time, the user starts to angle the pump cell using knobs on the pump cell holder. The created Rb line is angulated to spread all over the lower surface of the pump cell. While the heat gun is still active in the lower surface, the upper surface of the pump cell is colder than the lower surface. The liquefied Rb is vaporized and later condensed on the cell wall and surface. By closing the vacuum line, cooling it down for 10-15 minutes and heating it up one more time, the condensed Rb is noticeably coated on the inner surface and two side (window) of the pump cell. Thus, the pump cell windows are then exposed to the heat gun of 325° to remove the condensed Rb from it. During the previous process, the user may notice a bluish colour in the pump cell; this is a sign of very clean pump cell. In addition, an unwanted sign by the user at beginning of the process may be seen in figure 4.2. This could be an orange colour line around the Rb, which means it is contaminated by Rb reaction to N_2 or CO_2 or H_2O. This is called of Rb oxidization. Once this process is finished, the cell is covered with condensed Rb which has a silver colour which in turn is transferred to the polariser where further techniques will take place (Meersmann and Brunner, 2015). Figure 4.4 shows the final appearance of pump cell before taken to polariser.

4.5 Pump Cell Loading

The primed pump cell is placed inside the pump cell oven holder that is located within the Helmholtz coil, which produces a low magnetic field. The gas mixture usually contains one of the noble gas isotopes and nitrogen gas (Goodson, 2002). This is shown in figure 4.5

The linearly polarized laser beam passes through a $\lambda/4$ plate to become circularly polarized ($\sigma+$) and then passes through a telescope optic which extend the beam to about 2.5 cm diameter before it hits the pump cell. Figure 4.6 shows the production of circularly polarized light . Since the Rb inside the pump cell is now heated by laser irradiation and through heat-gun, usually at (110 $C°$-160 $C°$) or 383-433 K in the ^{129}Xe case that generates sufficient Rb vapour for OP (Meersmann and Brunner, 2015).

The temperature is controlled by thermocouples that are located externally near the inlet

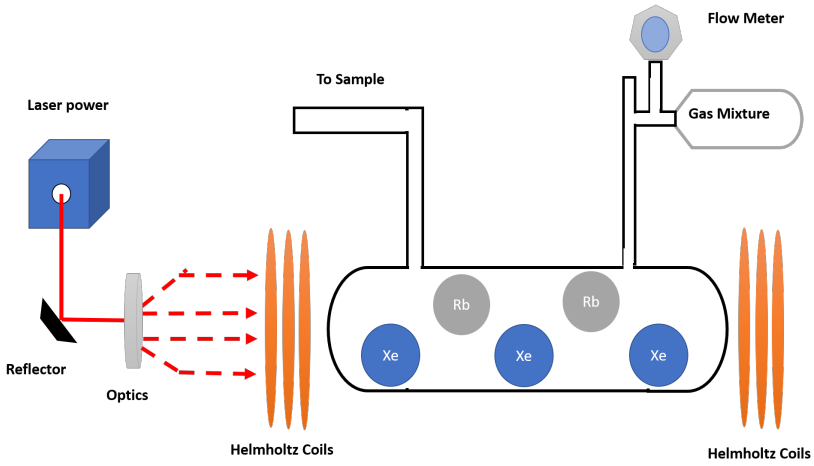


Figure 4.5: pump Cell within Helmholtz Coil

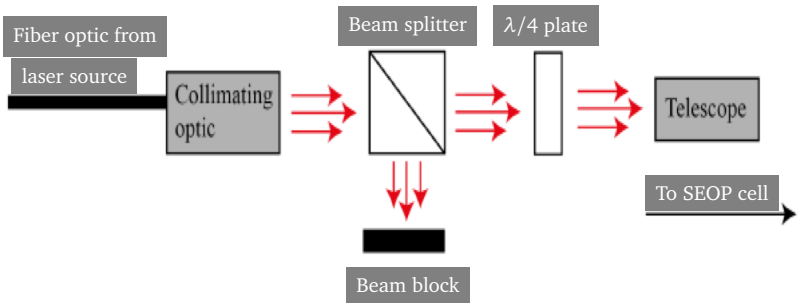


Figure 4.6: Achieving Circularly Polarized Light by $\lambda/4$ plate, (Meersmann and Brunner, 2015).

and outlet of the pump cell. The pump cell is placed between Helmholtz coil pair, which produces a low external magnetic field of approximately 100-150 Gauss (G). This external magnetic field B_0 is aligned with the laser beam and the Rb nuclear spins will align along the same axis.

The pump cell is ready to the next stage of hyperpolarisation of Spin Exchange Optical Pumping (SEOP) which will be discussed in detail within a later chapter.

CHAPTER 5

HYPERPOLARISATION

During the past two decades a new technology using hyperpolarised (HP) noble gases has emerged that overcomes many of the drawbacks a rising from conventional MRI and that enables useful in vivo pulmonary MRI. While magnetic resonance imaging MRI relies on the proton concentration in the subjects tissue to provide an NMR signal. Breathable gases from air remain, notoriously difficult to scan in areas such as lungs and bilayer lipids. The new hyperpolarised technology enables lung structural and lung functional MRI.

HP noble gases are produced through spin exchange optical pumping (SEOP) and are typically inhaled by subjects for the pulmonary MRI scans. ^{3}He and ^{129}Xe both spin I $= 1/2$ are used for pulmonary HP noble gas MRI). Since ^{3}He crisis arises, the academic and researchers were looking for an alternative to HP ^{3}He. Protocols with HP ^{129}Xe have been developed to investigate the lung parenchyma. HP krypton-83 ^{83}Kr I $= 9/2$ is being developed in Nottingham University.

5.1 Classical Theory of MRI Physics

5.1.1 Composition of Nuclei

All atomic nuclei are composed of protons and neutrons. The atomic nucleus is characterized by:

1. Atomic number (Z), defined as charge number; this represents how many protons in the nucleus.

2. Neutron number (N), the number of neutrons in the nucleus.

3. Mass number (A), representing how many nucleons (neutrons + protons) in the nucleus.

The symbol used to define these above numbers is X_Z^A, which is shown in figure 5.1. Neutron number can be calculated by subtracting the mass number (A) from the atomic number (Z) by using the equation:

$$[N = A - Z] \tag{5.1}$$

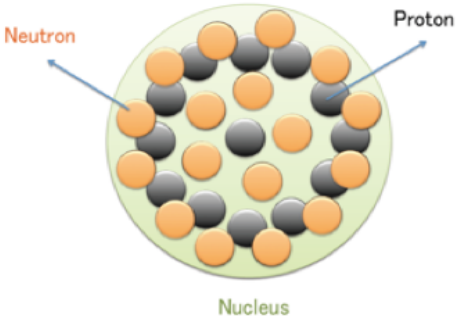


Figure 5.1: Nuclei Composition, (Cherry et al., 2012)

5.1.2 Isotopes

Nuclei that contain the same number of protons but a different number of neutrons are referred to as isotopes. The isotopes of a specific element has the same charge number, but different neutron and mass number. The isotopes natural abundances vary greatly from one to another. Also, not all isotopes give rise to NMR signal. For example Krypton, Kr has different isotopes (^{70}Kr,^{83}Kr,^{101}Kr). Xenon, Xe also has different isotopes (^{126}Xe,^{129}Xe,^{131}Xe) (Cherry et al., 2012).

5.1.3 Nuclear Spin

Each proton and neutron has an inherent angular momentum spin ($= \frac{1}{2}$) that contributes to the total angular momentum of the nucleus or the total nuclear spin. The nuclear spin is represented by (I), which is proportional to the angular momentum. The angular momentum (S) is given by the equation:

$$S = \frac{h(I+1)}{2\pi} \tag{5.2}$$

Where S is angular momentum, h is Planck's Constant and I is nuclear spin. When $I = 0$ for any nuclei, then it cannot be used naturally in Magnetic Resonance Imaging (MRI) experiments, for example we cannot use the oxygen ${}^{16}_{8}O$ nuclei in the lung to image the lung tissues (Mark Brown, 2010). The specific nuclear spin of an isotope can be zero, half integer or integer values. Hydrogen nuclei (i.e. protons) have spin $I = \frac{1}{2}$ and the energy eigenstates are split by Zeeman effect into two levels, $m = -\frac{1}{2}$ and $m = \frac{1}{2}$(up and down), respectively. The two split levels are populated according to Boltzmann distribution which are shown in figure 5.2. Some noble gases such as (Kr) and (Xe) isotopes have spin $I = 0$ and cannot be used in MRI. ${}^{130}Xe$ and ${}^{80}Kr$ are two examples of isotopes that cannot be used in MRI imaging. In the noble gas family, there are five isotopes that are stable and spin-active ($I > 0$). These are listed in Table5.1, (Basdevant et al., 2005).

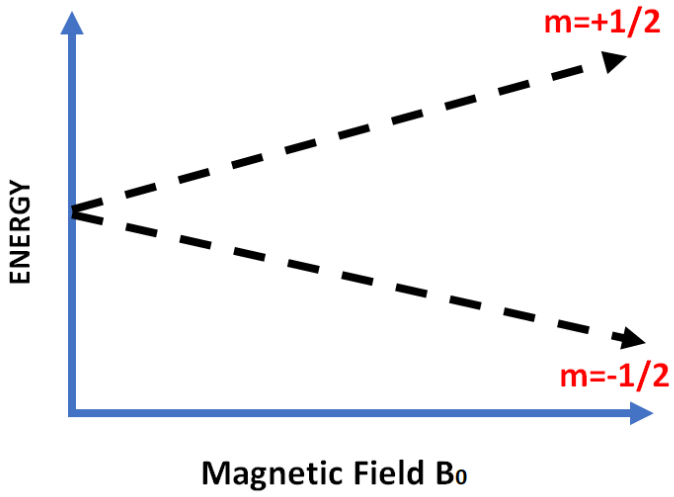


Figure 5.2: Zeeman Splitting, (Weibel, 2009)

Table 5.1: NMR Active noble Gases, (Mark Brown, 2010)

NMR Noble Gas				
Isotope	**Spin**	**Gyromagnetic ratio** $\gamma(10-7rad/Ts)$	**Frequency ratio compared to protons** $\gamma/_{proton}\gamma$	**Quadrupole moment** $(10^{28}m^2)$
^3He	$\frac{1}{2}$	-20.38	0.762	
^{21}Ne	$\frac{3}{2}$	-2.11	0.079	0.09
^{83}Kr	$\frac{9}{2}$	-1.03	0.039	0.26
^{129}Xe	$\frac{1}{2}$	-7.44	0.278	-
^{131}Xe	$\frac{3}{2}$	2.21	0.083	0.12

5.1.4 Hydrogen Nuclei in MRI World

Hydrogen, H is the most commonly used isotope for biomedical MRI applications due the high hydrogen contents in the body, its almost 100% natural abundance and its high gyromagnetic ratio. The H nucleus has a single proton and hence a spin $I = \frac{1}{2}$. The human body is composed of organs, which contain tissues and these tissues are made up of water and fat and therefore have hydrogen in them.

It is easy to understand the quantum physics of MRI when using hydrogen nuclei. Because the H nucleus has a spin of one half, which makes it easy and more accessible to deal with, compared to nuclei with a higher spin systems. This system seems to end up with two different orientations as consequence of Zeeman interaction. One of the orientation is up($I_\uparrow$) and the second is down($I_\downarrow$) which has a higher energy level than the previous one, as can be seen on figure5.2.

The energy of each orientation is given by equation:

$$E_I = \gamma \hbar m_I B_0 \tag{5.3}$$

where E is the energy of each orientation. γ is the gyromagnetic ratio of the specific nucleus, $\hbar$ is [Planck's constant/ 2π], m_i is magnetic quantum number m that can only change by increments of one; it encompasses a range of values between $I_\uparrow$ and $I_\downarrow$, and B_0 is the external magnetic field. Due to the existing magnetic field the energy difference for H nucleus is given by:

$$\triangle E = \gamma \hbar B_0 \tag{5.4}$$

In MRI, the frequency, which is the number of rotation per second, is related to the absorbed energy of nuclei that is called angular frequency which is given by

$$w_0 = 2\pi f \tag{5.5}$$

where w_0 is angular frequency or angular speed and f is the ordinary frequency. Larmor frequency is related to the energy difference between the two ($I_\uparrow$ and $I_\downarrow$) orientations. Therefore, we can express Larmor frequency as:

$$w = \gamma B_0 \tag{5.6}$$

where w is the Larmor frequency. The Boltzmann equation describes the ratio of protons in the respective energy state which is given by:

$$N_I = N_0 e^{-E_I/\kappa T} \tag{5.7}$$

Where: N_I is the population of energy level I, N_0 is the number of nuclei, E_I is the energy level I, relative to energy level 0, κ is Boltzmann's constant= $1.3805 \times 10^{-23} JK^{-1}$, T is the temperature in Kelvin (K). The difference between the populations of higher energy state (N↑) the population of lower energy state (N↓) is given by:

$$\triangle N = N\left[\frac{1}{1+e^{-\hbar w_0/\kappa T}} - \frac{1}{1+e^{\hbar w_0/\kappa T}}\right] \tag{5.8}$$

Applying the magnetic field B_0 on the orientations' axis z, y, x will determine the effect on magnetic moments on each axis. Applying B_0 on z-axis, will not affect the magnetic moment on x or y-axis (Keeler, 2011). Thus, equilibrium magnetization of z-axis in this case is given by

$$M_z = \frac{N\gamma\hbar}{2V}\left[\frac{1-e^{-\hbar w_0/\kappa T}}{1+e^{-\hbar w_0/\kappa T}}\right] \tag{5.9}$$

Where: V is the sample volume that contains N nuclei.

at room temperature the equation 5.9 is reduced to

$$M_z = \frac{N\gamma^2\hbar^2}{V\kappa T}B_0 \tag{5.10}$$

5.1.5 Hydrogen Nuclei is not used in MRI Pulmonary Application

According to Wielpütz and Kauczor (2012), MRI imaging is one of the strongest techniques commonly applied to daily case diagnosis. This could spare the patients from ionizing radiation; however, the basic methodology of MRI has its limitations. These drawbacks arise from lack sensitivity of in vivo MRI in particularly of lungs that are difficult to image, due to the low tissue density and the low number of MR active nuclei in that organ. Lung airways are filled with oxygen that can not be used in MR imaging as previously mentioned. Furthermore, nitrogen gas, N_2 is MR active but the gas density is about 1000 times lower than that of condensed matter such as body tissue. Lung parenchyma may not be clearly assessed through in vivo MRI due to several factors: first of all, decreased tissue density means also low hydrogen isotope count. Second, the magnetic susceptibility at the tissue-tissue and in particular at tissue- gas interface causes magnetic field inhomogeneity due to the susceptibility difference between regions inside the lung. This leads to short transverse relaxation, T_2. Thirdly, respiratory and cardiac motion artefact is arising during the scanning. Also, blood vessel pulsation from major arteries such as pulmonary, aortic arch, ascending and descending aorta, which lies inside the respiratory cavity cause motion artefacts (Wielpütz and Kauczor, 2012; Gould and Isaacson, 1993; Glover and Pauly, 1992).

On the other hand, Nuclear Medicine (NM), Computed Tomography (CT), Positron Emission Tomography (PET) and Single Photon Emission Computed Tomography (SPECT) imaging techniques could be a solution to have a visible finding of lung tissue disease and abnormality (Wielpütz and Kauczor, 2012). The drawbacks of these imaging modalities are the involvement of exposing the subject into Ionizing Radiation either from direct sources of radiation or injecting radioactive materials into subject (Lutterbey et al., 2005; Brenner and Hall, 2007).

Pathologically, clinical MRI was implemented before the development of hyperpolarised gases. They were usually performed at 1.5 Tesla scanners using parallel imaging technique. 3

T scanners are still preferred due to their better Signal to Noise Ratio (SNR). Figure 5.3 shows basic non-contrast techniques which are based on gradient echo (GRE) $T_1W.I$, fast spin echo (FSE) $T_2W.I$ or Short-TI Inversion Recovery (STIR) sequences with some modification on sequence parameters to overcome the problems that arises from artefact. These sequences were useful to detect abnormalities including vessels tumour and masses when iodinated contrast agent were contraindicated for some patients (Wielpütz and Kauczor, 2012).

In in vivo MRI studies, the hydrogen (proton) within the tissue molecules are excited to generate signal. Unfortunately, the lungs have a very low tissue-to-volume ratio leading to a low proton density, producing a very weak MR signal intensity. Lung tissues that are not rich in protons will produce weak signals and have a dark appearance. The signal strength contributes to the resolution of the acquired image and therefore, weak signal intensity is undesirable. Figure 5.4 shows the difference in signal intensity between two images Proton Density (PD) and hyperpolarised (HP) helium ^3He taken from the same patient (Gould and Isaacson, 1993).

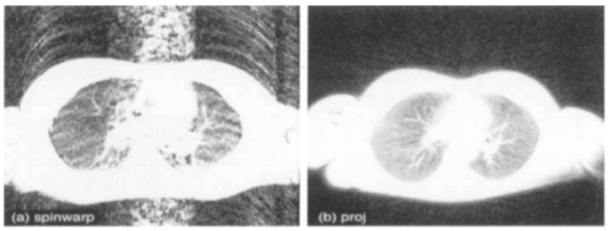


Figure 5.3: MRI Lung Images: (a) Conventional T_1 Weighted Image multi-slice spin (b) Axial l T_1 Weighted Image with multi-slice projection reconstruction(motion artefact has disappeared),(Wielpütz and Kauczor, 2012)

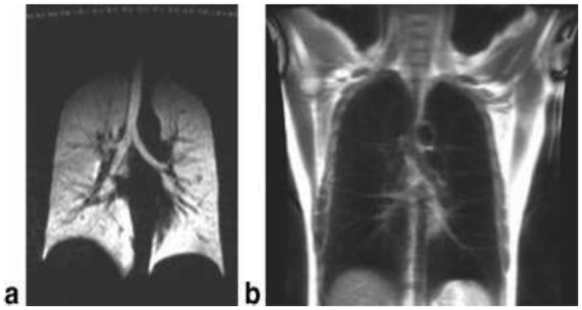


Figure 5.4: MRI Lung Images: (a) Hyperpolarised ^3He of human lung (b) Proton Density (PD) image of the same lung, (Gould and Isaacson, 1993)

5.2 Historical Background in Hyperpolarised Noble Gases uses in Pulmonary Imaging

Albert et al. (1994) imaged an excised mouse lung using with hyperpolarised ^{129}Xe. In this work, they have used (1.2×10^{19} atoms cm^3) of ^{129}Xe gas that enriched to two third of the percentage of 70%. The ^{129}Xe concentration was much smaller than the concentration of protons. He used approximately 20 mM of ^{129}Xe which is considered quarter the concentration of protons. Figure 5.5 shows the first lung image that was recorded in MRI with HP ^{129}Xe.

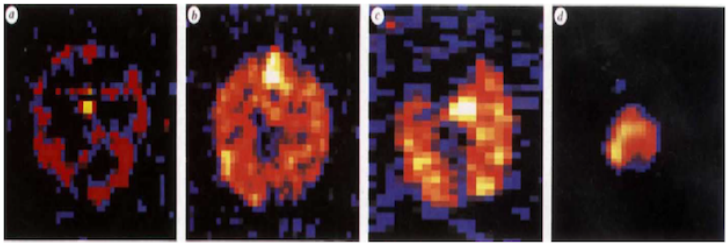


Figure 5.5: MRI of rat Lung Images using Hyperpolarised ^{129}Xe, (Albert et al., 1994)

Middleton et al. (1995) and his group performed a guinea pig lung and middle chest imaging. They had used 3.5 to 8 atm of ^3He with few milligram of Rubidium (Rb) for Hyperpolarizing ^3He using spin exchange optical pumping (SEOP). Figure 5.6 shows a 2-dimension of Gradient Recalled Acquisition in Steady State (GRASS) sequence image was obtained from an animal by using inhaled ^3He gas and 6° flip angle.

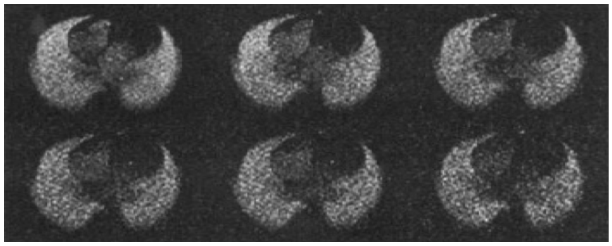


Figure 5.6: MRI Pig Lung Imagesusing GRASS Sequence, (Middleton et al., 1995)

A few years later, the first human trial in vivo of Hyperpolarised noble gas was performed by HP ^{129}Xe. However, most clinical in vivo imaging were performed in human subject using HP ^3He as contrast agent rather than other noble gases. The reason for this is the higher signal intensity arises from ^3He because it has larger gyromagnetic ratio than ^{129}Xe. Additionally, in terms of human safety the only risk of ^3He MR imaging is a low O_2 concentration while

inhaling the anoxic ^3He–N_2 mixture. To avoid serious and long duration arterial oxygen desaturation, breath-hold times with the gas mixture are restricted to 10–15 sec. The blood oxygen saturation is continuously monitored using an optical finger clip sensor.

5.3 ^3He at Market and in Research Field

Nowadays, price of ^3He has been rocketed to approximately 500 $per Litre caused by a supply crisis. In response, some actions have taken place by US congressmen that reduce the depletion of the existing ^3He reserve. These actions were taken because of ^3He preserve is shortened due to the high demand on it by border security and for neutron detection usage.

In 2009, shortage of ^3He has come to surface during US congressional discussion. Currently, U.S. nuclear weapons program produce approximately 8,000 litres of new ^3He per year and only 2000 litres are available for US clinical use. Importantly, ^{129}Xe has been revealed as an alternative modality that may replace ^3He (Lilburn et al., 2013).

5.4 Noble Gases and Alkali Metal Properties

5.4.1 Rubidium [Rb]

Rb is one of the most commonly used alkali metal in spin exchange optical pumping (SEOP) because high laser power is available to pump the relevant D_1 transition. One gram of Rb at considerable controlled temperature creates a high level of Rb densities (Six et al., 2012). The Rb density as a function of temperature is given by

$$[Rb^T] = \frac{10^{32.18} - \frac{\text{gas density}}{T}}{T} \tag{5.11}$$

The gas density is measured using the amagat, where 1 Amagat $= 2.6868 \times 10^{-3} m^{-3}$. The Amagat represent the gas density at standard temperature and pressure (STP) of 273.15 K and 101.325 kPa. Thus, at STP the rubidium density would be $[Rb]^{273} = 8.7 \times 10^{14} m^{-3}$. The only two Rb isotopes used in hyperpolarisation are ^{85}Rb and ^{87}Rb, with natural abundance of 72.2% and 27.8%, respectively (Cleveland et al., 2007; Six et al., 2012).

5.4.2 Xenon ^{129}Xe

Xenon is a colourless, odourless gas which has a large electron shell, which is shaped by the surrounding environment. This usually generates a localised dipole within atoms. The large electron shielding generated, produces a wide range of chemical shifts between 79 to 212 ppm. It has a boiling point of $-108.13°$ (-162.5F) at ambient pressure.^{129}Xe is found in the earth's atmosphere at a concentration of about 0.1 ppm. The natural abundance isotope distribution is 26.4% for ^{129}Xe and 21.2% for ^{131}Xe. ^{129}Xe have a spin of I $= 1/2$ while ^{131}Xe have a spin of I $= 3/2$ and both are considered as renewable resource. One litre of ^{129}Xe costs about 10 to 12 US dollar, which make it more affordable than ^{3}He. Like ^{3}He, ^{129}Xe has nuclear spin of I $= 1/2$. Although ^{129}Xe has a lower gyromagnetic ratio than ^{3}He with corresponding lower magnetic moment and lower magnetic resonance frequency, the ^{129}Xe has high hyperpolarisation levels in excess of 50%, making this isotope suitable for pulmonary MRI.

The following characteristics of ^{129}Xe makes it more suitable imaging isotope over ^{3}He :

1. ^{129}Xe is like any other noble gas and could be found in gaseous form at normal temperature.

2. Chemically ^{129}Xe is considered as inert isotopes like any other noble gas.

3. ^{129}Xe may be obtained from air liquefaction.

4. ^{129}Xe can be readily frozen at liquid nitrogen temperatures.

5. As ^{129}Xe is lipophilic and dissolves in tissue, in particular in fibrotic and fatty tissue.

6. ^{129}Xe has a different MR resonance frequency due to its large chemical shift. This makes dissolved HP ^{129}Xe in Red Blood Cell (RBC) observable for MRI.

7. As ^{129}Xe is non-toxic substance as any other noble gas, although it can act as a mild anaesthetic unlike other noble gases. Due to its anaesthetic properties its concentration should be lower than 35%, which could be considered as disadvantage that can be solved in clinical application.

8. Because ^{129}Xe has a low gyromagnetic γ ratio, and low frequency, T_2^* arising from B_0 inhomogeneity, will be longer than for ^3He. This facilitates MRI experiments at higher field strength.

Scientists found ^{129}Xe properties are allowing it to be used in lung imaging and scanning as an inhaled contrast agent for human subjects (Lilburn et al., 2013; Barskiy et al., 2017; Meersmann and Brunner, 2015).

5.4.3 Krypton ^{83}Kr

Unlike ^{129}Xe and ^3He, which have a nuclear spin of I $= 1/2$ system (spherically symmetric), ^{83}Kr has a nuclear spin of I $= 9/2$ (a non-spherical partition of the nuclear charges), which could also be hyperpolarised by using SEOP method. At the level of atmospheric pressure, ^{83}Kr exhibits long gas-phase T_1 of several hundred seconds. ^{83}Kr have exhibited some important medical effects in animals before the basic biology of how they work has been studied. Despite this relative lack of knowledge of their mode of action, some of the noble gases have even been used successfully in the laboratory.

Moreover, like Xe, it can be separated from Rubidium vapour without severe depolarization. HP ^{83}Kr could provide MRI contrast that is sensitive to the surface of its environment. When surface-^{83}Kr adsorption occurs, a deformed electron cloud and electric field gradient (EFG) formation takes place. As a consequence of the interaction between the EFG and the nuclei quadrupolar moments, ^{83}Kr nuclear spin will depolarize due to the fast quadrupolar relaxation. This sensitivity is caused by its nuclear electric quadrupolar moment leading to interactions that affect the spin lattice relaxation rate when HP ^{83}Kr is directly in contact with surfaces.

In particular, the spin lattice relaxation of ^{83}Kr gives clear data about surface properties including surface-to-volume ratio, hydration, and temperature. In addition, the ^{83}Kr was firstly investigated via NMR using complex system when dissolved in variety of polar and non-polar solvents (Cleveland et al., 2007; Six et al., 2014).

5.5 Optical pumping Concept

The concept of optical pumping is to increase the magnetization through alignment of the nuclear spins. This is achieved through laser pumping techniques (Lilburn et al., 2013; Meersmann and Brunner, 2015). In term of physics, a group of spins with nuclear spin =1/2 nuclei will have a spin polarization P according to:

$$P = \frac{\triangle N}{\sum N} \tag{5.12}$$

the equation is then simplified to be :

$$P = \frac{N\uparrow - N\downarrow}{N\uparrow + N\downarrow} \tag{5.13}$$

Where $N\uparrow$ and $N\downarrow$ is the difference in the population of magnetization of higher and lower energy state: Eigenstate 1/2, Eigenstate -1/2. This was previously explained in section 5.1.3. Figure 5.2 shows the splitting of the two energy states. The $Thermal$ Polarization P and the magnitude of γ has proportional relationship represented in the population magnetization as the magnetisation increases, the thermal polarisation and the magnitude of gyromagnetic ratio is also increase. However, decreasing the magnetisation will decrease the thermal polarisation and the magnitude of gyro magnetic ratio.

Magnetization is an important factor that contributes to NMR signal intensity. This can contribute to MRI image resolution, as higher resolutions are only possible with a high NMR signal-to-noise ratio. The **bulk magnetization** (M_0) as a function of the spin polarization relationship is taken from:

$$M_0 = \frac{1}{2} N_i \gamma h P \tag{5.14}$$

Where N_i is population number of nuclear spin. Recalling the (equation 5.7) in section 5.1.4 in a sample that is at a $thermal$ equilibrium state with a strong external magnetic field and at temperature, the polarization P can be recalculated using the Boltzmann distribution equation as:

$$P = \frac{e^{\frac{-\hbar\gamma B_0}{2kT}} - e^{\frac{\hbar\gamma B_0}{2kT}}}{e^{\frac{-\hbar\gamma B_0}{2kT}} + e^{\frac{\hbar\gamma B_0}{2kT}}} \tag{5.15}$$

By using the approximation $e^{\pm X} \approx 1 \pm X$, this equation is then can be rewritten as:

$$P = \frac{[1 - \frac{-\hbar\gamma B_0}{2kT}] - [1 + \frac{\hbar\gamma B_0}{2kT}]}{[1 - \frac{-\hbar\gamma B_0}{2kT}] + [1 + \frac{\hbar\gamma B_0}{2kT}]} \tag{5.16}$$

Provided the spin system fulfils the high temperature conditions $T \geq \frac{\gamma\hbar B_0}{k}$. For Nuclear Magnetic Resonance (NMR), the high temperature condition is fulfilled at ambient temperature and the equation is then simplified to be:

$$P \approx \frac{\gamma\hbar B_0}{2kT} \tag{5.17}$$

This equation can be combined with with equation (5.14) to give

$$M_0 = \frac{N_i \gamma^2 \hbar^2 B_0}{4kT} \tag{5.18}$$

since equation (5.17) represents the *thermal* equilibrium polarization for spin $[I = 1/2]$, it can be shown that for nuclei of nuclear spin $[I > 1/2]$, the *thermal* equilibrium polarization at high temperatures is given by:

$$P = \frac{\gamma\hbar B_0}{3kT}(I + 1) \tag{5.19}$$

For example, using a superconducting magnet of 9 T field and at ambient temperature (usually 300 Kelvin), the ^{129}Xe and ^{83}Kr polarization is approximately 8.8×10^{-6} and 4.52×10^{-6} respectively (Meersmann and Brunner, 2015).

5.5.1 Temperature Effect

Using the previous equations (5.18), the *thermal* equilibrium polarization P is proportional to the external magnetic field strength. The higher the magnetic field B_0, the higher the polarization P at a given temperature, but there are obvious limits given the available magnetic field strengths. Also, Polarisation P is inversely proportional to the temperature T. Therefore, the lower the T, the more polarization P will be in a sample. However, decreasing the sample temperature is not an option when acquiring the data from human tissues

or organism. Furthermore, very low temperatures with T $\ll$ 1K are required that are difficult to reach. However, a possibility exists using a $non-thermal$ equilibrium state by a method called **Hyperpolarisation** (HP). HP is another way to move the sample from equilibrium state to a (very low spin temperature) non-equilibrium state. Generally, high polarisation demand low temperature that is usually far below 1 K. Most NMR and NMR applications are performable at such low temperature while hyperpolarisation can provide a high polarisation value at high temperature, A hyperpolarised spin system is determined by a very low spin temperature that is at non equilibrium environment (usually at ambient temperature). The low spin temperature is produced in substances that remain at very low temperature for a period of time that is quite enough to reach thermal equilibrium. Rapid heating of the system to a higher temperature may result in a thermal non equilibrium state known as **hyperpolarised** spin state. Paradoxically, this is achieved by increasing the sample temperature for a short period of time. The low spin temperature is then generated through laser pumping (Garcia et al., 2007; Meersmann and Brunner, 2015).

A decreased temperature of spin leads to a high population of the ground state and thus high spin alignment, or a high nuclear magnetization resulting to very high NMR / MRI signal intensity. This state is not stable and will eventually relax back to the $thermal$ equilibrium through longitudinal relaxation governed by a time constant called T_1. Thus, if the longitudinal relaxation is slow enough, the non-equilibrium, high signal intensity state remains for sufficient periods of time to conduct the MR experiments (Krjukov et al., 2005).

There are a number of ways to achieve the hyperpolarisation of noble isotopes but the thesis focuses only on those produced by **Spin Exchange Optical pumping** (**SEOP**) via alkali metal vapour such as Rubidium (Rb) (Walker and Happer, 1997).

The way of reaching hyperpolarisation state could be subdivided into two steps processes. **First step** is where Alkali metal **Optical pumping** (**OP**) and the **second step** is **Spin Exchange** (**SE**), where the alkali metal electron spin polarization is transferred to generate a high nuclear spin polarization for ^3He, ^{129}Xe and ^{83}Kr (Goodson, 2002).

5.6 Optical pumping & Spin Exchange

5.6.1 Optical pumping (OP)

Optical pumping (OP) is achieved by applying a beam of laser light ($\sigma+$) to the pump cell that is subjected to a low magnetic from a Helmholtz coil. The pump cell contains 1 gram of rubidium (Rb) in the lower surface of the cell that is externally heated by air to produce the Rb vapour. Initially, the cell is 'primed' by making the Rb condense on the total surface of the cell with the exception of the entry window.

The atomic Rb vapour has an unpaired S-electron in the outer shell that will be pumped to the p shell using the appropriate laser wave length causing a D_1 transition at 794.7 nm, this wave length requires a 24 W of the power after $\lambda/4$ plate.. Figure 5.7 shows the transition of the OP process.

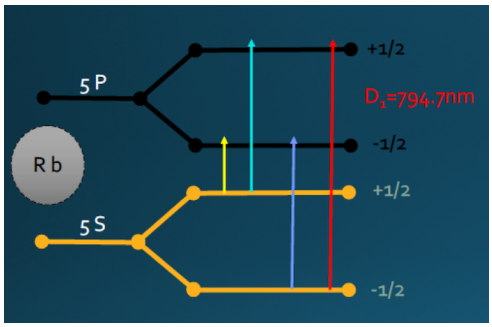


Figure 5.7: The D_1 transition of Optical pumping (OP) Associated with Collision Between Rb Electron and Laser light

In a magnetic field, the 5s and 5p levels each have two sub-levels associated with the electron spin orientations -1/2 and 1/2 respectively. The selection rules dictate that circularly polarized photons ($\sigma+$) pump the Rb electron specifically from -1/2 sub-level of the 5s shell to + 1/2 sub-level from 5p shell ($\triangle$ m $= +1$ for $\sigma+$). Figure 5.8(a) shows the one Zeeman sub-level to polarised in the absence of magnetic field.

However, the electron does not stay in the excited 5P state for long and relaxes back into either $+1/2$ or $-1/2$ sub-level of the 5s state. If it falls back into the -1/2 sub-level, it will be pumped again, however, if it relaxes into $+1/2$ it will remain in this state as it can't be pumped from there by $\sigma+$ photons. Eventually, all electrons end up in the + 1/2 state of 5p level (Meersmann and Brunner, 2015). Figure 5.8(b) shows the effect of magnetic field on the excited electron.

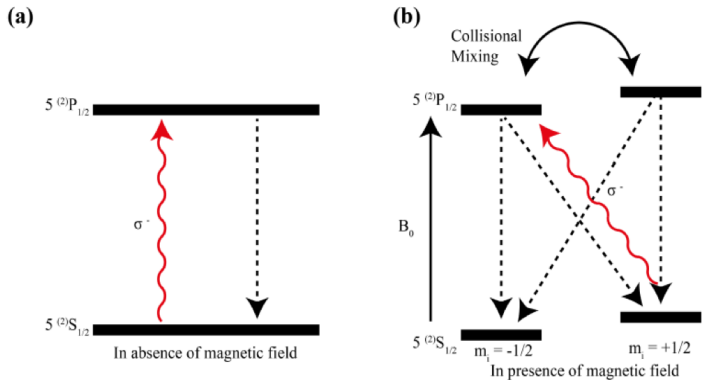


Figure 5.8: The Effect of Magnetic field on Zeeman Sub-level polarisation (a) In The Absence of Magnetic Field (b) In The Presence of Magnetic Field, (Meersmann and Brunner, 2015).

5.6.2 Spin Exchange (SE)

A second part of the process is when gas mixture of noble gas and buffer gas is transferred from storage cylinder via Teflon pipe into the inlet of the pump cell, the noble gas enters+ the pump cell where the spin exchange (SE) will take place between the (electron) of HP alkali metal and (nucleus) of noble gas atoms. Hyperpolarised Rb and un-polarized ^{129}Xe are good example to explain the spin exchange process. When un-polarized ^{129}Xe comes into contact with hyperpolarised Rb through collision, the interaction between the unpaired electron of hyperpolarised Rb and ^{129}Xe gas phase. This interaction is known as "Fermi-Contact hyperfine interaction" takes place. This interaction is responsible for transferring the polarization from Rb atoms to ^{129}Xe gas atoms caused by collisions resulting in a "flip flop" transfer. Figure 5.9 shows the flip flop collision where eventually, the hyperpolarised ^{129}Xe reaches a non-equilibrium state with very high polarization (or low spin temperature) where its magnetization (M) is largely increased. The Gas mixture (discussed further later in this chapter) that is transferred into the pump cell does not only contain ^{129}Xe but also nitrogen (N_2). The nitrogen is added as a buffer gas to remove or quench the fluorescence effect from excited (5p) Rb electrons to allow for relaxation to ground state without the emission of a photon. Since these photons can be 5s level photons, the wrong pumping could be induced (i.e. from the + 1/2 sub-level to the – 1/2 level of the excited state). The hyperpolarised gas spin nuclei will be transferred from the pump cell to reach a sample or to be stored for another usage (Meersmann and Brunner, 2015).

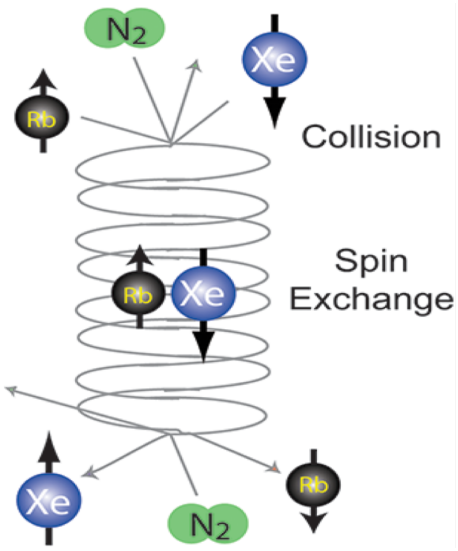


Figure 5.9: Flip-Flop Action of Rb and ^{129}Xe Spin Exchange (SE), (Birchall et al., 2017).

5.7 Polarisation in SEOP

The spin polarization of hyperpolarised system is not governed by a $thermal$ equilibrium from Boltzmann distribution but rather the polarization produced by SEOP. Polarization P can be increased in noble gases using a process of SEOP to be **hyperpolarised**. SEOP can be used to dramatically deplete one of the spin-states. Figure 5.10 shows a representation of this hyperpolarisation with corresponding NMR spectrum. In the thermal sample a 3983 scans were need to reach a spectrum of high signal intensity which require long acquisition and scan time while the spectrum was achieved with one scan when hyperpolarised sample was used.

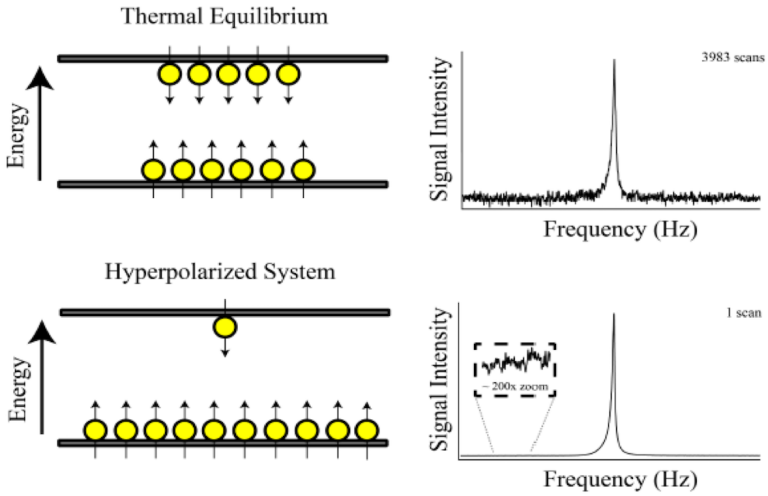


Figure 5.10: Comparison between NMR Signal from $Thermally$ Polarised Spin System and Hyperpolarised Spin System, (Meersmann and Brunner, 2015).

Happer et al. (1984) and colleagues have studied the theoretical impact of the SEOP. They used quantum physics of a simple Hamiltonian to describe the spin relaxation and transfer of ($Rb \rightleftharpoons {}^{129}Xe$) exchange in the SEOP cell as:

$$\vec{H} = A\vec{I}.\vec{S} + \gamma\vec{N}.\vec{S} + \alpha\vec{K}.\vec{S} + \mathscr{G}_S\mu_B\vec{B}.\vec{S} + \mathscr{G}_I\mu_B\vec{B}.\vec{I} + \mathscr{G}_K\mu_B\vec{B}.\vec{K} + \ldots \tag{5.20}$$

The equation above does not consider the buffer gas interaction from N_2. Where A, γ and α are coupling constants $\mathscr{G}_S$, $\mathscr{G}_I$ and $\mathscr{G}_K$ are $\mathscr{G}$-factors. μ_B is the magnetic moment. $\vec{S}$ is the electron spin, $\vec{I}$ is the spin of Rb nucleus, $\vec{N}$ is the rotational angular momentum of the metal, $\vec{K}$ is the spin associated to the noble gas, and $\vec{B}$ is the magnetic field. Spin polarization of the unpaired outer electron of Rb alkali metal as hyperfine interaction is represented by the term $A\vec{I}\vec{S}$, while Zeeman effect that results in energy level splitting during collisions of Rb and ${}^{129}Xe$ are part of a Van Der Waals complex is represented by the term $\gamma\vec{N}.\vec{S}$. The terms containing G factors and magnetic field $\vec{B}$ represent the coupling between spins of the electrons, Rb (alkali metal) nuclei, and the noble gas nuclei and the applied magnetic field. Taking into account that the Helmholtz coil used in SEOP produces a magnetic field of (40-100 G) which is responsible for ordinary Zeeman effect (Happer et al., 1984; Childs et al., 1982). Leaving Fermi contact hyperfine interaction between the noble gas nuclei and electrons of Rb vapour represented by the term $\alpha\vec{K}.\vec{S}$. This term could be simplified by quantum physics as:

$$\alpha\vec{K}.\vec{S} = \frac{\alpha}{2}[K^+S^- + K^-S^+] + AK_zS_z = \hat{H}_{KS} \tag{5.21}$$

Where K^+S^- , K^-S^+ are responsible for transferring the polarization from Rb atom to ${}^{129}Xe$ gas atom caused by "flip flop" interaction in SEOP and α is equivalent to the chances of locating the unpaired Rb electron in the nucleus of noble gas (NG). Combining equation (5.20) and equation(5.21) will determine noble gas polarization. Polarization of the noble gas as a function of time is given by:

$$P_{NG}(t) = \frac{\mathscr{R}_{SE} \times P_{avg}}{\mathscr{R}_{SE} + \mathfrak{R}_{NG}} \times 1 - e^{(-\mathscr{R}_{SE} + \mathfrak{R}_{NG})T} \tag{5.22}$$

Where P_{NG} is polarization of the noble gas, P_{avg} is the average polarization of Rb vapour, and T is the noble gas residence time in the pump cell. $\mathscr{R}_{SE}$ is the spin-exchange (SE) rate

per atom of noble gas; as a function of the SE rate constant of Rb and density of Rb vapour in the pump cell. $\Re_{NG}$ is the relaxation rate of the noble gas in the absence of Rb vapour due to inhomogeneity of magnetic field. The average polarization of Rb is given by:

$$P_{avg}(z) = \frac{\mathscr{R}_{op}(z)}{\mathscr{R}_{op}(z) + \Re_{SD}} \tag{5.23}$$

Where $\mathscr{R}_{op}(z)$ is the Rb optical pumping rate at z-axis along the laser light irradiation, K_A^i is the gas mixture coefficient rate, while M_i is the gas atom number densities and $\sum K_A^i.(M_i) = \Re_{SD}$ is the rate of relaxation due to spin-destruction collisions, or any collision between Rb (alkali metal) atoms which leads to a loss of the spin orientation provided by optical pumping. The polarization equation is then can be rewritten by combining equation(5.22) and equation(5.23) to be as:

$$P_{NG}(t) = \frac{\mathscr{R}_{SE}}{\mathscr{R}_{SE} + \Re_{NG}} \times \frac{\mathscr{R}_{op}}{\mathscr{R}_{op} + \sum K_A^i.(M_i)} \times [1 - e^{(-\mathscr{R}_{SE} + \Re_{NG})T}] \tag{5.24}$$

This equation is then simplified further for SEOP of certain isotopes when K_A^i for $^{129}Xe \approx 5.2 \times 10^{-21} m^3 s^{-1}$ and K_A^i for $^{83}Kr \approx 1.1 \times 10^{-21} m^3 s^{-1}$. The K_A^i of spin destruction between Rb atoms are $8.1 \times 10^{-19} m^3 s^{-1}$ (Wagshul and Chupp, 1994; Bouchiat et al., 1969, 1972). The spin-destruction rates for Rb, Xe, and Kr were recorded at 300 K. Thus total polarization were simplified to be :

$$P_{NG}(t) = \frac{\mathscr{R}_{SE}}{\mathscr{R}_{SE} + \Re_{NG}} \times \frac{\mathscr{R}_{op}}{\mathscr{R}_{op} + \sum K_A^{NG}.(NG)} \times [1 - e^{(-\mathscr{R}_{SE} + \Re_{NG})T}] \tag{5.25}$$

5.8 Gas Mixture

Previous studies(Meersmann and Brunner, 2015; Six et al., 2012; Lilburn et al., 2015) have described that gas mixtures are diluted with fluorescence effect quencher (N_2). If no cryogenic separation is used, it is difficult to precisely compare the recorded signal from SEOP gas to noble gas signal. While cryogenic separation using liquid N_2 may work with other noble gases such as ^{129}Xe. HP ^{83}Kr can not be separated cryogenically, this due to the longitudinal relaxation $T_1 < 10$ sec. A **cryogenic free** technique was used to study the

different noble gas mole fraction behaviour in percentage (%) at various SEOP pressure in (Bar). Gas mixtures were usually prepared prior to SEOP experiments which takes place using a custom built stainless-steel gas mixing system. Gas cylinder for mixture storage were flushed with N_2 five times and evacuated for over twelve hours before use. The typical gas mixture we used were:

1. Research grade ^{129}Xe with 100% purity, and natural abundance of 26.4%, (UN2036, BOC Limited, Surrey, UK)
2. Research grade ^{83}Kr with 99.995% purity, and natural abundance of 11.5%(UN1056, Airgas INC, Radnor, USA)
3. Research grade Compressed N_2 with 99.999% purity, (UN 1066, Air Liquid, Birmingham, UK)

5.9 Polarization & SEOP Pressure

5.9.1 Apparent polarization

An apparent polarization, P_{APP}, is defined as the polarization scaled to the equivalent amount of pure noble gas need to produce the signal intensity and is given by:

$$P_{APP} \approx P.\frac{P_{NG}}{P_T} \tag{5.26}$$

where P_{NG} is the pressure of noble gas, and P_T is the total gas pressure (Six et al., 2012).

5.9.2 Xenon Polarization

The Figure 5.11 also gives a clear information on polarization behaviour as function of SEOP pressure. As the pressure decreases polarization increases regardless of mixture type used. Also, the ↓ SEOP Pressure → the ↑ P of signal from Gas mixture. Moreover, The ↓ Gas density → the ↑ P at different SEOP pressure. this can be seen in with mixtures I (5% of ^{129}Xe, red square(□), with 95% of N_2). The ↑ gas density the ↓ P at different SEOP pressure. This can be seen in with IV (78.2% of ^{129}Xe, with black circle(●),with 20.8% of N_2).

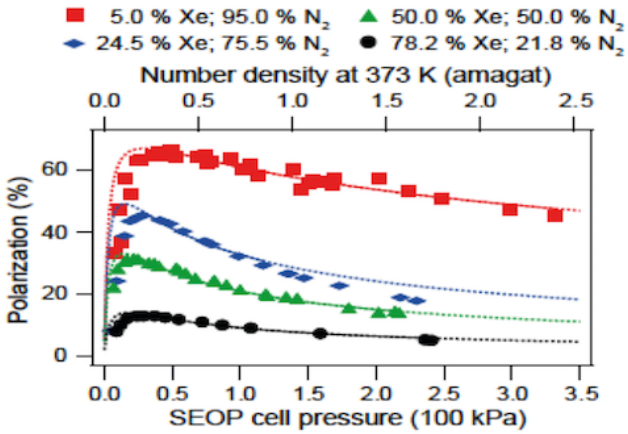


Figure 5.11: The polarization obtained for different gas mixtures of ^{129}Xe with buffer gas N_2 as a function of SEOP pressure using 30 W of circular polarised laser light, (Meersmann and Brunner, 2015).

Polarization percentage (%) of HP ^{129}Xe as a function of SEOP Pressure. Optical pumping was carried out for mixtures I (5% of ^{129}Xe, red square(□), with 95% of N_2), II (24.5% of ^{129}Xe, with blue diamond(◇), with 75.5% of N_2), III (50% of ^{129}Xe, green triangle(△), with 50% of N_2), and IV (78.2% of ^{129}Xe, with black circle(●),with 20.8% of N_2) under 20 W laser illumination in a pair of Helmholtz coils. Data was collected using 9.4 T after a stopped-flow delivery cycle using temperature of 373 K. Figure 5.11 shows the polarization of different ^{129}Xe mixtures as a function of SEOP pressure (Meersmann and Brunner, 2015).

5.9.3 Krypton Polarization

Figure 5.12 shows the polarization of different ^{83}Kr mixtures as a function of SEOP pressure. It also gives a clear information on polarization behaviour. The ↓ SEOP Pressure → the ↑ P of signal from Gas mixture. Moreover, The ↓ Gas density → the ↑ P at different SEOP pressure. This can be seen in with mixtures I (5% of ^{83}Kr, red square(□), with 95% of N_2). The ↑ gas density the ↓ P at different SEOP pressure. this can be seen in with IV (78.2% of ^{83}Kr, with black circle(●),with 20.8% of N_2).

Polarization percentage (%) of HP ^{83}Kr as a function of SEOP Pressure. Optical pumping was carried out for mixtures I (5% of ^{83}Kr, red square(□), with 95% of N_2), II (25% of ^{83}Kr, with blue diamond(◇), with 75% of N_2), III (49.5% of ^{83}Kr, green triangle(△), with 50.5% of N_2), and IV (74.1% of ^{83}Kr, with black circle(●),with 25.9% of N_2) under 20 W laser illumination in a pair of Helmholtz coils. Data was collected using 9.4 T after a stopped-flow

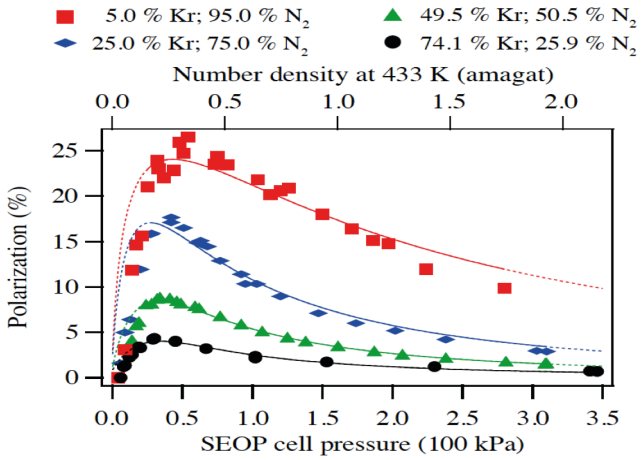


Figure 5.12: The polarization obtained for different gas mixtures of ^{83}Kr with buffer gas N_2 as a function of SEOP pressure using 30 W of circular polarised laser light, (Meersmann and Brunner, 2015).

delivery cycle using temperature of 433 K (Meersmann and Brunner, 2015).

5.10 Application of Hyperpolarised Noble Gas

5.10.1 ^{129}Xe Ventilation imaging

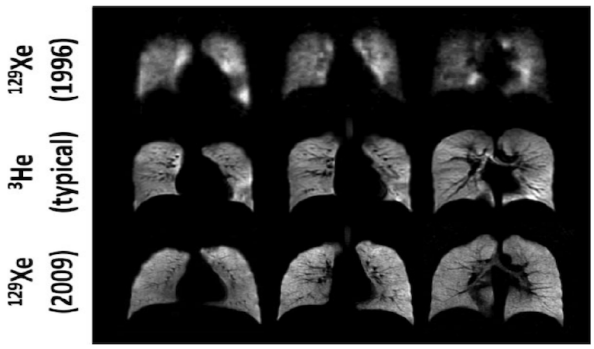


Figure 5.13: Improved MRI image from ^{129}Xe compared to ^{3}He Image, (Mugler and A, 2013).

As ventilation imaging is considered as common technique used for scanning lung tissue in MRI, high signal intensities will be detected from normal airflow inside lung tissues. On the other hand, low signal intensities on ventilated MRI image represent an area of partial or total airflow obstruction within the acinary and conducting zone of lung. A healthy subject was scanned by hyperpolarised ^{129}Xe and he has been scanned again using hyperpolarised ^{3}He . The results were showing an improvement of ^{129}Xe image quality. Although ^{129}Xe has low gyromagnetic ratio. The use of a dedicated RF coil and a large dose of ^{129}Xe shows a

Table 5.2: 3 Dimensional Fast Gradient Sequence with breath hold

Sequence Parameters			
Parameter		**Parameter**	
Repetition Time	6.7 ms	**Matrix Size**	128×128
Echo Time	1.5 ms	**No. Of slice**	14
Flip Angle	1°	**Slice Thickness**	15 mm
Field of View	40×40 cm	**Bandwidth**	15.63 kH_z

similar result that is obtained from ^3He. This is seen in in Figure 5.13. A lung functional MRI is a simple application could be generated from ^{129}Xe gas density by using static ventilation scan this achieved by using two Dimensional or three Dimensional Fast Gradient Sequence with breath hold (3D GRE BH (Mugler and Altes, 2013).

Shukla et al. (2012) had performed 3D GRE BH Sequence with parameters shown in table 5.2: He used a 3T magnet system Scanner and Quad birdcage coil tuned to 35.34 MHz and 1 litre of ^{129}Xe gas mixture. The protocol was performed in variety of subject such as healthy, asthmatic, Chronic Obstructive Pulmonary Disease (COPD) patients, Cystic Fibrosis disease (CF), and Radiation Induced Lung Injury (RILI) subjects which are shown in Figure 5.14 below.

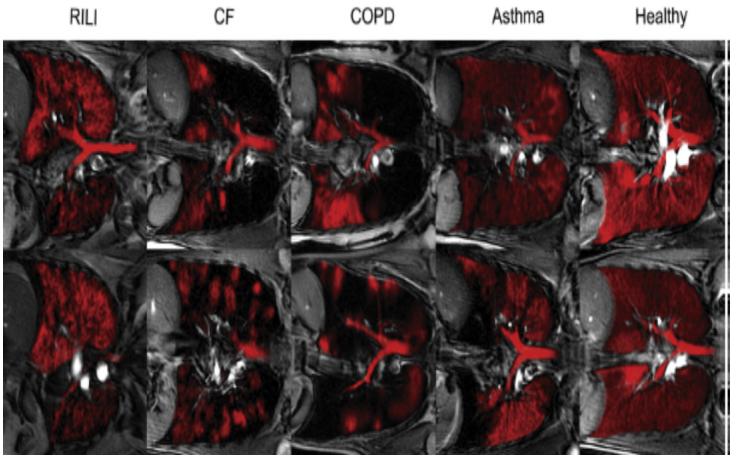


Figure 5.14: MRI ^{129}Xe Images of Various Lung Disease, (Shukla et al., 2012).

Fast Low Angle Shot (FLASH) shown at Figure 5.15 uses radio frequency excitation pulses with a tip angle smaller than $\pi/2$ pulse and read gradient for producing GRE echo. The sequence flip angle usually creates equilibrium state of longitudinal magnetization. However, the steady state or x-y magnetization is eliminated by a spoiler gradient (Lilburn et al., 2013; Zhao et al., 1996).

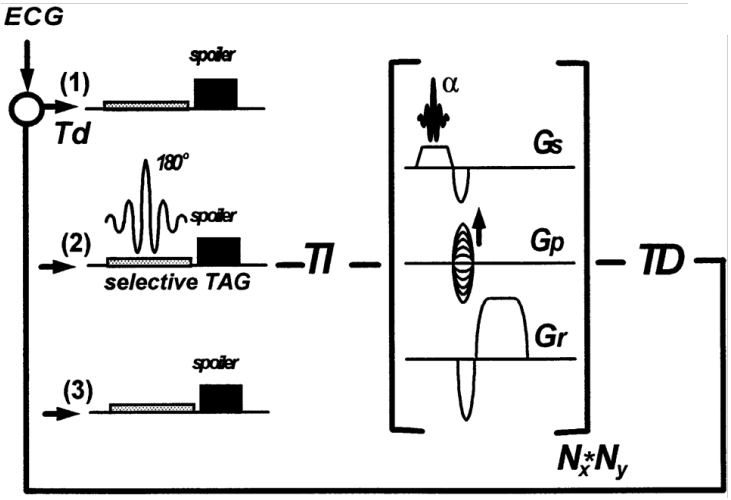


Figure 5.15: Fast Low Angle Shot (FLASH) Sequence, (Hatabu et al., 1999).

A high T_1-weighted and reduced $T_2^\star$-weighted contrast can be acquired by the FLASH sequence if large flip angle is used. On the other hand, when small flip angle is used, the T_1 recovery curves play a minor role and gas density (^{129}Xe density) weighting is increased although the most usable sequence for detection hyperpolarised noble gas is (FLASH. It is rarely used in lung and pulmonary imaging. The sequence has been developed by Zhao et al. (1996) to have a variable flip angle (VFA) that uses the maximum amount of HP gas density and improve the image contrast without adding any spoiler to the sequence. Because the spoiler will kill any polarization that already generated. Figure 5.16 shows the advantage of using a VFA sequence that overcomes the constant flip angle (Lilburn et al., 2013; Kino et al., 2009; Zhao et al., 1996).

FLASH images is identified by looking for fluid filled space in the organs. For example cerebrospinal fluid (CSF), ventricles and spinal cord in central nervous system, fluid in the gall bladder (GB) and common bile duct (CBD), fluid in the urinary tract (UT), and pathological edema. Fluids appear as dark on FLASH image by having hypo-signal (Low) intensity. However, the air containing oxygen appears dark with low signal intensity of hypo-signal regions, which make the sequence useful in chest imaging especially if contrast agent is used (Brant-Zawadzki et al., 1992; Haase et al., 1986; Saguintaah et al., 2002).

Another imaging Technology that is useful in gas density is the dynamic ventilation from **echo plan imaging** (EPI). EPI is considered the fastest imaging acquisition up to date, which requires a train of gradient refocusing pulse at each repetition time (TR). It allows sampling the whole phase encoding in one train by a process known as single shot or snap shot imaging.

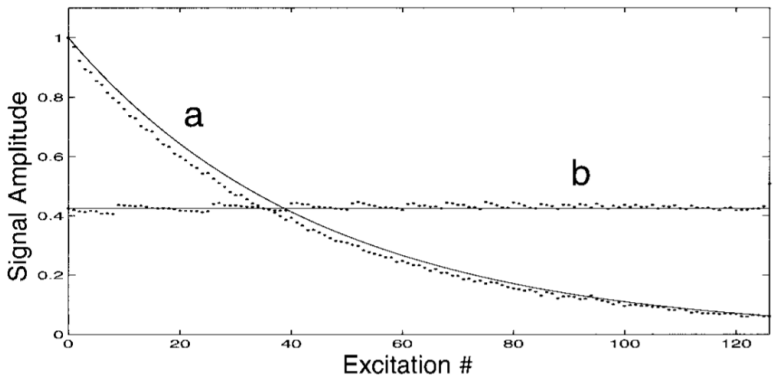


Figure 5.16: Signal Intensity comparison between (a) fixed flip angle and (b) variable flip angle, (Lilburn et al., 2013; Zhao et al., 1996).

EPI has low specific absorption rate (SAR), this allows the use of low RF power. The image weighting could be single or multi-slice contrast that is controlled by creating the initial echo when using spin echo, gradient echo, or inversion recovery echo methods (Stehling et al., 1991; Cockburn, 2003). EPI allows faster imaging when ^{3}He was used, which could be useful when ^{129}Xe and ^{83}Kr were used due to faster $T_2^{\star}$ decay yet the spatial domain resolution may be diminished. It also does't demand new delivery of HP gas. Thus it is considered less HP gas consuming and allows studying the gas distribution with only one inspiration (Gierada et al., 2000). Table 5.3 shows parameters were used with a group of emphysematic subject by using dynamic sequence:

Table 5.3: 3 Dynamic EPI sequence

EPI Sequence Parameters			
Parameter		**Parameter**	
Repetition Time	40 ms	**Matrix Size**	32×64
Echo Time	12.1 ms	**Echo Train Length**	32
Flip Angle	22°	**Slice Thickness**	10 mm
Field of View	22×45 cm	**Bandwidth**	N/A kH_z

The dynamic sequence was performed by 1.5T magnet using time interval between each acquired images 0.40, 0.80, 1.2, and 4.0 seconds respectively. The result of this sequence can be seen in Figure 5.17 which shows that gas was first seen in middle lobe then followed to be seen in the lower lobe and finally seen in upper lobe of rat lung (Gierada et al., 2000).

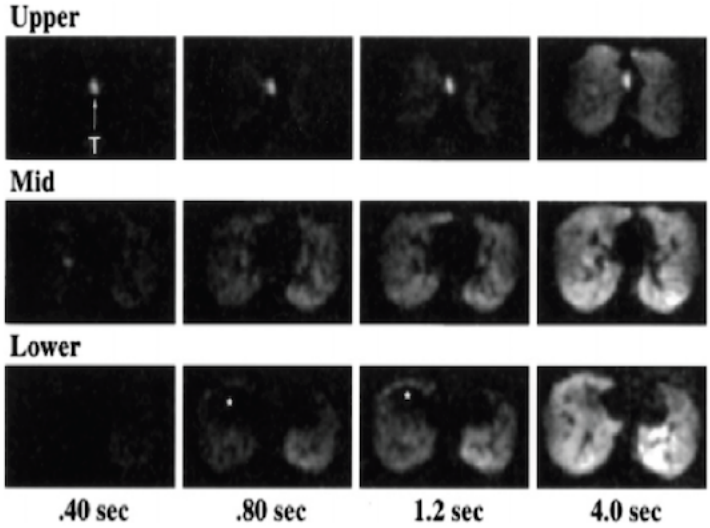


Figure 5.17: MRI images from Dynamic EPI sequence, (Gierada et al., 2000).

5.10.2 ^{129}Xe Perfusion Imaging

Electron shielding results in an effective magnetic field at the nucleus, B_{eff} which is given by:

$$B_{eff} = B_0(1-\sigma) \tag{5.27}$$

where σ is called the shielding (or screening) constant and is proportional the strength of the magnetic field at the nucleus due to the orbiting electrons. The resultant Larmor frequency of the nucleus is described by:

$$\nu = \left(\frac{\nu}{2\pi}\right) B_0(1-\sigma) \tag{5.28}$$

This change of the resonance frequency is known as the chemical shift. Figure 5.18 illustrate the NMR signal of ethyl acetate which consists of spectrum of peaks at different frequencies for each chemically unique nucleus.

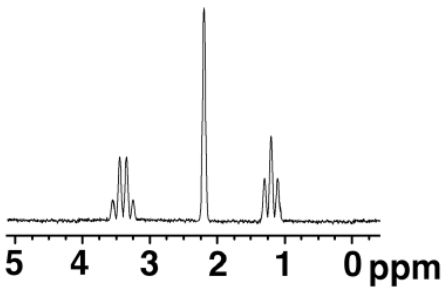


Figure 5.18: Proton spectrum of ethyl acetate showing unique peaks for each of the three types of protons.

Perfusion is a technique usually used to study ^{129}Xe behaviour between alveolar and capillary during the dissolving phase. As the ^{129}Xe has ability to dissolve in different phases represented in chemical shift which resonate at approximately 0 ppm in gas phase (airspace), 197 ppm at lung tissues(alveolar epithelium, interstitium, capillary endothelium, and plasma) and 211 ppm in red blood cells (RBCs). Figure 5.19 shows the three location of dissolved ^{129}Xe (Lilburn et al., 2013).

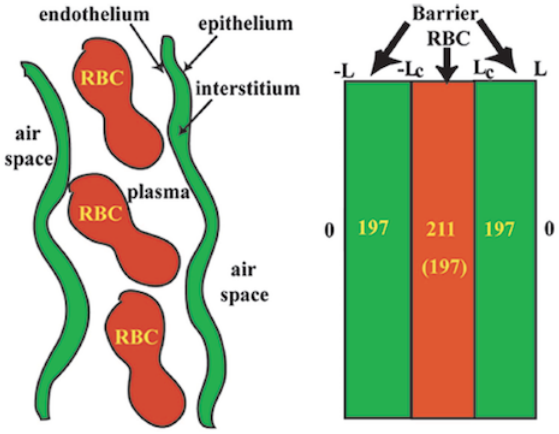


Figure 5.19: ^{129}Xe in the Lung Tissue Dissolved Phases, (Driehuys et al., 2006).

Xenon polarization transfer contrast (XTC) is a technique that is used to generate maps of two lung parameters. First, **MXTC-F** which represents gas phase polarisation for a long duration. Second, **MXTC-S** represents the Xenon dissolved phase in the lung (Meersmann and Brunner, 2015). Figure 5.20 shows a schematic diagram of MXTC technique of image acquisition.

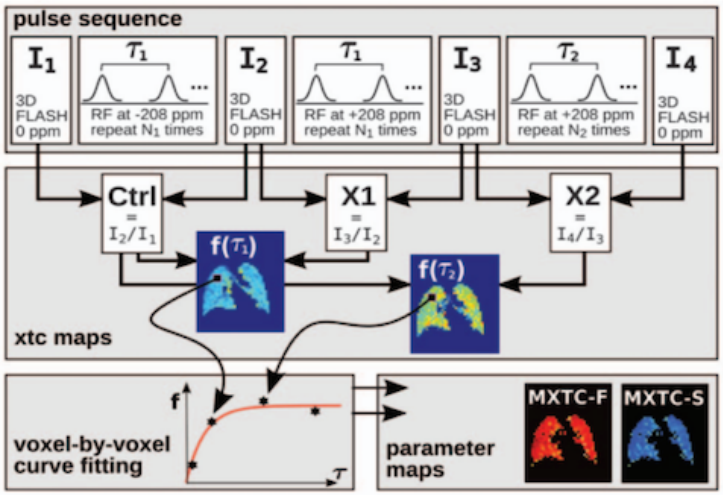


Figure 5.20: Schematic Diagram of MXTC Technique of Image Acquisition, (Driehuys et al., 2006; Meersmann and Brunner, 2015).

Xenon gas alveolar capillary transfer (XACT) is an emerging technique based on the previous **XTC** uses an excitation pulse that could eliminate the peak at 211 ppm leaving the peak at 197 ppm. Driehuys et al. (2006) uses this technique in figure 5.21 to image a rat lung at different phases.

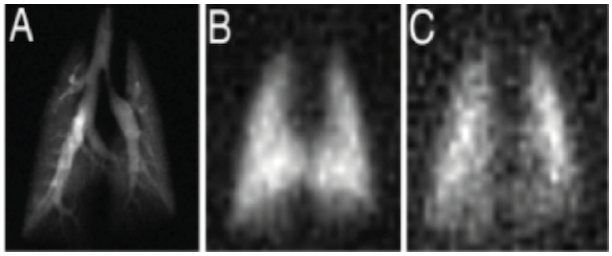


Figure 5.21: Coronal images of Rat lung (A)^{129}Xe in (airspace) gas phase, (B)^{129}Xe in the lung tissue dissolved phase, (C)^{129}Xe in RBC dissolved phase, (Driehuys et al., 2006).

5.10.3 ^{83}Kr Media (Surface) Interaction

Pavlovskaya et al. (2005) have shown that ^{83}Kr has the ability to be used as a contrast agent in T_1 weighted image. However, this relies on the surface hydration. The team has used two hydrophilic glass beads samples: the first sample was untreated by silicone while the second has been treated with silicone. In figure 5.22 the beads were about 1.0 mm in size for the void space to give the similar size of human alveoli . Their work has provided that ^{83}Kr has remained longer on the second sample after scan with longer time which proves that T1 relaxation is longer when ^{83}Kr is used.

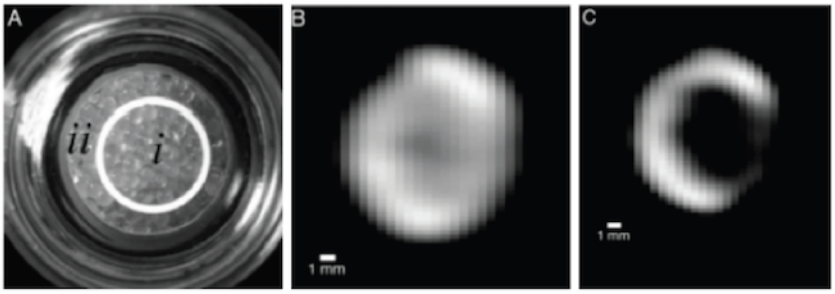


Figure 5.22: The ^{83}Kr MR images with Flash sequence to hydrophilic beads (i) untreated (ii) treated beads, (Pavlovskaya et al., 2005).

5.10.4 ^{83}Kr Surface Hydration Effect on T_1 Relaxation

Cleveland et al. (2007) explained how T_1 relaxation is affected by the type of surface. He

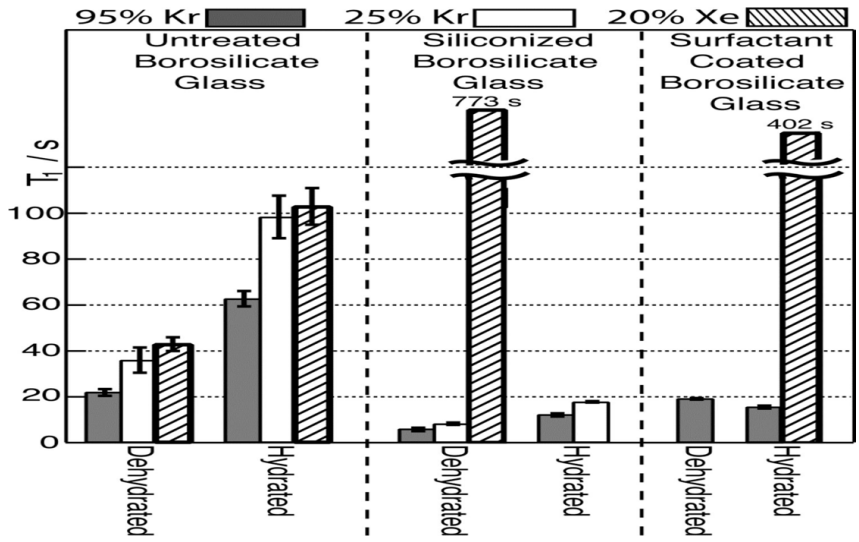


Figure 5.23: The T_1 relaxation time comparison between hydrated and dehydrated surface, (Cleveland et al., 2007)

found that a hydrophilic surface yield a lower longitudinal relaxation time compared to hydrophobic surface. This is later explained as powerful relaxation tumbling between ^{83}Kr and surface resulting a faster T_1 relaxation. One year later, same authors have shown in figure 5.23 a massive increase in T_1 time when they used a hydrated surface with an untreated Glass with 95% of ^{83}Kr.

5.10.5 ^{83}Kr Concentration Vs T_1 Relaxation

Brinkmann and Kuhn (1980) showed a linear relationship between T_1 relaxation rate and the ^{83}Kr density in a sample using the equation:

$$\frac{1}{T_1} = \rho(2.35pm0.05) \times 10^{-3}\text{rad/sec} \tag{5.29}$$

where ρ is the Kr density. Kr $\Leftrightarrow$ Kr tumbling causes the T_1 relaxation rate which depends on the gas density. T_1 decay rate is dependent on the ^{83}Kr gas concentration in the gas mixture. When ^{83}Kr and ^{3}He gas mixture is used, a longer T_1 time is observed. Both Kr $\Leftrightarrow$ Kr tumbles with a Kr $\Leftrightarrow$ Kr Van Der Waals complexes causes a stronger spin collision of the ^{83}Kr gas and a decrease of the T_1 decay time compared to Kr $\Leftrightarrow$ He gas phase collisions. Due to fast exchange, ^{83}Kr gas phase decay is caused by surface-gas collisions. So on any co-adsorption molecules close to the surface can limit the ^{83}Kr -surface interactions and thus diminish the ^{83}Kr tumbling with the surface. An example for co-adsorption molecules is mentioned in

Cleveland et al. report which shows that the existence of a small water amount increases the ^{83}Kr T_1 decay in glass beads (porous medium) (Brinkmann and Kuhn, 1980; Abatzoglou et al., 2007).

CHAPTER 6

HYPERPOLARISED LASER CHARACTERISTICS

6.1 Introduction

The laser unit is a central part in hyperpolarisation system. The laser unit plays a major role in the optical pumping concept. The laser is the primary source of the physio-chemical process (described previously in chapter 4, section 4.2) called optical pumping which helps to pump noble gases into higher levels of polarisation compared to its thermal state.

The laser unit used in this process is a high power system provided by fibre optic that is coupled to a diode laser. Therefore, we will review some of the basics of this device, the cooling method required as well as some of the experiments used in determining the adequacy of this device. Particularly with regard to the hyperpolariser used for noble gases pumping, there are two basic experiments to test the laser system. The first is to determine the power limits and it is strength from the power supply used for the device. Second, is to make sure that the laser generated is on the appropriate line shape designed for it. In this chapter we will discuss in these experiment details, how they work and what their expected output is.

The remarkable development of the laser, which followed four consecutive decades of invention of the first device, led to the emergence of solid-state and gas lasers. Taking into consideration laser gas generation is being primarily based on electrical discharge, while solid state laser generation is based on flash lamps and semiconductor diode laser arrays. (Krupke et al., 2003) offered a new class of continuous wave(CW) laser which combine the feature of both previous laser families.

The new class was based on excitation of atomic alkali vapour. The design concept was extracted from Konefał proposal of Rb resonance D_2 and D_1 transition using laser amplifier(Konefał, 1999). Because of the tiny quantum energy difference between the D_2 and the D_1 transitions ($\approx$ 2% for Rb), the neutral alkali atoms have the potential to be especially efficient laser species in three-level lasers, which can be used to produce effective pumping of D_2 transition. By using narrowband, highly powered coherent diode-laser sources with air cooling system connected to inversion less amplifier and laser oscillation without population inversion have been demonstrated on the 795-nm D_1 transition of rubidium.(Zibrov et al., 1995)

The laser light beam is controlled and generated by power supply (shown in figure 6.1A) that is connected to the laser system which is limited to 46.2 A and 2.37 V. Because of a laser is a source of heat, the laser source is also connected to an air cooling system (shown in figure 6.1B) to control the laser temperature to the required operating temperature of 20 °C

Therefore, obtaining the required flow of the laser beam to complete the optical pumping process requires a confirmation that the laser unit is used to efficiently discharge the maximum necessary power and that the appropriate spectral line width is located at the correct spot of 794 nm. This check up is applied by two experiments that help to determine the accuracy and effectiveness of the laser system.

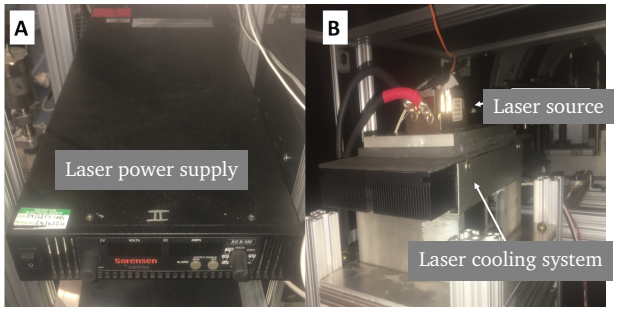


Figure 6.1: (A): Laser Power Supply (B): Laser Cooling System.

6.2 Material and Method

The method used to achieve the actual purpose of these experiments is based on a set of materials and tools that are present at the (SPMIC) laboratories that will contribute to the identification of extracted data.

6.2.1 Laser Power Output Experiment

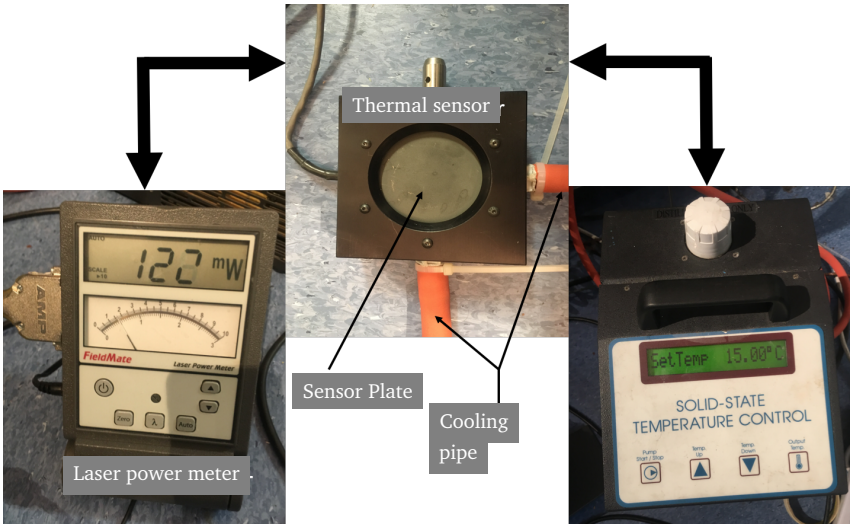


Figure 6.2: Laser Power Meter, Thermal Sensor, and Solid State Temperature Control used for Experiment Set Up.

The relationship between the electrical current and laser output can be studied using the following tools as they appear in figure 6.2: **Thermal sensor** placed inside the hyperpolariser (shown in figure 6.3 A) to face and meet the the circular light beam emanating from the laser device (as seen in figure 6.3 B). This sensor is attached to a **solid-state temperature control unit** by cooling pipe to cool the sensor plate during the measurement process. In addition, the sensor was attached to **laser power meter**. The power meter reads the amount of power produced by the laser flow which reached the sensor. Each time the current is gradually increased with an incremented of 5 A using the laser power supply and the amount of power from the laser power meter is recorded. Please note that current continued to increase manually until the maximum current for full laser power is achieved at 46.2 A. The extracted data is then recorded for further processing and analysing which will help to give an initial and clear perception of laser source performance based on the amount of current input.

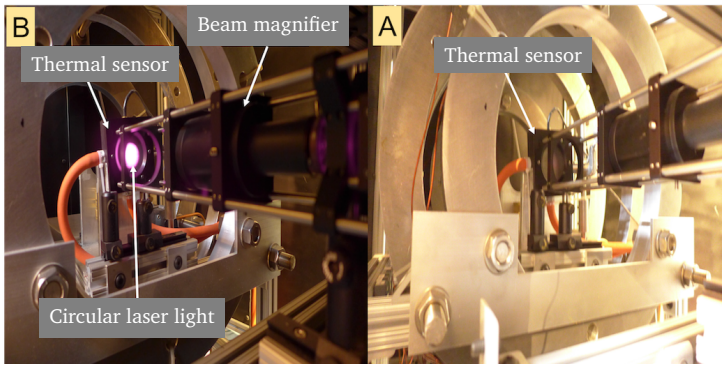


Figure 6.3: (A): Thermal Sensor without Direct Laser Beam,(B): Laser Circular light Facing Thermal Sensor Inside Hyperpolariser.

6.2.2 Spectral Line Shape Experiment

As for the relationship between spectral line shape and maximum equivalent laser power used, which is based on it; we can determine the efficiency and the effectiveness of the laser device. This gives us a clear idea on the possibility of using the laser device again to achieve the objective of using it in medical application either after maintenance process, repair one of its components, or even after the first time installation to ensure compliance with specification.

The tools which were used to achieve this experiment are shown in figure 6.4 were as the following: a **piece of paper** facing circular light the emanating from laser source inside the hyperpolariser. When laser light hits the piece of paper, it will emit scatter laser light. A **fibre optic cable** installed by placing it facing the piece of paper to detect the scattered laser light. The fibre optic cable is connected to an **optic spectrometer box** which is attached to a **computer** which contains an **Ocean Optic SpectraSuit** software. This will read the scattered light to determine the spectral line width of the laser source.

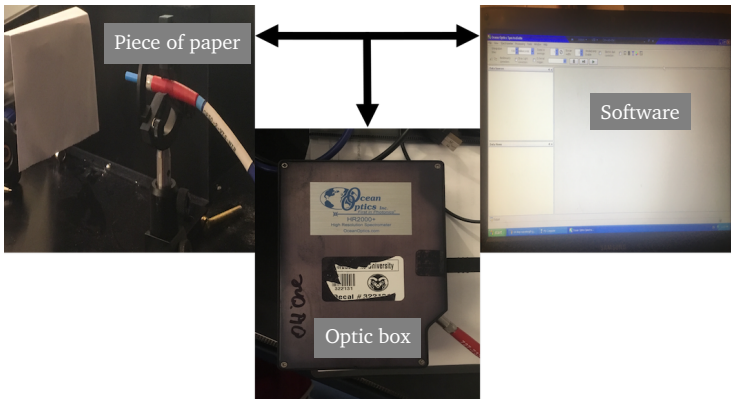


Figure 6.4: Fibre Optic cable connected to Computer Software via Spectrometer

6.3 Results & Data Analysis

6.3.1 Analysing Laser Power Output Data

Table 6.1: Extracted Data From Laser Power Output vs current and voltage Experiment

Current (A)	Voltage (V)	Power (W)	Power (W) After 5 min
46.2	2.29	24	24.2
40.6	2.22	20.9	20.9
35	2.15	17.4	17.6
30.1	2.08	14.5	14.3
25.2	2.02	11.3	11
20.3	1.95	7.64	7.5
15.4	1.88	4.45	4.46
10.5	1.8	1.37	1.39
5.6	1.72	0.80	0.85
0	0	0	0

The measured data from experiment mentioned in section 6.2.1 which was recorded in table 6.1, showed that maximum laser power output generated was 24 W of Continuous wave laser beam after optics was initially used. The data from table 6.1 were analysed using Igor Pro 7 (64bit) software to generate a positive co-relation line shown in figure 6.5 indicating laser output power in watts as a function of operating current in amperes. The power output was ideal outcome from laser performance for optical pumping. On the other hand, the experiment does not give a clear information about the spectral line behaviour.

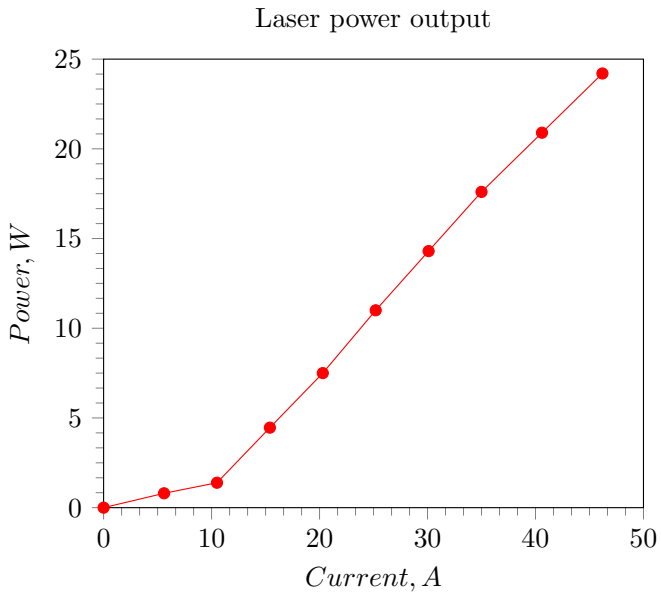


Figure 6.5: Laser Power Output Versus Operating Current

6.3.2 Analysing Spectral Line Shape Data

Ocean Optic SpectraSuit software uses real time mode to read the scattered laser light beam which displayed in figure 6.6 to verify the wavelength of 794.7 nm that is generated when laser power is at maximum output. Unexpectedly, another peak between 790 to 793.5 nm was found in the graph which indicate bad performance of the current laser from hyperpolariser type II.



Figure 6.6: laser intensity of spectral line shape in 794.7 nm wavelength

The data from figure 6.6 were extracted via computer and then analysed using Igor Pro 7 (64bit) software to integrate and find the area under each peak. After processing the data using multi-peak fitting function, the figure 6.7 shows produced graphs.

In figure 6.7(A) the data were de-convoluted to separate peak 1 at 794.7 nm from peak 0 in the range 790 to 7930.5 nm. Since peak 0 indicate losses from peak 1, data in figure 6.7(C) were normalised to residual to generate multi peak fitting function shown in figure 6.7(B) blue dots is the plot peak with corrected baseline and the red line is the fitting line for the both peaks.

The report in figure 6.8 shows the total peaks area of 5563 ± 11127, and the area integrated for each peak separately. It also gives an information on the type of each peak, full width of halve maximum value, location plus height, and the fitting parameters of each peak.

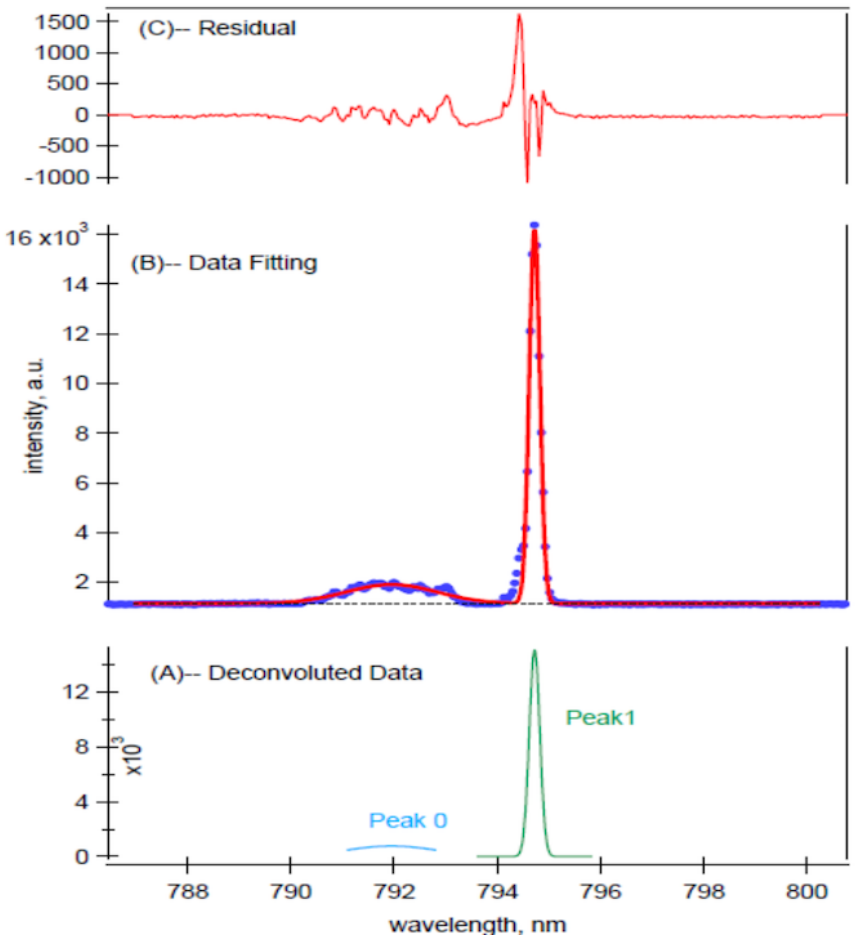


Figure 6.7: analysed data (A) extracted data De-convoluted, (B) multi-peak data fitting, and (C) residual data from both peak

6.4 Discussion

The analysis of initial data from laser output experiment have resulted a graphical detection to 1% loss of power output from the 30 W continuous wave diode laser device. This loss due to the presence of linear polariser and glass surfaces of beam expander lenses of optical laser and the presence of quarter wave plate $\lambda/4$. In addition, laser output loss has caused the final laser to generate 24 W continuous wave for SEOP process. This 1% loss of laser power is equivalent to 6 W decrease of the primary laser power output which can be seen from table 6.1 and figure 6.5. Furthermore, another loss was detected from the second experiment of spectral line width. The appearance of peak 0 adjacent to the main peak1 in figure 6.7 shows a loss in the laser output. The data analysis in figure 6.8 shows the area under peak 0 of 1687.6 compared to 5563.9 from total peak area which indicates approximately 30% loss of the laser. Since it is known that the laser output is about 24 W, this leaves 70% of laser output for SEOP, which is equivalent to 16 W.

Fit completed 16:04 28 August 2018
Y data wave: root:intensity[799, 1112]
X data wave: root:wave_length
Chi square: 1.1323e+07
Total fitted points: 314
Multi-peak fit version 2.22
Total Peak Area = 5563.9 +/- 111.27

Baseline	Type: Constant			
	y0 =	1134.4	+/-	13.768
Peak 0	Type: Gauss			
	Location =	791.95	+/-	0.051884
	Height =	764.41	+/-	40.272
	Area =	1687.6	+/-	107.15
	FWHM =	2.074	+/-	0.13264
	Fit function parameters			
	Location =	791.95	+/-	0.051884
	Width =	1.2456	+/-	0.079658
	Height =	764.41	+/-	40.272
Peak 1	Type: Gauss			
	Location =	794.72	+/-	0.00089985
	Height =	15071	+/-	112.78
	Area =	3876.3	+/-	29.985
	FWHM =	0.24162	+/-	0.0020848
	Fit function parameters			
	Location =	794.72	+/-	0.00089985
	Width =	0.14511	+/-	0.0012521
	Height =	15071	+/-	112.78

Figure 6.8: The Report shows Type and Fitting Parameters of Both Peaks

6.5 Conclusion

Overall, as previously discussed from both laser experiment results and analysis, there is a huge loss of approximately half of the main output of the 30 W continuous wave diode solid laser source. This could reduce the efficiency of the polariser to produce a fully polarised noble gases for future experiments. The author suggests a replacement of new laser source within hyperpolariser type-II or to move to the new hyperpolariser type-III. Some SEOP could be performed with this laser source however this could be useful only for training purposes or when setting up for a new experiment trials.

CHAPTER 7

HP ^{83}KR T_1 RELAXATION AS SURFACE ANALYSER

7.1 Introduction

Hyperpolarised ^{83}Kr is a promising new biomarker for Pulmonary MRI. The noble gas is capable of providing surface sensitive contrast. Recent methodological advances in Spin Exchange Optical Pumping (SEOP) have produced signal intensities for HP noble gases that are increased by orders of magnitude over thermal polarization. This opens up the perspective of clinical usage of HP ^{83}Kr. Any usage of ^{83}Kr requires the development of novel procedures. The comparison between the thermal equilibrium polarisation percentage and hyperpolarised polarisation percentage produces the understanding of enhancement factor to reach the hyperpolarised signal from thermal signal. For example, a relaxation agent is required for measurement with thermal ^{83}Kr. The thermal polarization percentage of ^{83}Kr at 9.4 T magnet is (4.52 $\times 10^{-4}$ %) using 64 average, 2 bar of ^{83}Kr and SNR = 90. Therefore, when 3 T magnet is used hyperpolarised ^{83}Kr is considered using 8 average, 0.1 bar and SNR = 3, the polarization would be enhanced by factor of $8 \times 20 \times 30 = 4800$. This would increase the polarization from (4.52 $\times 10^{-4}$ %) in thermal ^{83}Kr to $4.52 \times 10^{-4} \times 4800 \times \frac{3T}{9.4T} = 0.69$ % using HP ^{83}Kr.

Aqua Foam material with various sizes which work as porous relaxing surface are explored through spin lattice relaxation measurement. The observed ^{83}Kr T_1 relaxation rates depend on the foam surface chemistry and on the surface-to-volume ratio. Also the foams were treated differently to suffer from hydration and dehydration process for each fundamental measurement this will be discussed in detail later within this experiment. The results of these experiments are discussed at the end of this chapter as well.

The (^{83}Kr) noble gas has a natural abundance of 11.5% and resonance frequency of 15.4 MHz at 9.4 T magnetic field strength, it is considered a stable NMR gas isotope. The physical property of its nuclear spin I = 9/2, make a ^{83}Kr nucleus possesses an electric quadrupole moment ($Q = 0.28 \times 10^{-28}\mathrm{m}^2$). The ^{83}Kr nuclei alignment with magnetic field can cause quadrupolar coherence which leads to quadrupolar splitting. Electric field gradient is induced in the electronic cloud of the noble gas atom from this type of alignment (Pavlovskaya et al., 2005; Cleveland et al., 2007). This has previously monitored when early NMR with dissolved in nematic phase liquid crystals is used and when optical NMR detection used with ^{83}Kr isotopes in quadrupole nutation experiments inside non-spherical glass containers (Ingman et al., 1991; Jokisaari et al., 1993). In the absence of unpaired electrons, the quadrupole moment is a dominating factor for relaxation of the ^{83}Kr nuclear spin in solid, liquid, and gas phase (Cowgill and Norberg, 1973; Stupic et al., 2006).

This experimental work will produce a systematic study of relaxation experienced by the hyperpolarised (hp) noble gas isotope ^{83}Kr in contact with surfaces. The T_1 relaxation of ^{83}Kr is found to depend strongly on the chemical composition of the surfaces in the vicinity of the gas. This effect is caused by quadrupolar interactions during brief periods of surface adsorption that are the dominating source of longitudinal spin relaxation in the ^{83}Kr atoms (Meersmann et al., 2009; Horton-Garcia et al., 2005).

Recently, direct NMR measurement of ^{83}Kr gas inside a number of zeolites has been studied. The line shape of ^{83}Kr was found to depend on the internal cage structure and the charge of porous materials. The ^{83}Kr chemical shift has been explored as a function of krypton loading in these materials. Despite the low sensitivity of natural abundance ^{83}Kr (i.e. about 3.8% of the sensitivity obtained from thermally spin polarized ^{129}Xe), ^{83}Kr loading measurements in zeolites can typically be achieved within a couple of hours at a high field

strength (i.e. 9.4 T) with thermally polarized krypton. This is possible due to ^{83}Kr is fast spin lattice relaxation that ranges from milliseconds to tens of milliseconds (Horton-Garcia et al., 2005; Stupic et al., 2006).

The low signal intensity of thermally polarised ^{83}Kr remains a problem for probing small volume-to-surface material due to low ^{83}Kr loading and increased T_1 relaxation times in large surface-to-volume materials with values ranging from seconds to many tens of seconds. However, experiments with small volume surface material have become attainable and practicable because of optical pumping development of laser applications that lead to the production of hyperpolarised (hp) ^{83}Kr for NMR and MRI applications (Stupic et al., 2006; Albert and Hane, 2016; Meersmann and Brunner, 2015).

7.2 Materials and Methods

7.2.1 ^{83}Kr Optical Pumping

In the past, group of scientist have explored alkali metal vapour optical pumping of quadrapolar noble gas nucleus, such as ^{83}Kr. The SEOP experimental set-up used here is similar to the one reported previously in the literature for the production of hp ^{129}Xe (I = 1/2) (Meersmann and Brunner, 2015; Schaefer et al., 1990; Grover, 1978).

The gas mixture type II used for all experiments of a high concentration of natural abundance krypton [mentioned previously in chapter 5 section 5.9.3] (typically 25% and about 75% of molecular N_2). Note, that N_2 is added for radiation quenching purposes as in ^{129}Xe SEOP. The pumping cell gas pressure were in the range of 1.0 bar to 2.5 bar. Pumping with high noble gas density is found to be vital for obtaining the highest signal intensities with HP ^{83}Kr. Unlike for HP ^{129}Xe, the freezing for storage method is not suitable for HP ^{83}Kr. The freezing will cause quadrapolar relaxation, which in turn will destroy the HP ^{83}Kr relaxation (Mortuza et al., 2003).

In figure 5.12, The HP ^{83}Kr polarization at 2.5 bar was 5% for 25% ^{83}Kr and 75% N_2 mixture. When a 30 W continuous wave diode array solid-state laser (24 W after optics) is applied to the pump cell of stopped flow process, this leads to a signal enhancement of $\frac{5\%}{4.52\times10^{-4}\%}$ close to 11060 times greater than the ^{83}Kr thermal polarization (i.e $P_{Thermal} =$

4.52×10^{-4}%) at 9.4 T and 20 °C (≈ 300 K) (Horton-Garcia et al., 2005).

A gas mixture of 25% Krypton and 75% Nitrogen is used for pumping within Pump cell (length = 125 mm, I.D. = 25 mm) that contains 1 g of rubidium). The temperature of the pump cell is kept between 150 °C and 160 °C, a pumping cell temperature that is about 10 °C to 20 °C higher than the temperature typically used for HP ^{129}Xe. In the stopped flow experiments the samples are evacuated to 0.0001 bar and the gas mixture is exposed to laser radiation inside the pump cell for 6 min. Subsequently, the optically pumped krypton is transferred using pressure equalization into the samples where a delivered HP krypton gas pressure range of 1 – 2 bar is maintained.

7.2.2 NMR Measurements

Experiments are performed within a 9.4 T Oxford wide-bore (89 mm) superconducting magnet using 30 mm in diameter RF coil (probe), that resonates at a low resonance frequency of 15.4 MHz KEA software (Magritek, Malvern, USA) a magnetic resonance spectrometer linked to a computer. Matlab was used to fit and calculate T_1 values obtained from optical pumping data that represent the krypton signal intensity as a function of time when a series of sixteen pulse of 5° flip angle is applied and spaced evenly every 20 µs. For the experiments reported here, an amplitude of 26 µs RF pulse were used to be equivalent to 5° flip angle and the acquisition time of 102.4 ms.

7.2.3 Samples Design & Preparation

The Figure 7.1 shows the micro-structure of three different size of Aqua Foam that is used as a relaxing agent.

Figure 7.2 shows the foam according to the internal diameter as:

- Foam B which represent the Medium Surface-to-Volume with an internal diameter ranging from “0.1 -2.0 mm”.
- Foam C which represent the Small Surface-to-Volume with an internal diameter ranging from “0.5-1.0 mm”.

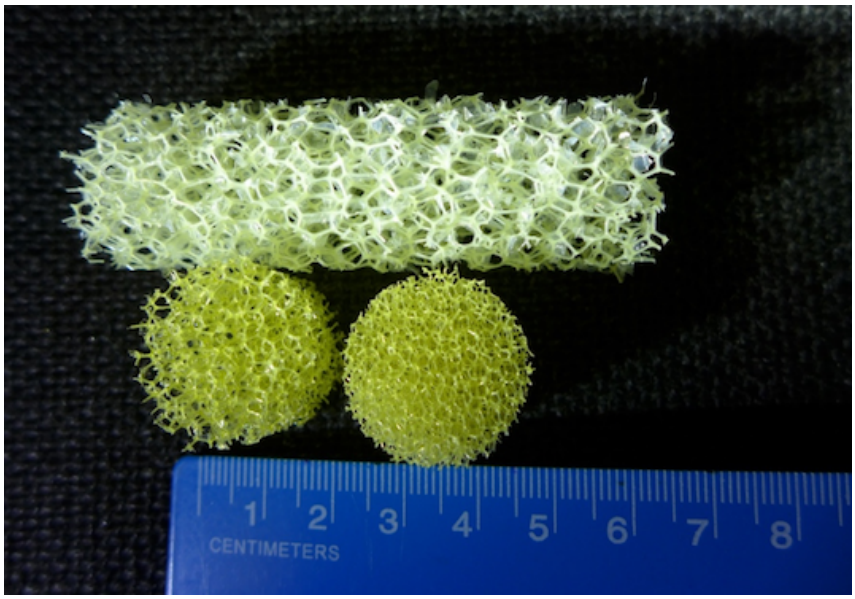


Figure 7.1: Micro-structure of Three Variable Size Relaxing Agent Foam

- Foam D which represent the Large Surface-to-Volume with an internal diameter ranging from “1.5 -2.5 mm”.

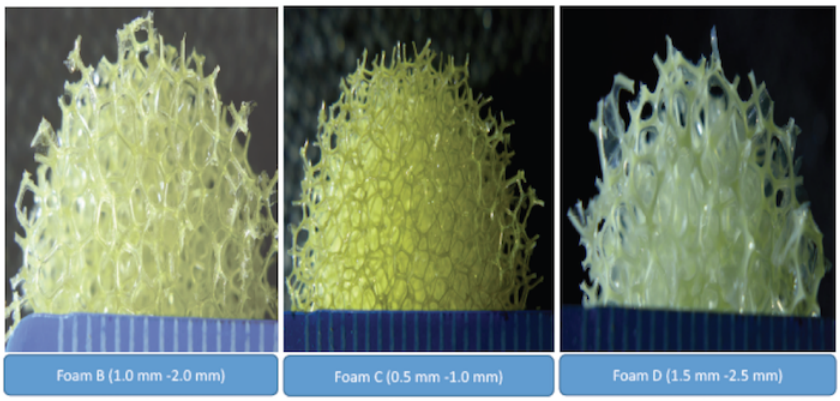


Figure 7.2: The Internal Diameter of Relaxing Agent B, C, and D

Medical universal vials (25mm in diameter and 92 mm in height) were modified at the sealing cover by adding 1/4 inch= 0.635 cm brass Swagelok connector to accommodate the foams to permit ^{83}Kr gas flowing through the foam’s surface within the vials. The ^{83}Kr gas was transferred from the polariser to samples via the Teflon pipe. Figure 7.3 shows five medical vials were used in the experiment as the following:

1. Sample A, (which is an empty vial)
2. Sample B,(which contains the foam B relaxing agent)
3. Sample C, (which contains the foam C relaxing agent)

4. Sample D, (which contains the foam D relaxing agent)

5. Sample E, (which also contains foam B but in this case the foam was dehydrated in vacuum oven for 24 hours using 50 °C)

6. Sample F, (which contained epoxy treated foam B)

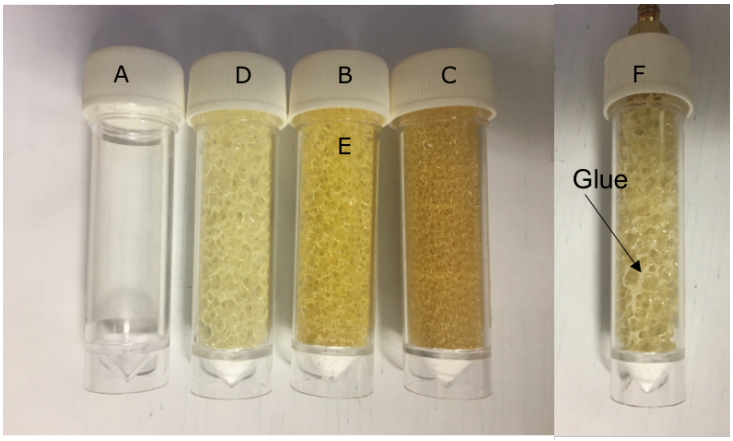


Figure 7.3: Relaxing Agent Foams filled within medical universal vials

The samples are classified according to the treatment process into three types:

1. Hydrated sample, which was exposed to high humidity

2. Dehydrated sample, dried up surface were water removed by using vacuum pupm for 24 h.

3. Oven sample, dehydrated in a vacuum oven at 50 °C

7.3 Result

7.3.1 Hydrated Treatment

Hydrated samples A and B were explored immediately after shuttling the HP ^{83}Kr gas to the samples. Figures 7.4 & 7.5 show the signal intensity decay of both hydrated samples A and B with time respectively. There is a significant decrease in T_1 value of the ^{83}Kr from 79 sec in the empty sample A to 7 sec when a high surface material is used as a relaxing agent in the (sample B). This shows the strong effect of the relaxation agent (foam) upon T_1 relaxation.

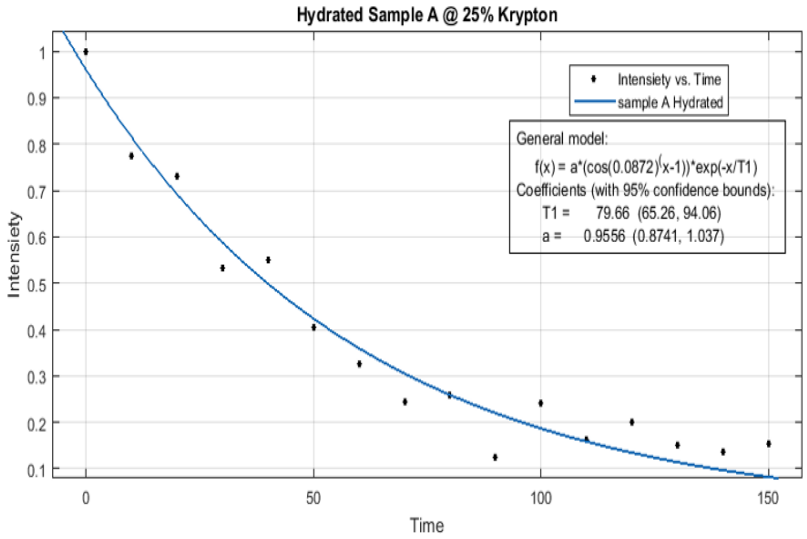


Figure 7.4: The signal Intensity as a function of time for Hydrated sample A (empty)

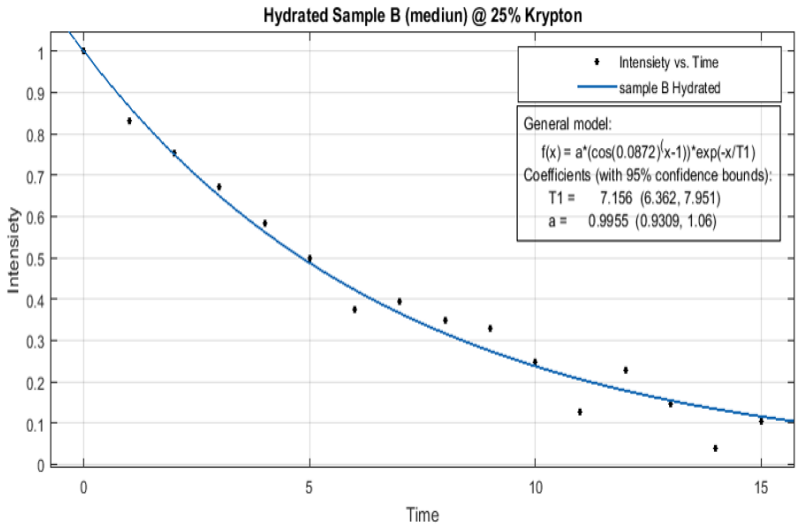


Figure 7.5: The signal Intensity as a function of time for Hydrated sample B (Medium surface-to-volume Foam)

^{83}Kr gas longitudinal relaxation is very slow in sample A while it is very fast in sample B of medium surface-to-volume agent.

In figure 7.6, The T_1 decay is decreased to 18 sec when high surface-to-volume of hydrated sample C is used. In figure 7.7, the T_1 decay is decreased to 9 sec when larger surface-to-volume hydrated sample D is used. There is no fundamental or significant difference between the T_1 value from hydrated samples B and D. This means both hydrated samples B & D can be used to induce fast ^{83}Kr relaxation.

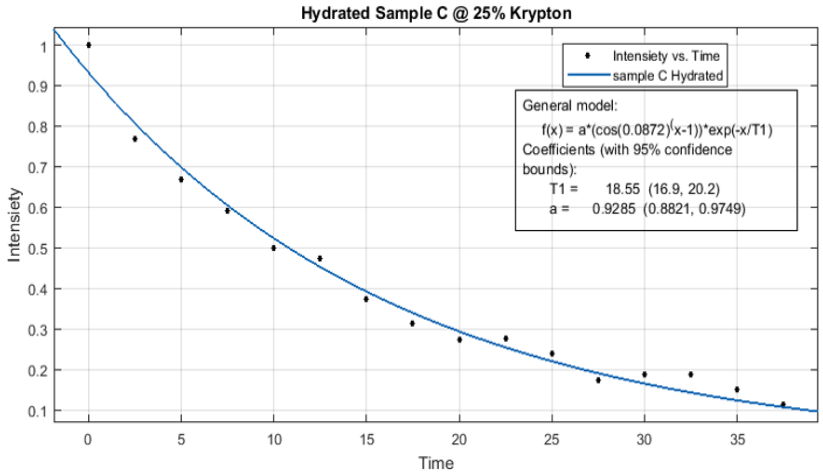


Figure 7.6: The signal Intensity as a function of time for Hydrated sample C (Small surface-to-volume Foam)

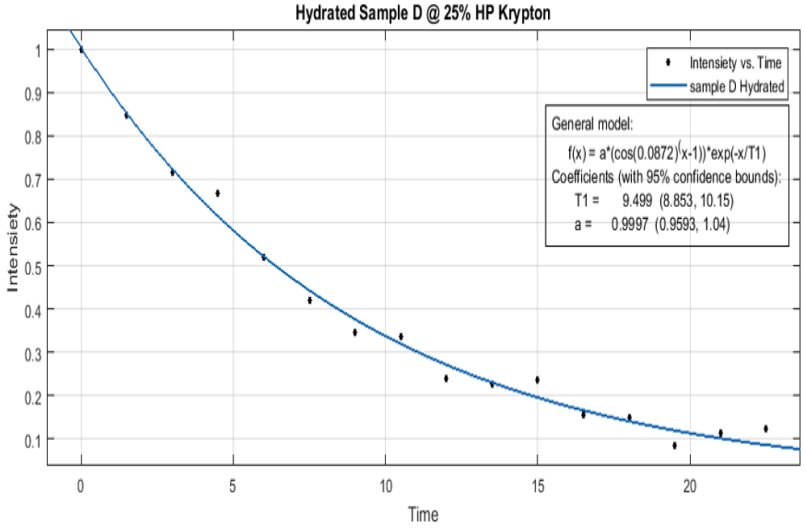


Figure 7.7: The signal Intensity as a function of time for Hydrated sample D (Large surface-to-volume Foam)

7.3.2 Dehydrated Treatment

Figures 7.8 & 7.9 show the T_1 decay for the dehydrated samples A and B over time respectively. Noticeably similar to hydrated treatment process, there is a significant decrease in T_1 value of the HP ^{83}Kr from 95 sec in the empty sample A to 3 sec when relaxing agent is used in the sample B.

Figures 7.10 & 7.11 show the T_1 decay for the dehydrated sample C and D over time respectively. Noticeably, there is no significant change in T_1 value of the HP ^{83}Kr from sample C and D. They both are in the 4 sec regime.

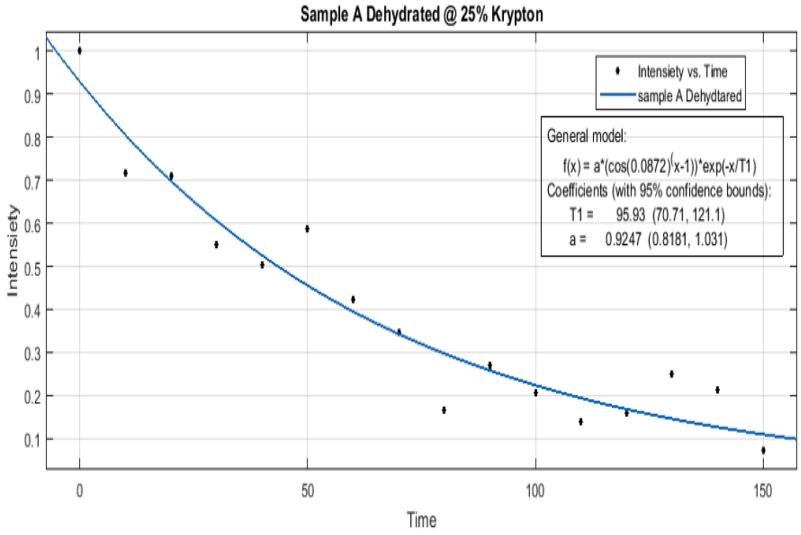


Figure 7.8: The signal Intensity as a function of time for Dehydrated sample A

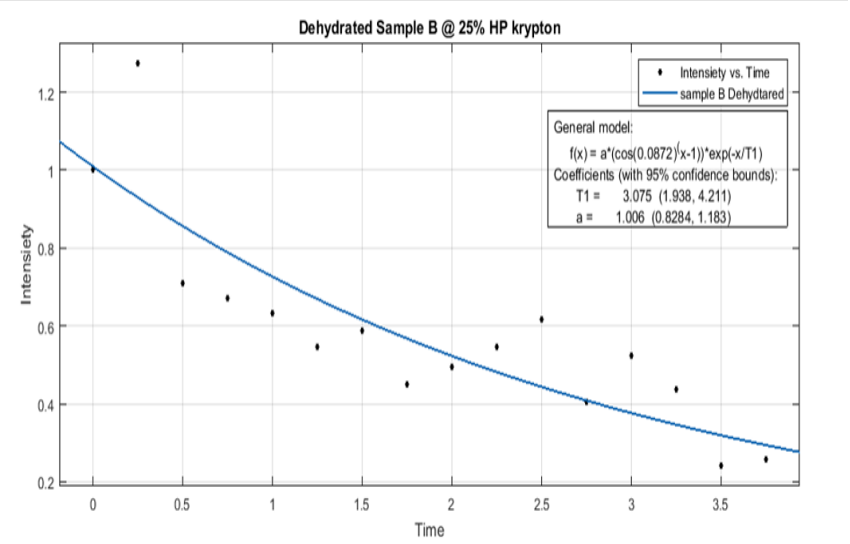


Figure 7.9: The signal Intensity as a function of time for Dehydrated sample B)

7.3.3 Oven Treatment

While the sample B is dried up using a vacuum oven at 50 °C, the oven sample was given different name to differentiate it from the other dehydrated sample (**oven** sample B is now known as **sample E**). While sample D dried up after rinsing it with glue, it is called now **sample F**.

Figure 7.12 shows the T_1 decay of 4.4 sec regime belong to the sample E which was dried by oven at 50 °C. That is very close to the T_1 value result from dehydrated sample B with 3 sec. The signal to noise in figure 7.12 of oven sample E is better than signal-to-noise in figure 7.9 of dehydrated sample B. This either due to pump cell becoming old or cause of mathematical issue arise from fitting software. However, the standard deviation in table 7.2

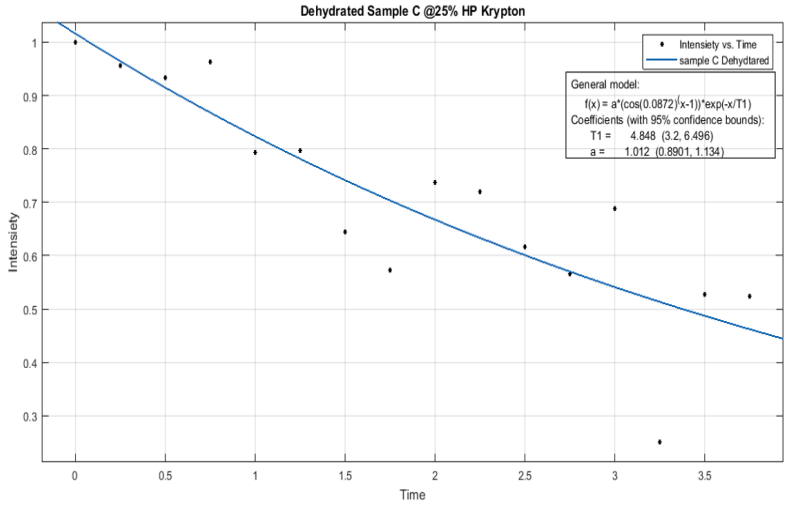


Figure 7.10: The signal Intensity as a function of time for Dehydrated sample C

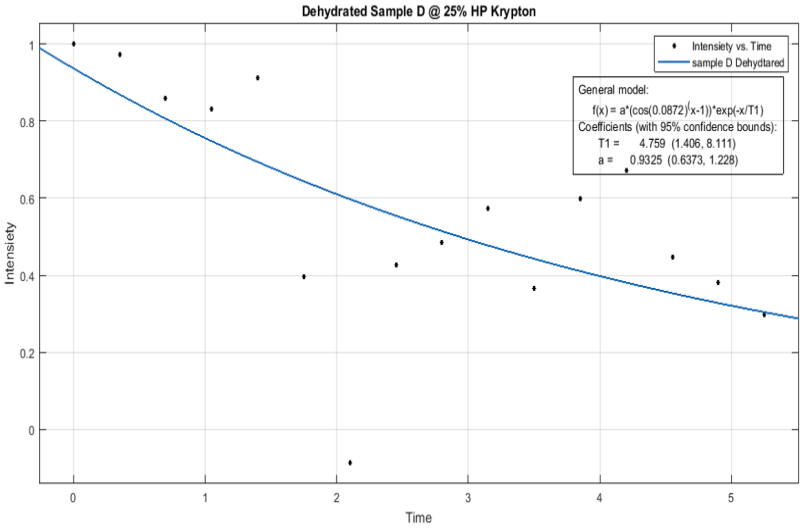


Figure 7.11: The signal Intensity as a function of time for Dehydrated sample D

gives more reliable data about the graphs signal-to-noise data because it was taken from the average T_1 data not from the one fitting data.

7.4 Discussion

7.4.1 Data Analysis

When comparing the T_1 value for the hydrated sample D to the hydrated sample F (sample D with glue) figure 7.13 shows a significant increase of 20 sec in the T_1 value from the original decay found with sample D of 9 sec. This is because of the foam of sample F was epoxy

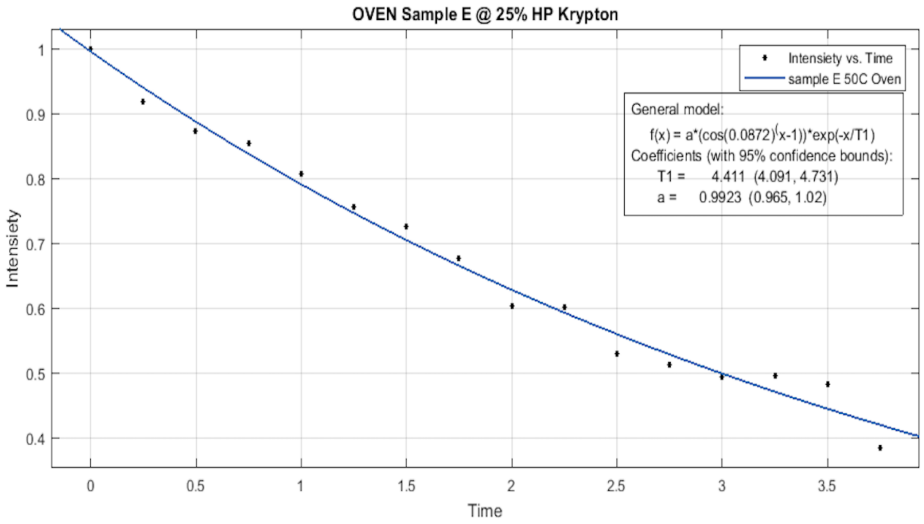


Figure 7.12: The signal Intensity as a function of time for **Oven sample E**

treated. As the glue coated the surface of the foam D, the surface of the foam became more solid and homogeneous than lower surface area which in turn makes the ^{83}Kr relaxation of hydrated sample F slower than ^{83}Kr relaxation of hydrated sample D observed in figure 7.7. If we finally consider comparing the T_1 value between the hydrated and dehydrated results

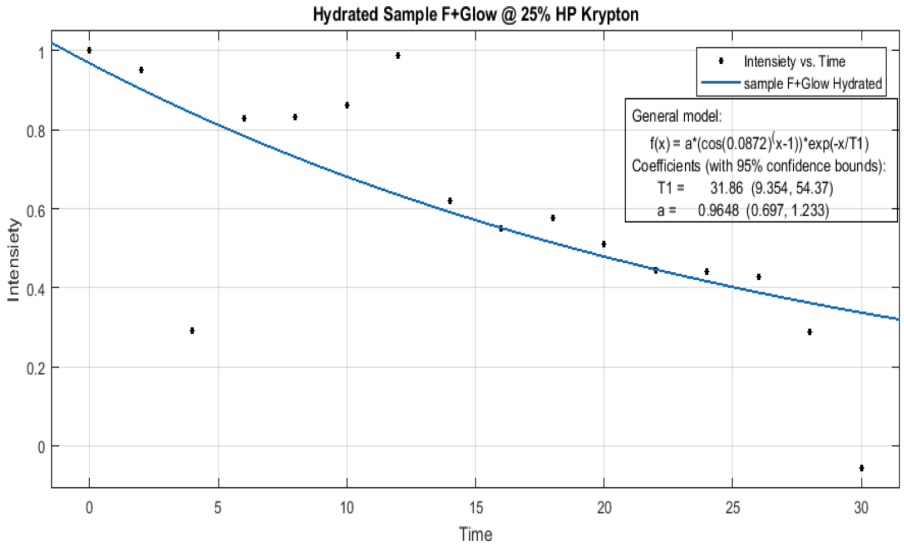


Figure 7.13: The signal Intensity as a function of time for **Hydrated sample F**

from sample A. Figure 7.8 shows that there is a significant 20 sec increase in the dehydrated sample over the hydrated sample A in figure 7.4.

Table 7.1 shows SEOP pressure inside the pump cell in mbar, delivery pressure in bar, and T_1 value in sec for all foam treatment process hydrated, dehydrated, epoxy treated (glued) to all samples.

In table 7.2, when looking at the average and standard deviation of T_1 results of the

Table 7.1: T_1 Value of Four Treated sample Using HP ^{83}Kr

sample	Hydrated sample			Dehydrated sample			Oven sample		
	SEOP (mbar)	Delivery (bar)	T_1 (sec)	SEOP (mbar)	Delivery (bar)	T_1 (sec)	SEOP (mbar)	Delivery (bar)	T_1 (sec)
A (empty)	1925	1.92	79.6	1983	2.01	59.9	NA	NA	NA
B (Medium) \E (Oven)	1935	1.93	7.1	1995	2.01	3.07	2037	2.06	4.41
C (Small)	1930	1.93	18.5	2010	2.01	4.84	NA	NA	NA
D (Large)	1937	1.93	9.4	2024	2.05	4.75	NA	NA	NA
F (Large+Glued)	1862	1.73	31.86	NA	NA	NA	NA	NA	NA

Table 7.2: The Average and Standard Deviation(SD) For Each Treated sample

sample	Hydrated sample		Dehydrated sample		Oven sample	
	Average (T_1)	SD	Average (T_1)	SD	Average (T_1)	SD
A (empty)	77.7	± 8.05	89.9	± 4.42	NA	NA
B (Medium) \E (Oven)	7.6	± 1.13	3.3	± 1.06	4.5	± 0.24
C (Small)	16.38	± 1.61	8.2	± 2.39	NA	NA
D (Large)	8.6	± 1.73	5.03	± 1.32	NA	NA
F (Large+Glued)	24.3	± 5.22	NA	NA	NA	NA

^{83}Kr gas relaxation measurements for four repeated experiments of four different types of surfaces (which have been explored by T_1 value of HP ^{83}Kr , namely hydrated, dehydrated, epoxi treated), we notice that this significant drop down in average T_1 relaxation range.

The Average and Standard Deviation (SD) of sample **A** with two different classified treatment of hydrated and dehydrated fall in the same 1.5 minutes' regime. This proves that there is no significant difference between the hydrated and dehydrated T_1 result explored in sample **A**. In contrast to sample **A** (empty), the results showed a major decrease in T_1, when low to high surface material is used in sample **B, C and D**. Moreover, the T_1 relaxation was decreased almost by half when theses samples dehydrated. In addition, the results prove that there is no significant difference between the T_1 result explored in hydrated sample **B & D**. Sample **D** is 3 times faster than sample **F** in relaxation. On the other hand, when observing the average and standard deviation of hydrated sample **D** and **F**, there is a significant change between epoxi (glue) treated and regular sample noticeable . If fast relaxation is required, for polarization measurement, epoxi treated data of sample **E** is more ideal. In addition, epoxi treated sample would be an ideal choice for phantom design.

7.4.2 Data Reliability

The SEOP delivery pressure was monitored to make sure that the collected data from the Kea were acquired at the same behaviour of SEOP inside the pump cell. This will confirm that SEOP was stable inside the pump cell every time the HP ^{83}Kr is delivered to the detection cell. Collected data were analysed using Igor Pro 7 Software (Version 7, Lake Oswego, Oregon 97035, USA). By analysing the delivery pressure of all sample collected over time. The following figure 7.14 shows stability of the measurements which were collected during the experiment for all samples.

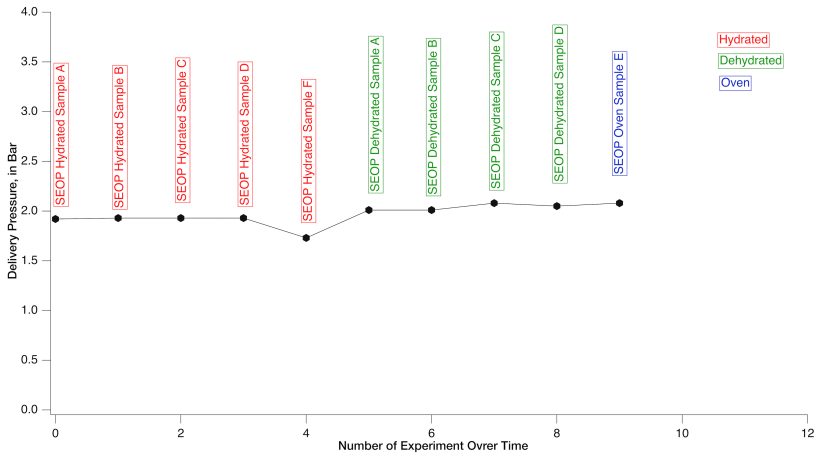


Figure 7.14: SEOP Measurements Stability Overtime

7.5 Conclusion

In summary, figure 7.15 shows that there is no significant change between hydrated and dehydrated sample A (i.e empty). However, sample C shows a quite variety of differentiation in T_1 data collected between hydrated and dehydrated material. This makes sample B, C, and F are the ideal selection for phantom design for clinical scanners.

In addition, figure 7.15 sample bars prove the effect of the foam property size, temperature, and hydration on the data measurement where hyperpolarisation of T_1 relaxation is significantly decreased when relaxing agent is used either in hydrated, dehydrated or oven sample is used.

Figure 7.16 shows a schematic diagram of phantom design that contain the ideal choice foam material and type (B, C, and F) which could be used at any in vivo clinical scanner to

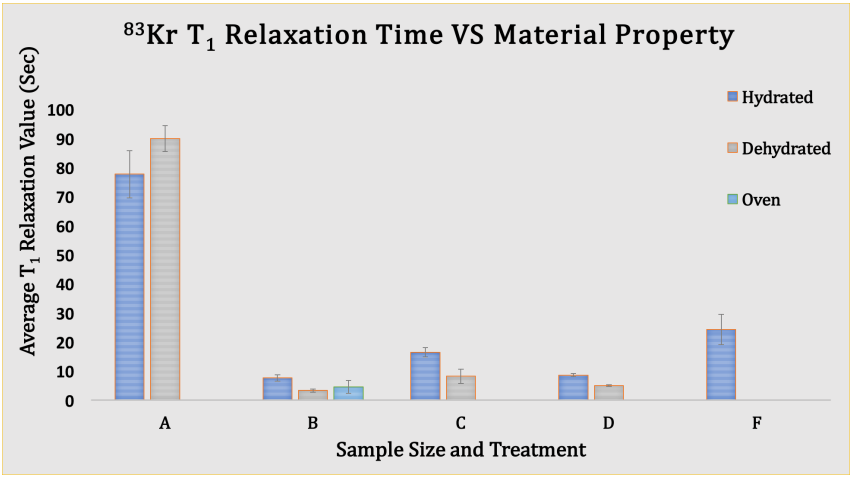


Figure 7.15: Analysis of Average T_1 Data Collected for HP ^{83}Kr of sample Materials

study ^{83}Kr relaxation measurement and behaviour prior to an excised lung imaging.

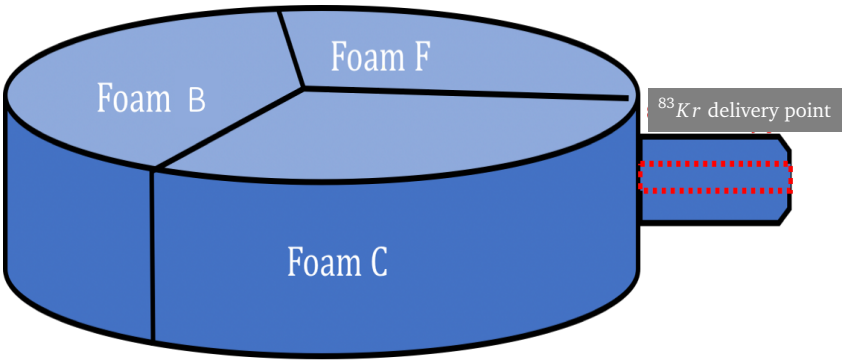


Figure 7.16: Schematic Diagram of Phantom Design for In vivo Clinical Scanner

CHAPTER 8

REMOTE DETECTION OF HP ^{83}KR GAS

8.1 Introduction

Magnetic Resonance Imaging (MRI) with hyperpolarised (HP) krypton-83 (^{83}Kr) has become available for the first time. The relaxation of the nuclear spin of ^{83}Kr nuclei (I = 9/2) is driven by quadrupolar interactions during brief adsorption periods on surrounding material interfaces. Experiments in re-compression system unit reveal that the polarization level of HP ^{83}Kr gas strongly depends on storage condition. The T_1 relaxation of HP ^{83}Kr allows for the determination of how long hyperpolarised ^{83}Kr could remain useful. The feasibility of hyperpolarised ^{83}Kr MRI is tested in a re-compression unit by using krypton gas with natural abundance isotopic distribution. Additionally, the influence of time where hyperpolarised ^{83}Kr gas density stored in re-compression unit close to magnetic field strength are investigated. With the prospect of HP^{83}Kr being used clinically, ideas on how it will be stored and transported have been explored. The affect of superconducting magnetic fringe field on ^{83}Kr T_1 relaxation times has been measured. A re-compression system has been designed and utilized to store the noble gas for up to 3 min in different magnetic field strengths. Results show that polarisation depletes substantially when placed at lower magnetic field strengths and 100 Gauss (10 mT) appears to be the optimum field for the gas yielding T_1 values ranging from 73.3 sec to 13 sec.

Hyperpolarisation of MRI tracer substances increases the MR signal by 3 to 5 orders of magnitude and various MRI protocols have been developed with hyperpolarised noble gases to probe different structural and functional aspects of lungs in healthy and diseased subject. The advancement of this technique is a quest for better imaging resolution but also for novel sources of contrast that inspect different aspects of lung function (Pavlovskaya et al., 2005; Lilburn et al., 2015, 2013).

HP krypton-83 (^{83}Kr), is being developed at SPMIC in Nottingham as a new MRI modality that is sensitive to the surface-to-volume (S/V) changes in an animal model of emphysema (Rogers et al., 2016). In addition, to make this new contrast agent work, the gas needs to be hyperpolarised through laser pumping, stored, and transported to the scanner for inhalation by the patient. Therefore, the ^{83}Kr relaxation (or depolarization) behaviour has been explored in detail under various conditions to improve the relevant MRI protocols.

8.2 Material and Method

8.2.1 ^{83}Kr Optical Pumping

In the past, scientists have explored alkali metal vapour optical pumping of quadrupolar noble gas nuclei, such as ^{83}Kr. The SEOP experimental set-up used here is similar to the one reported previously in the literature for the production of hp ^{129}Xe (I = 1/2) (Meersmann and Brunner, 2015; MEERSMANN and PAVLOVSKAYA, 2015; Schaefer et al., 1990; Grover, 1978).

The gas mixture type II used for all experiments of a high concentration of natural abundance krypton [mentioned previously in chapter 5 section 5.6] (typically 25% and about 75% of molecular N_2). Note, that N_2 is added for radiation quenching purposes as in ^{129}Xe SEOP. The pumping cell gas pressure was in the range of 1.0 bar to 2.5 bar. Pumping with high noble gas density is found to be vital for obtaining the highest signal intensities with HP ^{83}Kr. Unlike HP ^{129}Xe freezing for storage method is not suitable for HP ^{83}Kr. The freezing will cause quadrupolar relaxation, which in turn will destroy the HP ^{83}Kr polarisation (Mortuza et al., 2003).

In figure 5.12, The HP ^{83}Kr polarization at 2.5 bar was 5% for 25% ^{83}Kr and 75% N_2

mixture. When a 30 W continuous wave diode array solid-state laser (24 W after optics) is applied to the pump cell of stopped flow process, this lead to a signal enhancement of $\frac{5\%}{4.52\times10^{-4}\%}$ close to 11060 times greater than the ^{83}Kr thermal polarization (i.e $P_{Thermal} = 4.52 \times 10^{-4}\%$) at 9.4 T and 20 °C (≈ 300 K) (Horton-Garcia et al., 2005).

A gas mixture of 25% Krypton and 75% Nitrogen is used for pumping within a pump cell (length = 125 mm, I.D. = 25 mm) that contains 1 g of rubidium. The temperature of the pump cell is kept between 150 °C and 160 °C, a pumping cell temperature that is about 10 °C to 20 °C higher than the temperature typically used for HP ^{129}Xe. In the stopped flow experiments the samples are evacuated to 0.0001 bar and the gas mixture is exposed to laser radiation inside the pump cell for 6 min. Subsequently, the optically pumped krypton is transferred using pressure equalization into the samples where a delivered HP krypton gas pressure range of 1 – 2 bar is maintained.

8.2.2 NMR Measurements

Experiments were performed using 30 mm in diameter RF coil (probe) that resonate at low resonance frequency of 15.4 MHz with a KEA software (Magritek, Malvern, USA) a Magretek spectrometer linked to computer and a 9.4 T Oxford wide-bore (89 mm) superconducting magnet. Manually phased integrated values from optical pumping data are calculated using Prospa software. The calculated data of ^{83}Kr gas was Fourier transformed to spectrum as a function of time. Pulse and collected experiment used an amplitude of ≈ 190-200 μs as RF power to be equivalent to 90° flip angle and the with HP ^{83}Kr gas storage time interval was incremented every 30 sec inside re-compression unit.

8.2.3 Re-compression System Design & Preparation

The re-compression unit is a device used to store shuttled hyperpolarised noble gas and then transfer it to the sample as a part of delivery system. It is also used to boost ^{83}Kr spin polarization of below ambient pressure SEOP. This unit was manufactured for two prominent purposes: first, to extracted the hyperpolarised gas from the SEOP cell and second, to deliver the gas for pulmonary imaging in a single expansion–compression cycle. This re-compression unit was designed by Hughes-Riley et al. (2013) to store the hyperpolarised gas.

The compression system requires a high concentration of noble gas to function properly. This also allows for cryogenic separation. It functions properly with low pressure of SEOP and using stopped flow method which allows a complete cycle of extraction and compression at the same time to occur. Because capacity (volume) of the re-compression unit is bigger than the pump cell capacity, shuttled hyperpolarised gas will lose it is polarisation if it stayed in the re-compression cylinder for a long time. For this reason, the re-compression cylinder is surrounded by Helmholtz coils to provide longer survival storage time for hyperpolarised spins.

Figure 8.1 shows the re-compression system which consists of a cylindrical acrylic tube, inside the tube there is a piston that separates the cylinder into two main chambers. One chamber is for storing the hyperpolarised (HP) gas and the other is for the external nitrogen (N_2) to compress HP gas via the piston. The external (N_2) and vacuum pump are used to control the piston movement in and out while valve **V** is used to control the gas flow in and out.

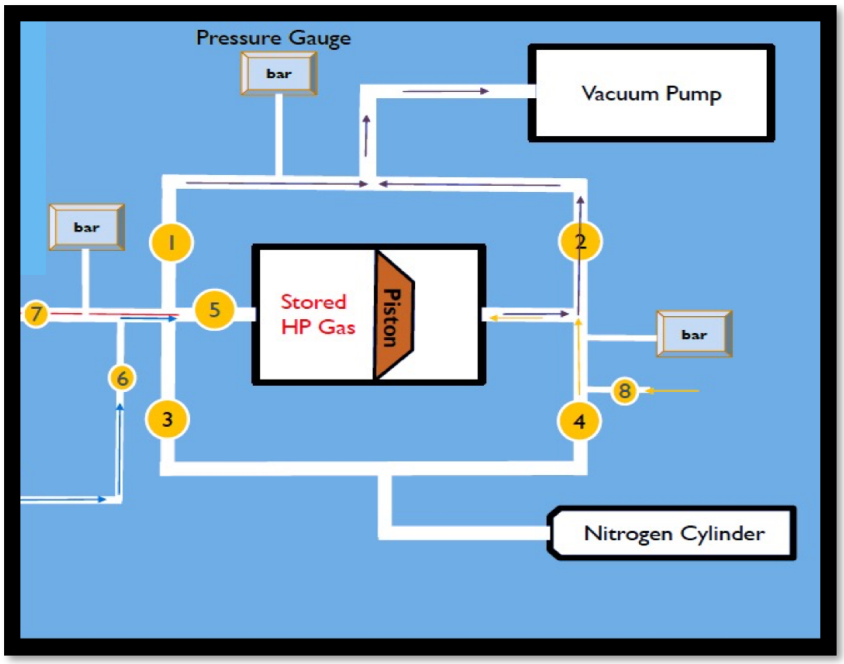


Figure 8.1: a Schematic Diagram of Re-compression System Design

8.2.4 Experimental Set-Up and Transfer of HP ^{83}Kr

SEOP of the Krypton was achieved in batch mode. The polarization was left to build up for 5 minutes in the cell before being sent for detection. Research grade krypton was used. The gas

mixture used was type II (25% of ^{83}Kr, with blue dimaond ($\diamond$), with 75% of N_2)[mentioned previously in chapter 5, subsection 5.9] and SEOP cell pressure was maintained at around 2 ± 0.2 bar achieving a polarisation of just 5%. The cell was made from Pyrex (borosilicate) cylindrical glass with Pyrex transfer tubes attached. Two Chem-cap valves were fastened at the top of the cell to ensure leakage of air that may react with the ^{83}Kr gas. However, the valves were opened during the experiment. The temperature of the cell was kept at 433 K using a heat-gun. Two thermocouples were attached to the Pyrex cell to monitor the cell temperature. This is seen in figure 8.2.

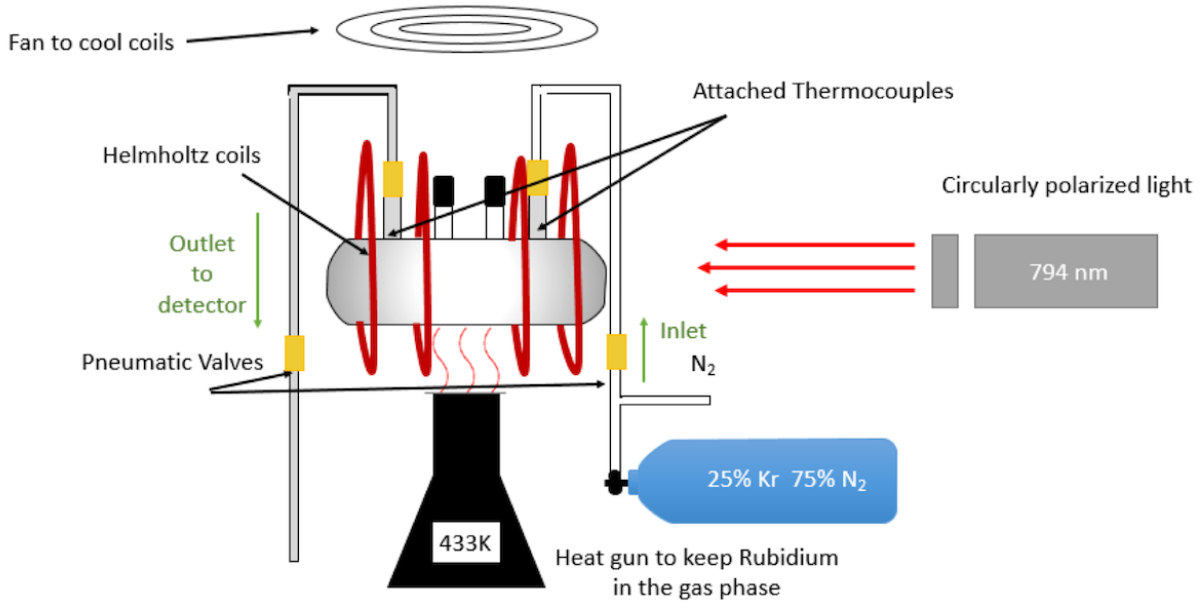


Figure 8.2: a Schematic Diagram show Inside Hyperpolarizing Unit.

Circularly polarized laser light from a 24 W laser was tuned to the D_1 transition of wave length = **794.7** nm and was directed at the pump cell by powering it to 2.3 V and 46.2 A. Two sets of Helmholtz coils powered to 10.15 A and 48.4 V to generate a magnetic field parallel with the propagation of the laser beam to initiate the angular momentum transfer between the photons and Rubidium electrons. A fan was kept on throughout the experiment to prevent the coils from overheating.

The inflow and outflow of gases inside the cell was controlled by pneumatic valves. The re-compression unit had a volume of 2 L and contained a plastic divider to separate air used for compression from the HP gas. Experiments were carried out in an Oxford superconducting 9.4 T with probe tuned to the resonance frequency of 15.4 MHz for the ^{83}Kr.

From figure 8.1, the storing chamber needs to be evacuated from stored gas before using

the re-compression unit. This usually is achieved manually by opening valves **1, 2** and **5**, while closing the others. The gas chamber is usually prepared to accommodate HP ^{83}Kr by opening valve **5** and **6** while closing other the valves. The hyperpolarised gas is then shuttled into the chamber from the pump cell. These two valves allow the HP ^{83}Kr gas to enter the stored HP gas chamber.

The HP ^{83}Kr gas was left inside this chamber for incremented (30 sec) delayed time by closing valve **5**. When valve **6** is closed and **1** is opened, the residual hyperpolarised gas left inside the pipes is then evacuated into vacuum pump. After the hyperpolarised gas is evacuated, valve **7** is opened while valve **1** is closed. This action followed by compressing the gas to the required atmospheric pressure by opening valve **8**. The valve **8** is then closed and valve **5** is opened to push the pressurized hyperpolarised gas via pipe to reach the glass container inside the RF coil. For detection, the pressure gauge located after valve **8** measures the pressure before the gas is compressed, while the pressure gauge located between valve **6** and **7** measures the atmospheric pressure after the gas is compressed.

The re-compression unit was placed inside the fringe field of the Oxford 9.4T superconducting magnet at 5 G, 10 G, 50 G, 100 G and 500 G. These values were measured using a **Gauss meter** which is shown in figure 8.3. The instrument was held at 4 points around the edge of re-compression unit nearest the magnet. These values were used to predict the averaged magnetic field strength. The standard deviation was then calculated for each reading giving an error of approximately 10% of required value.



Figure 8.3: Gauss Meter.

At each fringe field strength the gas was kept in the re-compression unit from 60 sec to 3 min increasing in increments of 30 sec. Four readings were taken for each storage time. As

shown in figure 8.4, the re-compression system was reoriented by 90° and readings for each field strength was measured again.

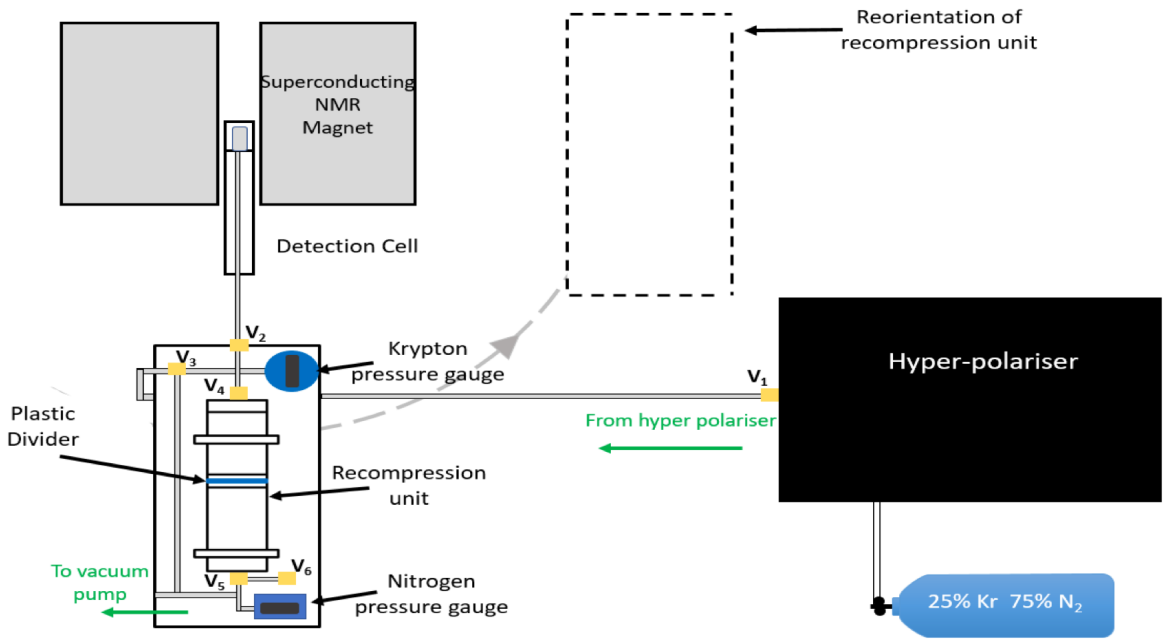


Figure 8.4: Schematic diagram of experimental set up. Recompression system was placed on a table with vaccuum pump underneath to aid with evacuating the system.

8.3 T_1 Calculation

8.3.1 Data Analysis

Data was acquired and processed through the PROSPA software package which conducted a simple NMR pulse sequence. A 90° RF pulse was applied and 1D plot was produced. This was manually phased to adjust the zero and first order phase parameters to display the maximum signal. Initially the spectrum was integrated using the integration PROSPA command, the values for repeat measurements were calculated according to the **Peak Height** Method.

In figure 8.5 the first 3 points from the real data of the free induction decay (FID) were summed and averaged giving the value for the peak intensity. For each experiment the nitrogen pressure and the pressure at which ^{83}Kr entered the detection cell were also taken for each 1D pulse plot.

After determining the peak intensity for each of the four measurements at each delivery storage time, these values were divided by the ^{83}Kr pressure and normalized. The results

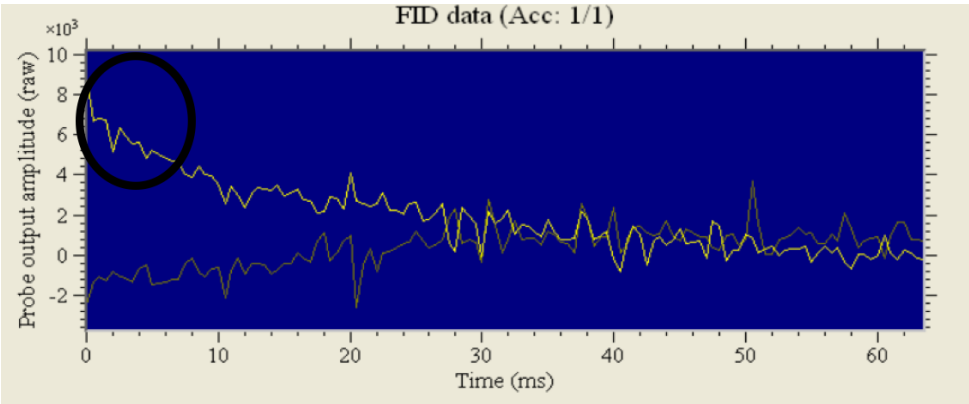


Figure 8.5: 1D Plot for Peak hieght Method FID

were then plotted against delivery storage time and T_1 was calculated using

$$S_{(t)} = A.\exp^{-t/T_1} \tag{8.1}$$

where A is a pre-exponential fitting parameter.

Table 8.1 shows the average of acquired signals which were normalised later to give the normalised signal for the 1D plot acquired at 50G, while figure 8.6 shows the fitting curve produced to generate the T_1 value. This method was applied to all Free Induction Decays (FID's) produced by all experiments of different fringe field strength [5 G, 10 G, 50 G (parallel and perpendicular to the stray field of the super conducting magnet), 100 G (parallel and perpendicular to the stray field of the super conducting magnet), 250 G and 500 G].

Table 8.1: The Normalised Signal of 1D decay from 50 Gauss Re-compression Experiment of Peak Height Method

Average Signal Intensity	Normalised Signal Intensity	Time (sec)
16141785.96	1	20
8787148.19	0.54	80
6814046.57	0.42	110
3536682.04	0.21	140
3241057.21	0.20	170
1970674.43	0.12	200
0	0	260

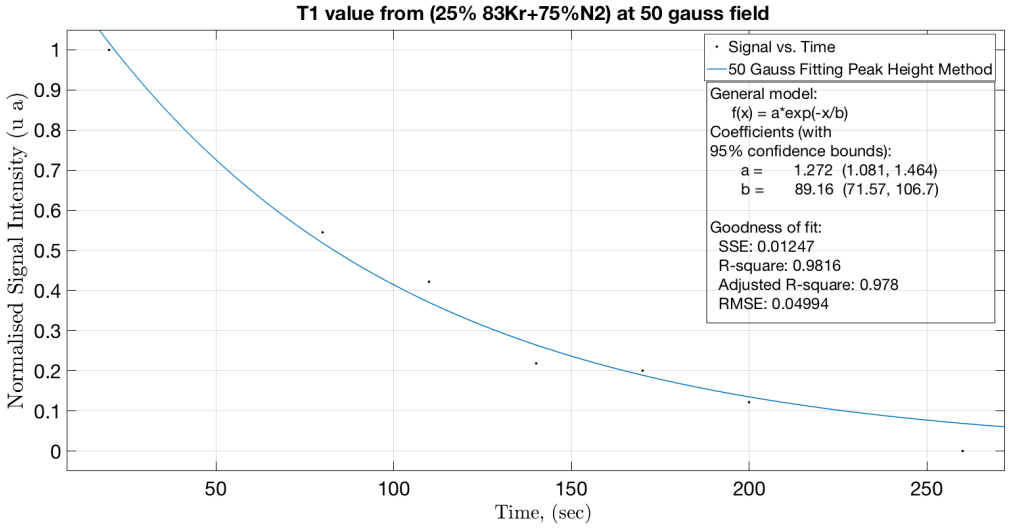


Figure 8.6: The T_1 Value from 1D spectrum 50 G after Normalised Signal fitted

8.3.2 Justification and Data Reliability

Furthermore, on top of the peak height signal intensity calculation, the **integration** method was also used to integrate the area under the peak to verify the generated result from the peak height method which is shown in figure 8.7. Table 8.2 shows the normalised signal from the integration method while the figure 8.8 shows the T1 value from plotted curve fit used by equation 8.2.

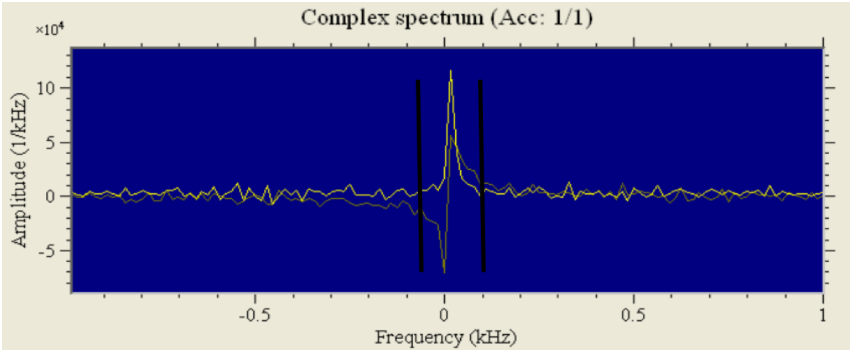


Figure 8.7: 1D spectrum Shows Integration Method

In addition, SEOP stability was calculated to make sure that the data acquired from each 1D spectrum are having the same condition from the SEOP cell. Thus a control signals were measured during each field experiment to check pump cell stability. This signal is measured directly from the detection cell without storing it inside the re-compression system where it is normalised with the pressure inside the pump cell. Figure 8.9 shows the signal stability from the pump cell during the experiment.

Table 8.2: The Normalised Signal of 1D spectrum from 50 Gauss Recompression Experiment of Integration Method

Average Signal Intensity	Normalised Signal Intensity	Time (sec)
6901.08	1	20
3795.36	0.54	80
2924.21	0.42	110
1423.89	0.20	140
1152.56	0.16	170
613.81	0.08	200
0	0	260

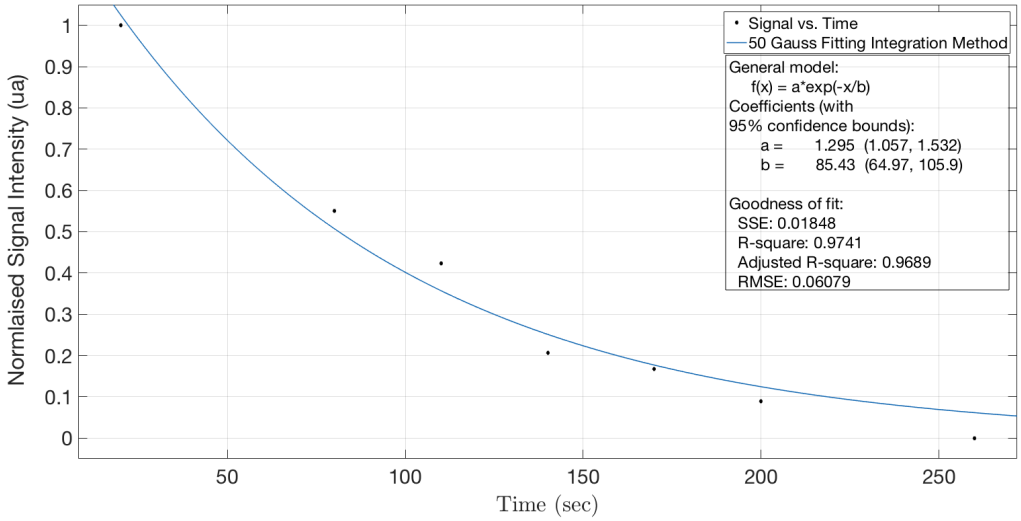


Figure 8.8: The T_1 Value from 1D spectrum 50 G after Normalised Signal fitted

8.4 Results

The normalised signal data from 50 G 1D spectrum was plotted using a custom exponential curve fit using Matlab software equation

$$y = a.\exp^{-x/b} \tag{8.2}$$

Table 8.3: T_1 Value generated from Peak Height and Spectrum Integration of 1D plot from ^{83}Kr Recompression Experiment

FIELD STRENGTH	Peak Height Method				Spectrum Integration Method			
	T_1	$T_{(low)}$	$T_{(up)}$	STD	T_1	$T_{(low)}$	$T_{(up)}$	STD
5 G	ϕ	ϕ	ϕ	ϕ	16.3	12.4	47.3	19.1
10 G	66.1	31.5	100.7	34.6	59	85.4	198	75.2
50 G	89.1	72.8	105.4	16.3	85.4	64.9	105.9	19.1
50 G with 90 phase shift	83.5	71.4	95.7	12.13	87.6	68.4	106.9	19.2
100 G	98.8	64.5	133.8	34.4	81.4	52.92	90.5	19.6
100 G with 90 phase shift	127	69.5	185.8	58.1	81.5	22.5	140.5	58.9
250 G	92	84.2	99.7	7.7	97.3	87.5	107.2	9.8
500 G	68.8	41.8	95.8	26.9	81	65.1	103.1	19.1

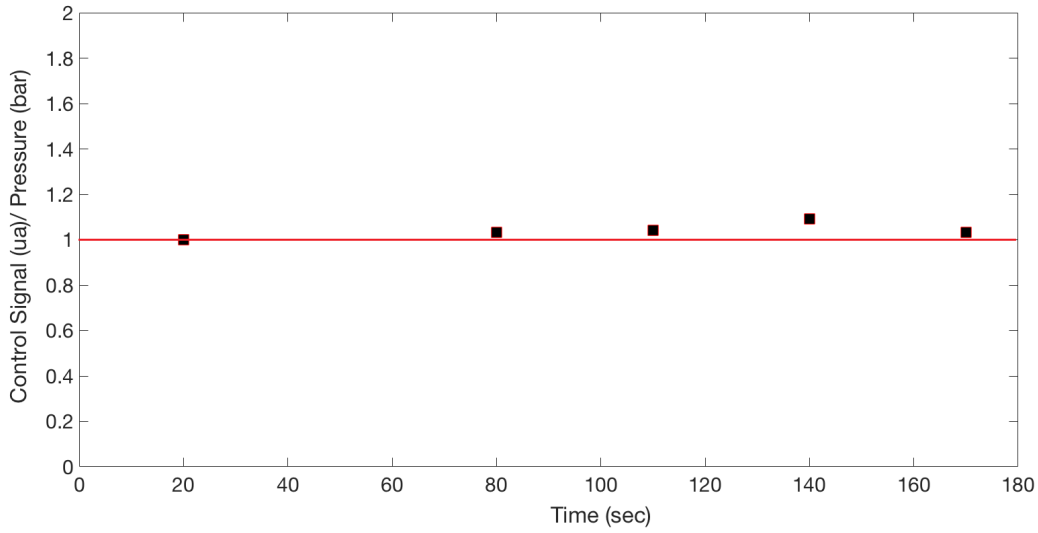


Figure 8.9: Pump cell Stability

8.5 Discussion

The Table 8.3 show all the T_1 values generated from both methods. T_1 value for field strength 50 G is roughly the same even if the orientation is changed and also have the same standard deviation. While 100 G field shows the same T_1 value in both orientations when integration method used, however the 90° shift orientation (perpendicular) showed a high standard deviation of 58% compared to 19% of parallel 100 G field. Thus, the 90° shift orientation was excluded from the discussion. The author still recommends further investigation for this field strength to see whether the standard deviation could be improved.

Overall, the T_1 value remained similar for all investigated field strength with a slight increase in the 250 G and a slight decrease in the 10 G. Therefore, to demonstrate the difference between the results gathered from different field strength, the data were analysed to express the difference between each magnetic field strength using MATLAB.

In the bar chart of figure 8.10, the **integration** method showed that 250 G has the longest T_1 value while 10 G is the shortest. Leaving 500 and 100 G are having the same T_1 value. The 50 G showed a T_1 value that falls between 250 G and the 100 G. While in the same chart, The **Peak Height** method showed the same pattern in T_1 relaxation except this time the field strength of 100 G was the longest. Although the aim from experiment is to demonstrate what field strength represent the longest T_1 value which is 250 G. However, The author believes that 50 G is the most suitable field strength because 50 G is easily achievable is Helmholtz

coils while 250 and 500 G require cooling devices. The 500 G showed a decrease in T_1 value while it supposed to show an increase of T_1 value, this is because as the field strength in the fringe field increase the variation increase as well.

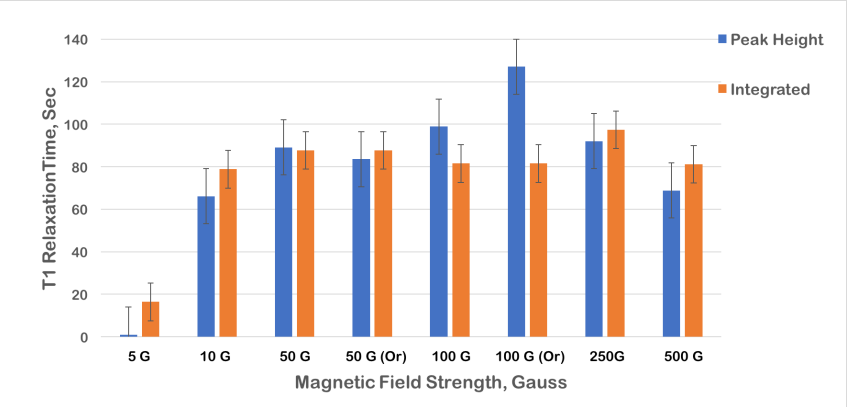


Figure 8.10: T_1 value versus fringe field of 9.4 T magnet

8.6 Conclusion

Storing hyperpolarised ^{83}Kr at different magnetic fringe field strength by using a re-compression unit shows that there is a dependency of the polarization on these field strength value which were used to determine T_1 relaxation times ranging from (59-66 ± 34) to (97-127 ± 19.2). Also, there is a direct relationship between the fringe field existence and the survival HP ^{83}Kr gas relaxation inside the re-compression system. While the results showed field dependency, the ideal field coil to surround the re-compression system is 50 G by using Helmholtz coil. This is because low building cost and easy accessibility to this design. Moving to a higher field Helmholtz coil would be costly and require cooling system with no additional benefit in the T_1 value.

CHAPTER 9

FUTURE WORK

Lungs are difficult to image, when conventional magnetic resonance imaging is used because of the presence of air in the lungs. Atmospheric air can not be detected by imaging when magnetic resonance technique is used, for chemical and physical reasons, as discussed in earlier chapters.

In this thesis the author has discussed the basic principles for developing the technical methods of a magnetic resonance imaging system to detect chest diseases. The use of this technique of "hyperpolarisation" will open the doors for the possibility of imaging this human organ using magnetic resonance imaging. On the other hand, this technique is one of the medical laser applications. This technique of Spin Exchange Optical Pumping is novel. The future MRI procedures may depend on this technique.

It can not be absolutely determined that this technology will be available for human applications. To enable this technique to become applicable there are several stages that need to be discussed, researched and examined. Colleagues and students will be thankful to complete the research and study these gaps after me.

One of these gaps is the development and modification of the "hyperpolarisation" device so that it can be moved from its current position inside the laboratory to the clinical magnetic resonance zones. The other is to study and investigate the T1 thermal polarisation of ^{83}Kr and ^{129}Xe inside the high magnetic field 3T and 7T magnets. A phantom must be designed to

accommodate different foam sizes. Moreover, a study to investigate the T1 value behaviour of hyperpolarised ^{83}Kr and ^{129}Xe when has come in contact with these different type of surfaces in a 7T clinical magnet. Another practical investigation is to design an RF coil to accommodate the ^{83}Kr phantom that resonates at 11.543 MHz when placed inside 7T clinical magnet bore. Also, a design of an RF probe to accommodate a lung is recommended.

Also, another investigation is required to probe the effect of the size of the alveoli on the image contrast of ^{83}Kr and ^{129}Xe. Further clinical investigation is required using an excised lung to observe how sensitive the ^{83}Kr inside the lung at 7T clinical scanner by addressing T1 behaviour. In addition to the previous gaps, the study of the toxicity of hyperpolarised ^{83}Kr for human subjected is an extreme demand before moving to human subjects experiment. Furthermore, a study to address the workflow inside the magnetic resonance imaging zone to worker and patient and noble gas transportation is needed.

Finally, to study the most practical method to deliver the hyperpolarised noble gas to human patient with minimum depolarisation is another stage of investigation which is required. As you can see moving to clinical application to hyperpolarised noble gas is not an easy process and will require a number of studies. However, It is possible to make this technique clinically applicable.

CHAPTER 10

CONCLUSION

Here I will summarise and conclude the data and information gathered from all previously discussed experiments. Hyperpolarised ^{83}Kr is a promising new biomarker for Pulmonary MRI. The noble gas is capable of providing surface sensitive contrast. Recent methodological advances in Spin Exchange Optical Pumping (SEOP) have produced signal intensities for HP noble gases that are increased by orders of magnitude over thermal polarization. This work reports the study of relaxation experienced by the hyperpolarised (HP) noble gas isotope ^{83}Kr in contact with surfaces. The spin-lattice relaxation of ^{83}Kr is found to depend strongly on the chemical composition of the surfaces in the vicinity of the gas. This effect is caused by quadrupolar interactions during brief periods of surface adsorption that are the dominating source of longitudinal spin relaxation in the ^{83}Kr atoms. A simple model made from different type of foam, with uniform but variable sizes was used for the relaxation measurements. The observed T_1 relaxation rates also depend strongly on the chemical treatment of the foam surfaces and on the surface to volume ratio. Hyperpolarised Krypton under conditions of stopped flow allows for the acquisition of ^{83}Kr NMR spectra that can be used to characterize a variety of materials. By using the improved methodology for SEOP of isotopically hyperpolarised ^{83}Kr, internal surface behaviour details of ex vivo foam were resolved with hyperpolarised ^{83}Kr spectra after hyperpolarised ^{83}Kr delivery to the detection cell. Different HP ^{83}Kr relaxation times were found between the different type

of foams and their sizes in ex vivo. The T_1 relaxation rate of hyperpolarised ^{83}Kr provided a demonstration of surface quadrupolar relaxation sensitivity. The low signal intensity of thermally polarised ^{83}Kr remains a problem for probing small volume-to-surface material due to low ^{83}Kr loading and increased T_1 relaxation times in large surface-to-volume materials with values ranging from seconds to many tens of seconds. However, experiments with small volume surface material have become attainable and practicable because of optical pumping development of laser applications that lead to the production of hyperpolarised (hp) ^{83}Kr for NMR and MRI applications.

In hydrated treatment, There is a significant decrease in T_1 value of the ^{83}Kr when a small surface to volume sample is used as a relaxing agent. This shows the strong effect of the relaxation agent (foam) upon T_1 relaxation. There is no fundamental or significant difference between the T_1 value from hydrated samples with large and medium surface foams. **In a dehydrated treatment**, there is a significant decrease in the T_1 value of the HP ^{83}Kr when a medium surface to volume sample were used. Noticeably, there is no significant change in T_1 value of the HP ^{83}Kr when large and small surface to volume were used. **After oven treatment**, samples showed similar T_1 value results when compared with medium and large surface to volume dehydrated samples. Also, here samples recorded half the T_1 value when compared with large surface to volume dehydrated sample and quarter the value recorded from small surface to volume hydrated sample. **In epoxy treatment**, the sample showed an increase of T_1 value when compared with all sizes of hydrated, and dehydrated samples. it also showed a decrease of one third of T_1 value from the empty hydrated and dehydrated sample.

Storage of hyperpolarised krypton was investigated at different magnetic fringe fields. The T_1 values generated from both peak height and integration methods showed similar results. Overall, the T_1 value remained similar for all investigated field strengths with a slight increase in at 250 G and a slight decrease at 10 G. Therefore, to demonstrate the difference between the results gathered from different field strengths, the data were analysed to express the difference between each magnetic field strength. The integration method showed that 250 G has the longest T_1 value while 10 G is the shortest. 500 and 100 G have the same T_1 value. 50 G showed a T_1 value that falls between 250 G and the 100 G. The 50 G is the most

suitable field strength because 50 G is easily achievable using Helmholtz coils while 250 and 500 G require coil cooling device. Storing hyperpolarised 83Kr at different magnetic fringe field strength by using a re-compression unit shows that there is a dependency of the polarization on these field strength value which were used to determine T_1 relaxation times ranging from (59-66 ± 34) to (97-127 ± 19.2). Also, there is a direct relationship between the fringe field existence and HP ^{83}Kr gas relaxation inside the re-compression system. While the results showed field dependency, the ideal field coil to surround the re-compression system is 50 G by using Helmholtz coil. This is because low building cost and easy accessibility to this design. Moving to a higher field Helmholtz coil would be costly and require cooling system with no additional benefit in the T_1 value.

BIBLIOGRAPHY

Abatzoglou, N., Dalai, A., Gitzhofer, F., Markatos, N., Stamou, A., Beltrao, J. et al. (2007), Green diesel from fischer-tropsch synthesis: Challenges and hurdles, *in* 'Proc. of the 3rd IASME/WSEAS Int. Conf. on Energy, Environment, Ecosystems and Sustainable Development, Agios Nikolaos, Greece', citepseer, pp. 223–232.

Albert, Cates, Driehuys, Happer, Saam, Springer and Wishnia (1994), 'Biological magnetic resonance imaging using laser-polarized 129Xe.'.

Albert, M. S. and Hane, F. T. (2016), *Hyperpolarized and inert gas MRI: From technology to application in research and medicine*, Academic Press.

Barskiy, D., Coffey, A., Nikolaou, P., Mikhaylov, D., Goodson, B., Branca, R., Lu, G., Shapiro, M., Telkki, V.-V., Zhivonitko, V. et al. (2017), 'Nmr hyperpolarization techniques of gases', *Chemistry-A European Journal* **23**(4), 725–751.

Basdevant, J.-L., Rich, J. and Spiro, M. (2005), *Fundamentals in nuclear physics: From nuclear structure to cosmology*, Springer Science & Business Media.

Bernstein, M. A., King, K. F. and Zhou, X. J. (2004), *Handbook of MRI pulse sequences*, Elsevier.

Birchall, J., Whiting, N., Skinner, J., Barlow, M. J. and Goodson, B. M. (2017), Using raman spectroscopy to improve hyperpolarized noble gas production for clinical lung imaging techniques, *in* 'Raman Spectroscopy and Applications', InTech.

Bloembergen, N., Purcell, E. M. and Pound, R. V. (1990), Relaxation effects in nuclear magnetic resonance absorption, *in* 'Resonances', World Scientific, pp. 411–444.

Bouchiat, C., Bouchiat, M. and Pottier, L. (1969), 'Evidence for rb-rare-gas molecules from the relaxation of polarized rb atoms in a rare gas. theory', *Physical Review* **181**(1), 144.

Bouchiat, M., Brossel, J. and Pottier, L. (1972), 'Evidence for rb-rare-gas molecules from the relaxation of polarized rb atoms in a rare gas. experimental results', *The Journal of Chemical Physics* **56**(7), 3703–3714.

Brant-Zawadzki, M., Gillan, G. D. and Nitz, W. R. (1992), 'Mp rage: a three-dimensional, t1-weighted, gradient-echo sequence–initial experience in the brain.', *Radiology* **182**(3), 769–775.

Brenner, D. and Hall, E. (2007), 'Computed tomography—an increasing source of radiation exposure', *New England Journal of Medicine* **357**(22), 2277–2284.

Brinkmann, D. and Kuhn, D. (1980), 'Nuclear magnetic relaxation of kr 83 in krypton gas', *Physical Review A* **21**(1), 163.

Callaghan, P. T. (1993), *Principles of nuclear magnetic resonance microscopy*, Oxford University Press on Demand.

Carr, H. Y. and Purcell, E. M. (1954), 'Effects of diffusion on free precession in nuclear magnetic resonance experiments', *Physical review* **94**(3), 630.

Cherry, S., Sorenson, J. and Phelps, M. (2012), *Physics in nuclear medicine e-Book*, Elsevier Health Sciences.

Childs, W., Cok, D. and Goodman, L. (1982), 'Hyperfine structure of the x/sup 2/. sigma./sup+/ground state of ca/sup 35/cl and ca/sup 37/cl by molecular-beam, laser-rf double resonance', *J. Chem. Phys.;(United States)* **76**(8).

Cleveland, Z. I., Stupic, K. F., Pavlovskaya, G. E., Repine, J. E., Wooten, J. B. and Meersmann, T. (2007), 'Hyperpolarized 83kr and 129xe nmr relaxation measurements of hydrated surfaces: implications for materials science and pulmonary diagnostics', *Journal of the American Chemical Society* **129**(6), 1784–1792.

Cockburn, M. (2003), 'Mri from picture to proton', *Imaging & Therapy Practice* p. S13.

Cowgill, D. F. and Norberg, R. E. (1973), 'Spin-lattice relaxation and chemical shift of kr 83 in solid and liquid krypton', *Physical Review B* **8**(11), 4966.

Currie, S., Hoggard, N., Craven, I. J., Hadjivassiliou, M. and Wilkinson, I. D. (2013), 'Understanding mri: basic mr physics for physicians', *Postgraduate medical journal* **89**(1050), 209–223.

Dale, B. M., Brown, M. A. and Semelka, R. C. (2015), *MRI: basic principles and applications*, John Wiley & Sons.

De Graaf, R. A. (2013), *In vivo NMR spectroscopy: principles and techniques*, John Wiley & Sons.

Dodd, C. and Deeds, W. (1968), 'Analytical solutions to eddy-current probe-coil problems', *Journal of applied physics* **39**(6), 2829–2838.

Dorri, B., Vermilyea, M. and Toffolo, W. (1993), 'Passive shimming of mr magnets: algorithm, hardware, and results', *IEEE transactions on applied superconductivity* **3**(1), 254–257.

Driehuys, B., Cofer, G. P., Pollaro, J., Mackel, J. B., Hedlund, L. W. and Johnson, G. A. (2006), 'Imaging alveolar–capillary gas transfer using hyperpolarized 129xe mri', *Proceedings of the National Academy of Sciences* **103**(48), 18278–18283.

Edelman, R. R., Hatabu, H., Tadamura, E., Li, W. and Prasad, P. V. (1996), 'Noninvasive assessment of regional ventilation in the human lung using oxygen–enhanced magnetic resonance imaging', *Nature medicine* **2**(11), 1236.

Elster, A. D. and Burdette, J. H. (2001), 'Questions and answers in magnetic resonance imaging, 2e'.

Fain, S., Schiebler, M. L., McCormack, D. G. and Parraga, G. (2010), 'Imaging of lung function using hyperpolarized helium-3 magnetic resonance imaging: review of current and emerging translational methods and applications', *Journal of Magnetic Resonance Imaging* **32**(6), 1398–1408.

Finnemore, D., Stromberg, T. and Swenson, C. (1966), 'Superconducting properties of high-purity niobium', *Physical Review* **149**(1), 231.

Fleckenstein, J., Archer, B., Barker, B., Vaughan, J., Parkey, R. and Peshock, R. (1991), 'Fast short-tau inversion-recovery mr imaging.', *Radiology* **179**(2), 499–504.

Garcia, S., Lana, C., Thomas, L., Song, H., David, W. and Alexander, P. (2007), 'Sensitivity enhancement by exchange mediated magnetization transfer of the xenon biosensor signal', *Journal of Magnetic Resonance* **184**(1), 72–77.

Gierada, D. S., Saam, B., Yablonskiy, D., Cooper, J. D., Lefrak, S. S. and Conradi, M. S. (2000), 'Dynamic echo planar mr imaging of lung ventilation with hyperpolarized 3he in normal subjects and patients with severe emphysema', *NMR in Biomedicine: An International Journal Devoted to the Development and Application of Magnetic Resonance In Vivo* **13**(4), 176–181.

Glover, G. and Pauly, J. (1992), 'Projection reconstruction techniques for reduction of motion effects in mri', *Magnetic resonance in medicine* **28**(2), 275–289.

Goodson, B. (2002), 'Nuclear magnetic resonance of laser-polarized noble gases in molecules, materials, and organisms', *Journal of Magnetic Resonance* **155**(2), 157–216.

Gould, S. and Isaacson, P. (1993), 'Bronchus-associated lymphoid tissue (balt) in human fetal and infant lung', *The Journal of pathology* **169**(2), 229–234.

Grover, B. (1978), 'Noble-gas nmr detection through noble-gas-rubidium hyperfine contact interaction', *Physical Review Letters* **40**(6), 391.

Haase, A., Frahm, J., Matthaei, D., Hanicke, W. and Merboldt, K.-D. (1986), 'Flash imaging. rapid nmr imaging using low flip-angle pulses', *Journal of Magnetic Resonance (1969)* **67**(2), 258–266.

Happer, W., Miron, E., Schaefer, S., Schreiber, D., Van Wijngaarden, W. and Zeng, X. (1984), 'Polarization of the nuclear spins of noble-gas atoms by spin exchange with optically pumped alkali-metal atoms', *Physical Review A* **29**(6), 3092.

Hatabu, H., Wielopolski, P. A. and Tadamura, E. (1999), 'An attempt of pulmonary perfusion imaging utilizing ultrashort echo time turbo flash sequence with signal targeting and alternating radio-frequency (star)', *European journal of radiology* **29**(2), 160–163.

Hess, D., MacIntyre, N. and Galvin, W. (2015), *Respiratory Care: Principles and Practice*, Jones & Bartlett Learning.
URL: *https://books.google.co.uk/books?id=cnJuCQAAQBAJ*

Hidalgo-Tobon, S. (2010), 'Theory of gradient coil design methods for magnetic resonance imaging', *Concepts in Magnetic Resonance Part A* **36**(4), 223–242.

Horton-Garcia, C. F., Pavlovskaya, G. E. and Meersmann, T. (2005), 'Introducing krypton nmr spectroscopy as a probe of void space in solids', *Journal of the American Chemical Society* **127**(6), 1958–1962.

Hughes-Riley, T., Six, J. S., Lilburn, D. M., Stupic, K. F., Dorkes, A. C., Shaw, D. E., Pavlovskaya, G. E. and Meersmann, T. (2013), 'Cryogenics free production of hyperpolarized 129xe and 83kr for biomedical mri applications', *Journal of Magnetic Resonance* **237**, 23–33.

Ingman, P., Jokisaari, J. and Diehl, P. (1991), '83kr and 131xe nmr of the noble gases dissolved in nematic liquid crystals. determination of quadrupole couplings and electric field gradients', *Journal of Magnetic Resonance (1969)* **92**(1), 163–169.

Jokisaari, J., Ingman, P., Lounila, J., Pulkkinen, O., Diehl, P. and Muenster, O. (1993), 'Electric field gradients experienced by the noble gas isotopes 21ne, 83kr and 131xe in thermotropic liquid crystals', *Molecular Physics* **78**(1), 41–54.

Kanal, E., Shellock, F. G. and Talagala, L. (1990), 'Safety considerations in mr imaging.', *Radiology* **176**(3), 593–606.

Keeler, J. (2011), *Understanding NMR spectroscopy*, John Wiley & Sons.

Kino, A., Zuehlsdorff, S., Sheehan, J. J., Weale, P. J., Carroll, T. J., Jerecic, R. and Carr, J. C. (2009), 'Three-dimensional phase-sensitive inversion-recovery turbo flash sequence for the evaluation of left ventricular myocardial scar', *American Journal of Roentgenology* **193**(5), W381–W388.

Konefał, Z. (1999), 'Observation of collision induced processes in rubidium–ethane vapour', *Optics communications* **164**(1-3), 95–105.

Krjukov, O'Neill and John, O.-B. (2005), 'Brute force polarization of 129Xe', *Journal of Low Temperature Physics* **140**(5-6), 397–408.

Krupke, W. F., Beach, R. J., Kanz, V. K. and Payne, S. A. (2003), 'Resonance transition 795-nm rubidium laser', *Optics letters* **28**(23), 2336–2338.

Kuethe, D. O., Caprihan, A., Fukushima, E. and Waggoner, R. A. (1998), 'Imaging lungs using inert fluorinated gases', *Magnetic resonance in medicine* **39**(1), 85–88.

Kwok, H. S., Shaw, D. T. and Naughton, M. J. (1993), 'Superconductivity and its applications'.

Lemdiasov, R. A. and Ludwig, R. (2005), 'A stream function method for gradient coil design', *Concepts in Magnetic Resonance Part B: Magnetic Resonance Engineering: An Educational Journal* **26**(1), 67–80.

Lilburn, D., Clmentine, L., Joseph, S., Eric, D., Liang, Y.-B., Dominick, S., Maria, B., Mark, B., Galina, P. and Thomas, M. (2015), 'Hyperpolarized 83Kr magnetic resonance imaging of alveolar degradation in a rat model of emphysema.', *Journal of the Royal Society, Interface / the Royal Society* **12**(107), 20150192—-.
URL: *http://rsif.royalsocietypublishing.org/content/12/107/20150192*

Lilburn, D., Galina, P. and Thomas, M. (2013), 'Perspectives of hyperpolarized noble gas MRI beyond 3He', *Journal of Magnetic Resonance* **229**, 173–186.
URL: *http://dx.doi.org/10.1016/j.jmr.2012.11.014*

Liu, Z., Araki, T., Okajima, Y., Albert, M. and Hatabu, H. (2014), 'Pulmonary hyperpolarized noble gas mri: recent advances and perspectives in clinical application', *European journal of radiology* **83**(7), 1282–1291.

Lutterbey, Gieseke, Falkenhausen, V., Morakkabati and Schild (2005), 'Lung mri at 3.0 t: a comparison of helical ct and high-field mri in the detection of diffuse lung disease', *European radiology* **15**(2), 324–328.

Lvovsky, Y., Stautner, E. W. and Zhang, T. (2013), 'Novel technologies and configurations of superconducting magnets for mri', *Superconductor Science and Technology* **26**(9), 093001.

Mark Brown (2010), *MRI: Basic Principles and Applications, 4th Edition*.

McDougall, I. L. and Bird, J. M. (1987), 'Magnet assembly having a plurality of nested coaxial coils'. US Patent 4,701,736.

Meersmann, T. and Brunner, E. (2015), *Hyperpolarized xenon-129 magnetic resonance: concepts, production, techniques and applications*, number 4, Royal Society of Chemistry.

MEERSMANN, T. and PAVLOVSKAYA, G. E. (2015), 'Beyond spin i1/41/2; hyperpolarized 131xe and 83kr magnetic resonance', *Hyperpolarized Xenon-129 Magnetic Resonance: Concepts, Production, Techniques and Applications* (4), 426.

Meersmann, T., Pavlovskaya, G. E., Cleveland, Z. I. and Stupic, K. F. (2009), 'Nuclear electric quadrupolar properties of hyperpolarized gases to probe surfaces and interfaces'. US Patent 7,576,538.

Meiboom, S. and Gill, D. (1958), 'Modified spin-echo method for measuring nuclear relaxation times', *Review of scientific instruments* **29**(8), 688–691.

Middleton, Black, Saam, Cates, Cofer, Guenther, Happer, Hedlund, Johnson, Juvan and Swartz (1995), 'MR imaging with hyperpolarized 3He gas', *Magnetic Resonance in Medicine* **33**(2), 271–275.

Mispelter, J., Lupu, M. and Briguet, A. (2006), *NMR probeheads for biophysical and biomedical experiments: theoretical principles & practical guidelines*, Imperial College Press.

Mortuza, M. G., Anala, S., Pavlovskaya, G. E., Dieken, T. J. and Meersmann, T. (2003), 'Spin-exchange optical pumping of high-density xenon-129', *The Journal of chemical physics* **118**(4), 1581–1584.

Mugler, J. P. and A, A. T. (2013), 'Hyperpolarized 129Xe MRI of the human lung', *Journal of Magnetic Resonance Imaging* **37**(2), 313–331.

Mugler, J. P. and Altes, T. A. (2013), 'Hyperpolarized 129xe mri of the human lung', *Journal of Magnetic Resonance Imaging* **37**(2), 313–331.

Organization, W. H. et al. (2011), *Global status report on noncommunicable diseases 2010*, Geneva: World Health Organization.

Pantsyrny, V., Gubkin, I., Potanina, L., Sudyev, S., Vorobieva, A., Drobyshev, V., Kozlenkova, N., Shikov, A. and Dergunova, E. (2009), 'Advances in iter-relevant nb-ti and nb _{3} sn strands and low-loss nb-ti strands in rf'.

Pavlovskaya, G. E., Cleveland, Z. I., Stupic, K. F., Basaraba, R. J. and Meersmann, T. (2005), 'Hyperpolarized krypton-83 as a contrast agent for magnetic resonance imaging', *Proceedings of the National Academy of Sciences* **102**(51), 18275–18279.

Pisanty, E. (2017), 'How strong can an electromagnet be?', Physics Stack Exchange. URL:https://physics.stackexchange.com/q/317215 (version: 2017-03-08).
URL: *https://physics.stackexchange.com/q/317215*

Rogers, N. J., Hill-Casey, F., Stupic, K. F., Six, J. S., Lesbats, C., Rigby, S. P., Fraissard, J., Pavlovskaya, G. E. and Meersmann, T. (2016), 'Molecular hydrogen and catalytic combustion in the production of hyperpolarized 83kr and 129xe mri contrast agents', *Proceedings of the National Academy of Sciences* **113**(12), 3164–3168.

Romeo, F. and Hoult, D. (1984), 'Magnet field profiling: analysis and correcting coil design', *Magnetic Resonance in Medicine* **1**(1), 44–65.

Rutherford, M. A. and Bydder, G. M. (2002), *MRI of the Neonatal Brain*, WB Saunders London.

Saguintaah, M., Couture, A., Veyrac, C., Baud, C. and Quere, M.-P. (2002), 'Mri of the fetal gastrointestinal tract', *Pediatric radiology* **32**(6), 395–404.

Schaefer, S., Cates, G. and Happer, W. (1990), 'Determination of spin-exchange parameters between optically pumped rubidium and kr 83', *Physical Review A* **41**(11), 6063.

Sharma, R. G. (2015), *Superconductivity: basics and applications to magnets*, Vol. 214, Springer.

Shier, D., Butler, J. and Lewis, R. (2001), *Human anatomy and physiology*, McGraw-Hill Boston, MA, USA.

Shukla, Y., Wheatley, A., Kirby, M., Svenningsen, S., Farag, A., Santyr, G. E., Paterson, N. A., McCormack, D. G. and Parraga, G. (2012), 'Hyperpolarized 129xe magnetic resonance imaging: tolerability in healthy volunteers and subjects with pulmonary disease', *Academic radiology* **19**(8), 941–951.

Six, J., Theodore, H.-R., David, L., Alan, D., Karl, S., Dominick, S., Peter, M., Ian, H., Galina, P. and Thomas, M. (2014), 'Pulmonary MRI contrast using Surface Quadrupolar Relaxation (SQUARE) of hyperpolarized 83Kr', *Magnetic Resonance Imaging* **32**(1), 48–53.
URL: *http://dx.doi.org/10.1016/j.mri.2013.08.007*

Six, J., Theodore, H.-R., Karl, S., Galina, P. and Thomas, M. (2012), 'Pathway to Cryogen Free Production of Hyperpolarized Krypton-83 and Xenon-129', *PLoS ONE* **7**(11).

Stehling, M. K., Turner, R. and Mansfield, P. (1991), 'Echo-planar imaging: magnetic resonance imaging in a fraction of a second', *Science* **254**(5028), 43–50.

Stupic, K. F., Cleveland, Z. I., Pavlovskaya, G. E. and Meersmann, T. (2006), 'Quadrupolar relaxation of hyperpolarized krypton-83 as a probe for surfaces', *Solid state nuclear magnetic resonance* **29**(1-3), 79–84.

Thuries, E., Pham, V., Laumond, Y., Verhaege, T., Fevrier, A., Collet, M. and Bekhaled, M. (1991), 'Towards the superconducting fault current limiter', *IEEE Transactions on Power Delivery* **6**(2), 801–808.

Vonsovsky, S. V., Izyumov, Y. A. and Kurmaev, E. Z. (1982), 'Superconductivity of transition metals'.

Wagshul, M. and Chupp, T. (1994), 'Laser optical pumping of high-density rb in polarized he 3 targets', *Physical Review A* **49**(5), 3854.

Walker, T. G. and Happer, W. (1997), 'Spin-exchange optical pumping of noble-gas nuclei', *Reviews of Modern Physics* **69**(2), 629.

Weibel, E. (2009), 'What makes a good lung', *Swiss Med Wkly* **139**(27-28), 375–386.

Weishaupt, D., Köchli, V. D. and Marincek, B. (2008), *How does MRI work?: an introduction to the physics and function of magnetic resonance imaging*, Springer Science & Business Media.

Westbrook, C. and Talbot, J. (2018), *MRI in Practice*, John Wiley & Sons.

Wielpütz, M. and Kauczor, H.-U. (2012), 'Mri of the lung: state of the art', *Diagnostic and interventional radiology* **18**(4), 344.

Witte, C., Kunth, M., öpfert, ö., Rossella, F. and Schröder, L. (2012), 'Hyperpolarized xenon for nmr and mri applications', *Journal of visualized experiments: JoVE* (67).

Won, M., Yoon, H. and Treagust, D. (2014), 'Students' learning strategies with multiple representations: Explanations of the human breathing mechanism', *Science Education* **98**(5), 840–866.

Zhao, L., Mulkern, R., Tseng, C.-H., Williamson, D., Patz, S., Kraft, R., Walsworth, R. L., Jolesz, F. A. and Albert, M. S. (1996), 'Gradient-echo imaging considerations for hyperpolarized129xe mr'.

Zibrov, A., Lukin, M., Nikonov, D., Hollberg, L., Scully, M., Velichansky, V. and Robinson, H. (1995), 'Experimental demonstration of laser oscillation without population inversion via quantum interference in rb', *Physical review letters* **75**(8), 1499.